

Fall 2014

Thermoelectric waste heat recovery in automobile exhaust systems: Topological studies and performance analysis

Sumeet Kumar
Purdue University

Follow this and additional works at: https://docs.lib.purdue.edu/open_access_dissertations



Part of the [Energy Systems Commons](#)

Recommended Citation

Kumar, Sumeet, "Thermoelectric waste heat recovery in automobile exhaust systems: Topological studies and performance analysis" (2014). *Open Access Dissertations*. 311.
https://docs.lib.purdue.edu/open_access_dissertations/311

This document has been made available through Purdue e-Pubs, a service of the Purdue University Libraries. Please contact epubs@purdue.edu for additional information.

PURDUE UNIVERSITY
GRADUATE SCHOOL
Thesis/Dissertation Acceptance

This is to certify that the thesis/dissertation prepared

By Sumeet Kumar

Entitled

THERMOELECTRIC WASTE HEAT RECOVERY IN AUTOMOBILE EXHAUST SYSTEMS:
TOPOLOGICAL STUDIES AND PERFORMANCE ANALYSIS

For the degree of Doctor of Philosophy



Is approved by the final examining committee:

Stephen D. Heister

Xianfan Xu

Timothy S. Fisher

Yue Wu

To the best of my knowledge and as understood by the student in the Thesis/Dissertation Agreement, Publication Delay, and Certification/Disclaimer (Graduate School Form 32), this thesis/dissertation adheres to the provisions of Purdue University's "Policy on Integrity in Research" and the use of copyrighted material.

Stephen D. Heister

Approved by Major Professor(s): _____

Approved by: Ganesh Subbarayan

10/02/2014

Head of the Department Graduate Program

Date

THERMOELECTRIC WASTE HEAT RECOVERY IN
AUTOMOBILE EXHAUST SYSTEMS:
TOPOLOGICAL STUDIES AND PERFORMANCE ANALYSIS

A Dissertation

Submitted to the Faculty

of

Purdue University

by

Sumeet Kumar

In Partial Fulfillment of the

Requirements for the Degree

of

Doctor of Philosophy

December 2014

Purdue University

West Lafayette, Indiana

To maa and papa...

ACKNOWLEDGEMENTS

Foremost, I would like to express my sincere gratitude to my advisors Prof. Stephen Heister and Prof. Xianfan Xu for their invaluable and brilliant guidance throughout the course of this project at Purdue. Without their support, and encouragement this work would not have been possible.

I thank Prof. Timothy Fisher and Prof. Yue Wu for serving on my thesis examining committee and for their valuable comments and suggestions. In addition, I would like to thank Dr. James Salvador and Dr. Gregory Meisner from General Motors R&D for helpful discussions and assistance with acquiring the vehicle engine and exhaust data used in this study.

I gratefully acknowledge National Science Foundation (NSF) and US Department of Energy (DOE) for financially supporting (CBET – 1048616) my graduate research at Purdue.

I am grateful to all my friends especially Sugi, Gurneesh, Astitva, Kamesh and Varun for their help and companionship throughout my stay at Purdue. I thank the graduate office staffs at ME and AAE Department for their valuable administrative support. I also want to specially thank Charlotte Bell from Zucrow laboratories for helping in travel managements for conferences and research meetings.

Sumeet Kumar

TABLE OF CONTENTS

	Page
LIST OF TABLES	vii
LIST OF FIGURES	viii
NOMENCLATURE	xvi
ABSTRACT	xx
CHAPTER 1. INTRODUCTION	1
1.1 Background	1
1.2 Thermoelectric Generator	2
1.2.1 Hot Side Heat Exchanger	3
1.2.2 Thermoelectric Components	3
1.2.2.1 Thermoelectric Couple	4
1.2.2.2 Thermoelectric Module	4
1.2.3 Coolant Supply System	6
1.2.4 Bypass System	6
1.3 Major Challenges	6
1.4 Literature Survey	9
1.4.1 Thermoelectric Generator Design	10
1.4.2 Thermoelectric Material	14
1.5 Motivation	16
1.6 Objectives of Present Study	17
1.7 Thesis Organization	18
CHAPTER 2. THERMOELECTRIC GENERATOR MODEL	19
2.1 Modeling of Thermoelectric Generator System	19
2.1.1 Assumptions	19
2.1.2 Volume Discretization	20
2.1.3 Thermal Resistance Network	21
2.1.4 Pressure Drop Calculations	27

	Page
2.1.5	Solution Methodology.....28
2.2	Design Model for Thermoelectric Generator 30
2.2.1	Rectangular Topology31
2.2.1.1	Longitudinal Flow Configuration 31
2.2.1.2	Transverse Flow Configuration 33
2.2.2	Circular Topology35
2.2.2.1	Hexagonal Configuration 35
2.2.2.2	Cylindrical Configuration..... 35
2.3	Verification and Validation..... 38
2.3.1	Grid Independence38
2.3.2	Energy Balance41
CHAPTER 3.	TOPOLOGY STUDIES AND PERFORMANCE ANALYSIS 42
3.1	Inlet Conditions 43
3.2	User Inputs for Parametric Studies..... 43
3.3	Baseline Geometry 45
3.3.1	Effect of Mass flow Rate and Inlet Temperature45
3.3.2	Major Conclusions53
3.4	Rectangular Topology 54
3.4.1	Longitudinal Flow Configuration54
3.4.2	Major Conclusions61
3.4.3	Transverse Configuration.....62
3.4.4	Major Conclusions68
3.5	Circular Topology 69
3.5.1	Hexagonal Topology.....69
3.5.2	Major Conclusions74
3.5.4	Cylindrical Topology75
3.5.5	Major Conclusions80
3.5.7	Model Comparison.....81
CHAPTER 4.	OPTIMIZATION OF SKUTTERUDITE BASED 82
	THERMOELECTRIC MODULES 82

	Page
4.1 Introduction	82
4.2 Literature Survey	82
4.3 Numerical Modeling	84
4.4 Thermoelectric Module Optimization	90
4.5 Thermoelectric Design for TEG Optimization	94
4.5.1 Case 1: Uniform Heat Transfer and Temperature	96
4.5.2 Case 2: Varying Heat Transfer and Temperature	97
4.6 Conclusions	100
CHAPTER 5. EFFECT OF HOT WALL AXIAL CONDUCTION ON THE	
PERFORMANCE OF THERMOELECTRIC GENERATORS	101
5.1 Axial Conduction in Hot Wall Liner	101
5.2 Numerical Model	102
5.3 Solution Method	106
5.4 Results	107
5.4.1 Liner Material and Thickness Sensitivity	107
5.4.2 Inlet Condition Sensitivity	114
5.5 Conclusions	118
CHAPTER 6. SUMMARY	120
6.1 Summary and Conclusions	120
6.2 Future Work	121
6.2.1 Jet Impingement	121
6.2.2 Modeling Test Bed to Support TEG Development	122
6.2.3 Transient Analysis	122
6.2.4 Computational Analysis of 3D Model	122
LIST OF REFERENCES	124
APPENDIX	129
VITA	131
PUBLICATIONS	132

LIST OF TABLES

Table	Page
Table 1.1. Previous efforts in Automotive TEG prototype development.	13
Table 2.1. Inputs required in thermal resistance network.	26
Table 2.2. Energy Balances for four Models.	41
Table 3.1. User Inputs.	44
Table 3.2. General Motors' baseline model configuration.	45
Table 3.3. Thermoelectric Couple Parameters.	52
Table 4.1. Optimal current density values for Skutterudites for leg height	
Lx = 10 mm.	90
Table 4.2. Electrical power generation for both cases.	100
Table 5.1. Parameters representing impact of axial conduction on TEG performance. .	113
Table 5.2. Parameters representing impact of axial conduction effects on TEG.	
performance at inlet mass flow rate of 5 g/s.	118

LIST OF FIGURES

Figure	Page
Figure 1.1. Energy flow path in an internal combustion engine [1].	1
Figure 1.2. Illustration of the location of a thermoelectric generator in a vehicle.	
For the TEG drawing: gray body: hot gas heat exchanger; thin green layer above	
and below hot gas heat exchanger: TE modules; yellow blocks with tubing: cold side	
heat exchanger. (Courtesy: General Motors)	2
Figure 1.3. Schematic of a thermoelectric couple	5
Figure 1.4. Stratified Schematic of a thermoelectric module.	5
Figure 1.5. Maximum efficiency for a thermoelectric device at various T_H with	
$T_C = 100^\circ\text{C}$ using Eq. (1.1) [3].	7
Figure 1.6. ZT curve for thermoelectric materials [8–10,44,45].	14
Figure 1.7. Figure of Merit ZT values for Thermo-electric materials [8,44,45]	16
Figure 2.1. Thermal resistance network and temperature locations	22
Figure 2.2. Flowchart for the solution methodology.	29
Figure 2.3. Longitudinal Flow Configuration	32
Figure 2.4. Transverse Flow Configuration.	34
Figure 2.5. Hexagonal Configuration.	36
Figure 2.6. Cylindrical Configuration.	37
Figure 2.7. Grid Independence study for Longitudinal Flow Model.	39

Figure	Page
Figure 2.8. Grid Independence study for Transverse Flow Model.	39
Figure 2.9. Grid Independence study for Hexagonal Model.	40
Figure 2.10. Grid Independence study for Cylindrical Model.	40
Figure 3.1. Power output vs. flow rate for Baseline Model at $T_{in} = 823 \text{ K}$ (550°C).....	47
Figure 3.2. Total pressure drop vs. flow rate for Baseline Model at $T_{in} = 823\text{K}$ (550°C).....	47
Figure 3.3. Power output vs. Inlet Temperature for Baseline Model at $\dot{m}_{in} = 35 \text{ g/s}$	48
Figure 3.4. Total pressure drop vs. Inlet Temperature for Baseline Model at \dot{m}_{in} $= 35 \text{ g/s}$. The allowed pressure drop is 812 Pa at given flow rate of 35 g/s	48
Figure 3.5. Temperature differences across materials along flow direction for Baseline Model at $\dot{m}_{in} = 35\text{g/s}$ and $T_{in} = 550^\circ\text{C}$	50
Figure 3.6. Energy flux along flow length for Baseline Model at \dot{m}_{in} $= 35\text{g/s}$ and $T_{in} = 550^\circ\text{C}$	50
Figure 3.7. Thermal energy distribution for Baseline Model.	52
Figure 3.8. Normalized parameters along the TEG length at $\dot{m}_{in} = 35\text{g/s}$ and $T_{in} = 550^\circ\text{C}$	52
Figure 3.9. Power output vs. different fin configurations at $\dot{m}_{in} = 35\text{g/s}$ and $T_{in} = 550^\circ\text{C}$	55
Figure 3.10. Total Pressure drop vs. different fin configurations at \dot{m}_{in} $= 35\text{g/s}$ and $T_{in} = 550^\circ\text{C}$	55
Figure 3.11. ZT values for a thermoelectric couple based on Skutterudite and Bismuth Telluride Modules. Cutoff temperature for transition is set at 550K	56

Figure	Page
Figure 3.12. Power output vs. different mass flow rates at $T_{in}=550^{\circ}\text{C}$ for ‘S’ and ‘SB’ arrangement with optimized heat exchanger configuration. . S-SB and B-SB denote the number of separate Skutterudites and Bismuth Telluride modules required for ‘SB’ configuration.	57
Figure 3.13. Number of TEMs vs. flow rates at $T_{in}=550^{\circ}\text{C}$ for ‘S’ and ‘SB’ arrangement with optimized heat exchanger configuration.	57
Figure 3.14. Power output vs. Inlet exhaust temperatures at $\dot{m}_{in}=35\text{ g/s}$ for ‘S’ and ‘SB’ arrangement with optimized heat exchanger configuration.	58
Figure 3.15. Number of TEMs vs. Inlet exhaust temperatures at $\dot{m}_{in}=35\text{ g/s}$ for ‘S’ and ‘SB’ arrangement with optimized heat exchanger configuration.	58
Figure 3.16. 3D plot of Power output at optimized fin configurations at $\dot{m}_{in}=35\text{ g/s}$ and $T_{in}=550^{\circ}\text{C}$	60
Figure 3.17. Power output and pressure drop variation at different aspect ratio (AR = width/length) at fixed generator height of 38 mm using 50 skutterudites (Inlet: $\dot{m}_{in}=35\text{ g/s}$, $T_{in}=550^{\circ}\text{C}$ for with $t_{fin}=3.3\text{ mm}$ and $s_{fin}=6.35\text{ mm}$).	60
Figure 3.18. Left Y axis represents electrical power output with varying channel width (1 mm - 50 mm) with $N_{fin}=9$ per channel ($t_{fin}=2\text{ mm}$, $s_{fin}=2.2\text{ mm}$) with baseline geometry(height: 3.8 cm, width: 22.4 cm and length: 41.3 cm) at \dot{m}_{in} $=35\text{ g/s}$ and $T_{in}=550^{\circ}\text{C}$. Right Y axis displays number of skutterudite modules.	63
Figure 3.19. Y axis represents total pressure drop with varying channel width for same inputs mentioned in Figure 3.18.	63

Figure	Page
Figure 3.20. The top figure shows the optimized power output with respect to..... varying AR (aspect ratio = width/height) keeping the length equal to 1 module side at $T_{in} = 550^{\circ}\text{C}$. The legend shows electrical output at different mass flow rates..... The bottom figure represents number of skutterudite modules required for each configuration.	65
Figure 3.21. The top figure shows the optimized power output with respect to..... varying AR (Aspect ratio = width/height) keeping the length equal to 1 module..... side for $\dot{m}_{in} = 35 \text{ g/s}$ and $T_{in} = 550^{\circ}\text{C}$. The colored curves show electrical output at different number of skutterudites modules as shown in legend..... The bottom figure shows the pressure drop occurred for the same case.	67
Figure 3.22. Power output with varying outer diameter for different inner diameters for 'S' configuration at $\dot{m}_{in} = 35 \text{ g/s}$ and $T_{in} = 550^{\circ}\text{C}$ for optimized heat..... exchanger configuration. Right Y-axis shows number of Modules.	70
Figure 3.23. Total Pressure drop with varying outer diameter for different inner..... diameters for 'S' configuration at $\dot{m}_{in} = 35 \text{ g/s}$ and $T_{in} = 550^{\circ}\text{C}$ for optimized..... heat exchanger configuration.	70
Figure 3.24. Power output with varying mass flow rates for outer diameter..... = 0.105m and inner diameter = 0.04 m for 'S' and 'SB' configuration at $T_{in} = 550^{\circ}\text{C}$	72
Figure 3.25. Number of Modules vs. mass flow rates for outer diameter = 0.105 m and inner diameter = 0.04 m for 'S' and 'SB' configuration at $T_{in} = 550^{\circ}\text{C}$	72
Figure 3.26. Power output with varying inlet temperatures for outer diameter = 0.105 m and inner diameter = 0.04 m for 'S' and 'SB' configuration at $\dot{m}_{in} = 35 \text{ g/s}$	73

Figure	Page
Figure 3.27. Number of Modules vs. varying inlet temperatures for outer diameter = 0.065 m and inner diameter = 0.04 m for 'S' and 'SB' configuration at $\dot{m}_{in} = 35$ g/s.	73
Figure 3.28. Power output with varying outer diameter shown for different inner diameters for 'S' configuration ($\dot{m}_{in} = 35$ g/s and $T_{in} = 550^{\circ}\text{C}$). Right axis shows the required number of Skutterudite Modules.	76
Figure 3.29. Total Pressure drop with varying outer diameter for different inner diameters for 'S' configuration ($\dot{m}_{in} = 35$ g/s and $T_{in} = 550^{\circ}\text{C}$).	76
Figure 3.30. Power output with varying mass flow rates for outer diameter = 0.08 m and inner diameter = 0.04 m for 'S' and 'SB' configuration at $T_{in} = 550^{\circ}\text{C}$ for optimized heat exchanger configuration.	78
Figure 3.31. Required number of Modules with varying mass flow rates for outer diameter = 0.08 m and inner diameter = 0.04 m for 'S' and 'SB' configuration at $T_{in} = 550^{\circ}\text{C}$ for optimized heat exchanger configuration.	78
Figure 3.32. Power output with varying inlet temperatures for outer diameter = 0.08 m and inner diameter = 0.04 m for 'S' and 'SB' configuration at $\dot{m}_{in} = 35$ g/s. ...	79
Figure 3.33. Required number of modules with varying inlet temperatures for outer diameter = 0.08 m and inner diameter = 0.04 m for 'S' and 'SB' configuration at $\dot{m}_{in} = 35$ g/s.	79
Figure 3.34. Power dependence of various designs on number of TEMs.	81
Figure 4.1. Schematic of a thermoelectric couple with discretization along leg height ...	84
Figure 4.2. ZT curves for the Skutterudites [8,9].	87

Figure	Page
Figure 4.3. Mesh independence study at respective current density fluxes.....	
at $J_P = 50.9 \text{ A/cm}^2$, $J_N = -37.1 \text{ A/cm}^2$, $\Delta T = 450^\circ \text{C}$ and $L_x = 10 \text{ mm}$	88
Figure 4.4. Heat flux and temperature profiles along the TE legs at $J_P = 50.9 \text{ A/cm}^2$,	
$J_N = -37.1 \text{ A/cm}^2$, $\Delta T = 450^\circ \text{C}$ and $L = 10 \text{ mm}$	89
Figure 4.5. Respective leg efficiencies vs. input current density fluxes with.....	
$\Delta T = 450^\circ \text{C}$ and $L = 10 \text{ mm}$	89
Figure 4.6. TE Module vs. Current Density Values at $\Delta T = 450^\circ \text{C}$ and $L_x = 10 \text{ mm}$	91
Figure 4.7. TE efficiency vs. J_P for various leg heights at $\Delta T = 450^\circ \text{C}$ and.....	
$A_N/A_P = 0.8$	92
Figure 4.8. TE efficiency vs. hot side heat flux for various leg heights at ΔT	
$= 450^\circ \text{C}$ and $A_N/A_P = 0.8$	92
Figure 4.9. TE efficiency vs. J_P for various ΔT at $L_x = 10 \text{ mm}$ and $A_N/A_P = 0.8$	93
Figure 4.10. TE efficiency vs. hot side heat flux for various ΔT at $L_x = 10 \text{ mm}$	
and $A_N/A_P = 0.8$	94
Figure 4.11. Variation of heat transfer and temperature over a heat exchanger	
surface for Case 1 and Case 2. The linear variation is approximated as stepwise.....	
profile in five steps for Case 2.	96
Figure 4.12. Electrical power estimates versus leg height at different fill fraction	
for Case 1 with area ratio (A_N/A_P) fixed at 0.8 for skutterudite.	98
Figure 4.13. Required volume of TE materials for Case 1 at different fill fractions.	98

Figure	Page
Figure 4.14. Electrical power generation at various leg heights for optimal fill fraction and $A_N/A_P = 0.8$. The steps 1-5 represent each row of TE couples arranged along the flow direction.	99
Figure 4.15. Optimal fill fractions at various leg heights for Steps 1-5 varying along the flow direction (Case 2). The right axis shows the required volume of Skutterudite material.....	99
Figure 5.1. Schematic of a longitudinal thermoelectric generator with control volumes for hot gas passage and the hot gas wall lining	102
Figure 5.2. Thermal energy transport in i^{th} hot wall liner and gas CV	103
Figure 5.3. Thermal resistance network in a control volume	104
Figure 5.4. Gas temperature variation along the flow direction for (a) Copper and (b) Stainless steel Wall liners at $\dot{m} = 36\text{g/s}$ and $T_{\text{in}} = 973\text{K}$	109
Figure 5.5. Hot wall liner temperature variation along the flow direction for..... (a) Copper and (b) Stainless steel Wall liners at $\dot{m} = 36\text{g/s}$ and $T_{\text{in}} = 973\text{K}$	110
Figure 5.6. TEM junction temperature variation along the flow direction for (a) Copper and (b) Stainless steel Wall liners at $\dot{m} = 36\text{g/s}$ and $T_{\text{in}} = 973\text{K}$	111
Figure 5.7. Axial conduction flux in wall lining and its variation along the flow direction for Copper and Stainless steel Wall liners at $\dot{m} = 36\text{g/s}$ and $T_{\text{in}} = 973\text{K}$	112
Figure 5.8. Gas temperature variation along the flow direction for 5 mm and 20..... mm thick stainless steel liners at inlet temperatures of 473K, 773K and 1073K with flow rates 5g/s, 25g/s and 50g/s.....	115

Figure	Page
Figure 5.9. Liner temperature variation along the flow direction for 5 mm and 20 mm thick stainless steel liners at inlet temperatures of 473K, 773K and 1073K with flow rates 5g/s, 25g/s and 50g/s.	116
Figure 5.10. TEM junction temperature variation along the flow direction for 5 mm and 20 mm thick stainless steel liners at inlet temperatures of 473K, 773K and 1073K with flow rates 5g/s, 25g/s and 50g/s.	117
Appendix Figure	
Figure A 1. Method comparison at different current inputs for skutterudites at $Lx = 10 \text{ mm}$, $A_N/A_P = 0.8$; $\Delta T = 450^\circ\text{C}$, and $A_p = 1\text{cm}^2$	130

NOMENCLATURE

Uppercase Roman

A	surface area, m^2
AR	aspect ratio, -
C_p	specific heat capacity of air, $\text{kJ}/(\text{kg}\cdot\text{K})$
CV	control volume
Cu	copper metal
Err	error
H	enthalpy flow, J
I	electric current, A
J	electric current density flux, A/m^2
K	thermal conductance, $\text{W}/(\text{m}\cdot\text{K})$
L	length, m
N	number
N_x	number of discrete segments along +X axis direction, -
P	pressure drop, Pa
P_{el}	electrical power, W
Q	heat transfer rate, W
R	thermal resistance, K/W

R_{el}	electrical resistance, Ω
S (italicized)	seebeck coefficient, V/K
S	skutterudite thermoelectric module
SB	hybrid module configuration of skutterudite and bismuth telluride materials
T	temperature, K
TEC	thermoelectric couple,-
V	electrical voltage, V
ZT	dimensionless thermoelectric figure of merit,-

Lowercase Roman

d	density of air, kg/m^3
f	surface friction factor
h	surface heat transfer coefficient, $\text{W}/(\text{m}^2\text{-K})$
\dot{m}	mass flow rate of air, kg/s
n	number of thermocouples in a control volume
q	heat flux, W/m^2
s	spacing, m
t	thickness, m
v	air velocity, m/s
x	distance from thermoelectric generator inlet, m

Greek Symbols

Δ	change in quantity
----------	--------------------

ϵ	emissivity of radiating surface
κ	thermal conductivity, W/ (m-K)
μ	coefficient of contraction
η	efficiency
ρ	electrical resistivity, Ω -m
σ	Stefan-Boltzmann constant, W/(m ² -K ⁴)

Subscripts

C	cold side
ch	fin channel
Con	contraction
el	electric
eq	equivalent
Exp	expansion
g	gas
H	hot side
HeX	heat exchanger
i	ith control volume
in	thermoelectric generator inlet
Ins	insulation
L	load
max	maximum
n	n type thermoelectric material

oc	open circuit
out	thermoelectric generator outlet
p	p type thermoelectric material
rad	radiation
rel	relative
t	total
trf	transfer
w	thermoelectric generator liner/ wall

ABSTRACT

Kumar, Sumeet. Ph.D., Purdue University, December, 2014. Thermoelectric Waste Heat Recovery in Automobile Exhaust Systems: Topological Studies and Performance Analysis. Major Professors: Dr. Stephen Heister and Dr. Xianfan Xu, School of Mechanical Engineering.

The demand for improved fuel efficiency in automobiles has placed an emphasis on exhaust system waste heat recovery as a 40% of the fuel's chemical energy is lost to the environment in modern spark ignition engines. To advance fuel economy, researchers are currently evaluating technologies to exploit exhaust stream thermal power using thermoelectric generators (TEGs) that operate using the Seebeck effect. Thermoelectric generators have the potential to recover some of this waste energy in the exhaust stream potentially improving fuel economy by as much as 5%.

Attempts are made to maximize the electrical power generation by optimizing the thermoelectric generator geometry for a prescribed volume. A plate-fin heat exchanger configuration is assumed and consideration is given to pressure drops associated with the fins placed in the exhaust flow path; and the cross-sectional changes across thermoelectric generator inlet-exit ports. Multiple filled skutterudites based thermoelectric modules are employed in the higher temperature regions and Bismuth Telluride modules are used at lower temperature regions of the device.

Power is optimized for rectangular configurations featuring longitudinal and transverse flow through the device and for hexagonal and cylindrical topologies as well. Optimal designs that maximize power output for fixed volume and number of thermoelectric elements are obtained for all configurations. In general, the rectangular configuration with transverse flow has the best overall performance.

System modeling of thermoelectric (TE) components is performed to maximize thermoelectric power generation. One-dimensional heat flux and temperature variations across thermoelectric legs have been solved using iterative numerical approach as a tool to optimize both TE module and TEG designs. Design trades are explored assuming the use of skutterudite as thermoelectric material that has potential for application to automotive applications where exhaust gas and heat exchanger temperatures typically vary from 100°C to 600°C. Dependencies of parameters such as leg geometry, fill fractions, electric current, thermal boundary conditions, etc., on leg efficiency, thermal fluxes and electric power generation have been studied in detail. Optimal leg geometries are computed for various automotive exhaust conditions.

Axial conduction in the wall liner is further modeled numerically and its impact on temperature distribution in gas stream, wall liner, and temperature difference across thermoelectric junctions are presented. The developed model is simulated to establish TEG output sensitivity to liner materials and thicknesses for both zero and non-zero axial conduction cases. Further, the axial conduction sensitivity to inlet conditions is considered and the effect on TEG output statistics are presented.

CHAPTER 1. INTRODUCTION

1.1 Background

Substantial waste heat energy is available from automobile exhaust gas. Two-thirds of the thermal energy in a vehicle is lost as waste heat, out of which 40% is lost through hot exhaust gas [1,2] as shown in Figure 1.1. Thermoelectric generators (TEGs) have the potential to recover some of this waste energy in the exhaust stream potentially improving fuel economy by as much as 5%.

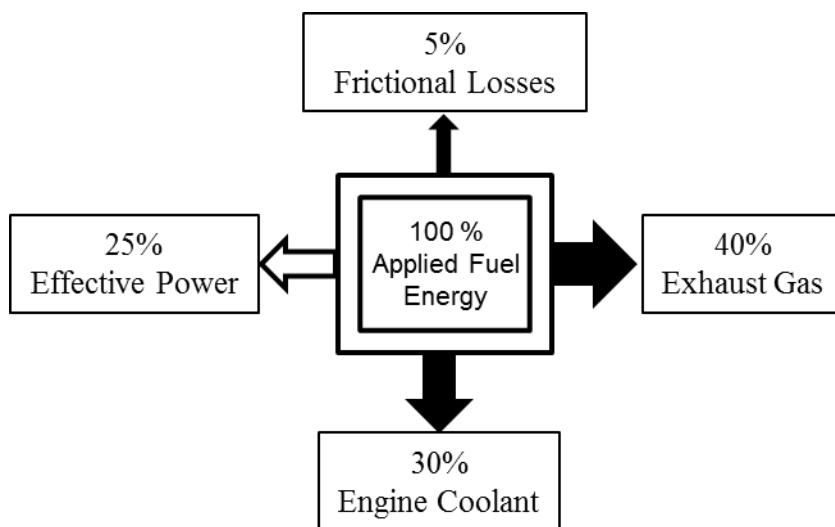


Figure 1.1. Energy flow path in an internal combustion engine [1].

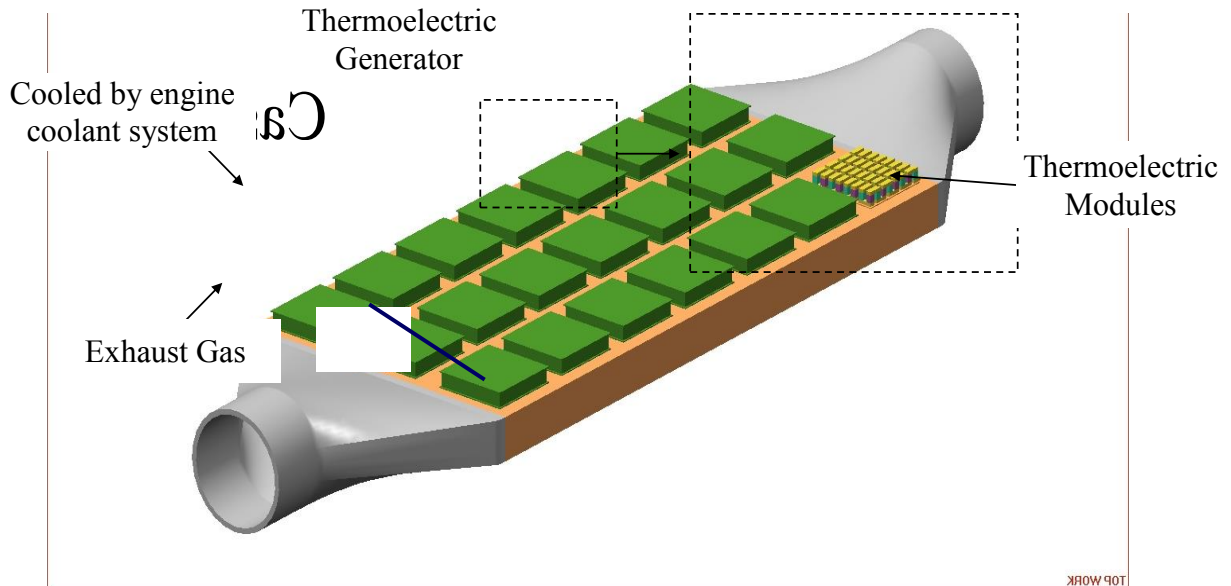


Figure 1.2. Illustration of the location of a thermoelectric generator in a vehicle. For the TEG drawing: gray body: hot gas heat exchanger; thin green layer above and below hot gas heat exchanger: TE modules; yellow blocks with tubing: cold side heat exchanger. (Courtesy: General Motors)

1.2 Thermoelectric Generator

Thermoelectric generator is a device which converts available waste heat from an automobile exhaust into electricity using the Seebeck Effect as shown in Figure 1.2. The main components of these devices are: - a hot side heat exchanger, a coolant and cold side heat exchanger system, thermoelectric materials packaged as modules and a bypass system. The bypass system is required for scenarios when the exhaust gas exceeds the maximum allowable temperature for the safer operation of the thermoelectric modules. The hot side heat exchangers are either exhaust gas based or coolant based. The exhaust gas based TEGs convert the available waste heat from the exhaust gas of the internal combustion engine into usable electricity. Similarly, coolant based TEGs use the engine's coolant waste heat to generate electricity.

1.2.1 Hot Side Heat Exchanger

The hot exhaust gas from the automobile engine flows through the thermoelectric generator. The working fluid is a mixture of unburnt fuel, oxides of carbon, sulfur and remaining nitrogen. Here, the fluid can be modeled as a hot air without much loss in generality. The heat transfer through air poses a big constraint due to limitation of poor heat transfer coefficient. Desirable heat transfer is achieved by effective design of heat exchanger system. There could be several choices of commercial heat exchangers. However, plate fin based heat exchanger was preferred for the current design analysis due to its simplicity in design and modeling. In a plate fin heat exchanger, adding large number of fins could be helpful in augmenting high heat transfer rates but at the same time dangerously poses a risk of high back pressure rise which affects the fuel economy and engine performance. Hence optimum number of fins and fin thickness or spacing is the effective way of increasing the system effectiveness.

1.2.2 Thermoelectric Components

The thermoelectric n and p type materials are arranged in form of thermoelectric couples which are commercially packaged as thermoelectric modules. These thermoelectric modules are characterized by their hot and cold junction surfaces. The hot side is in contact with of the hot surface of the thermoelectric generator and the cold side in contact with engine coolant supply.

1.2.2.1 Thermoelectric Couple

Figure 1.3 depicts a schematic of a typical thermoelectric couple. The n-type and p-type thermoelectric legs are sandwiched between copper conductive tabs. These copper tabs complete the electric circuit when connected to an external electrical load resistance. These tabs are attached to ceramic substrates such as Alumina (Aluminum Nitride). Ceramic substrates are good heat conductor and excellent electrical insulators. Hence they facilitate heat transfer across the intermediate junctions and prevent any electrical current leakage. The hot side of the thermoelectric couple is kept in contact with the thermoelectric generator and heat exchanger assembly using commercial thermal grease to reduce thermal interface resistance. The cold side is in thermal contact with the engine coolant supply which is maintained at constant temperature of 100°C. A plate fin type heat exchanger is integrated into the TEG to enhance heat transfer from the hot exhaust gas to hot side of Thermoelectric (TE) couples. The plate fin assembly contact resistance depends on integration and is not considered in current model.

1.2.2.2 Thermoelectric Module

An array of thermoelectric couples is arranged on a ceramic substrate to constitute a Thermoelectric Module. The n-type and p-type legs are connected serially to form an electrical circuit and parallel fashion in a thermal circuit. Individual modules can be connected in a desired pattern to output required voltage and wattage. A stratified illustration is provided in Figure 1.4.

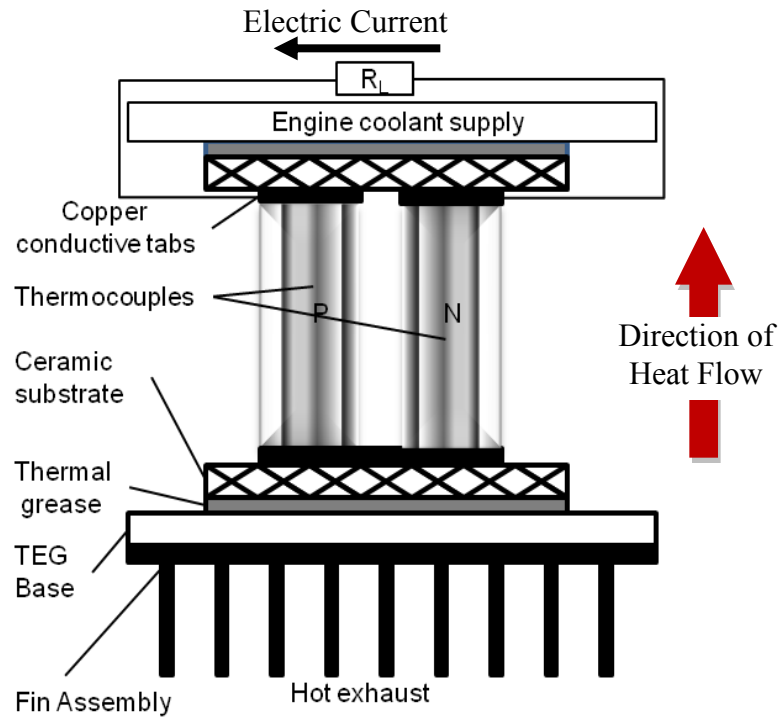


Figure 1.3. Schematic of a thermoelectric couple.

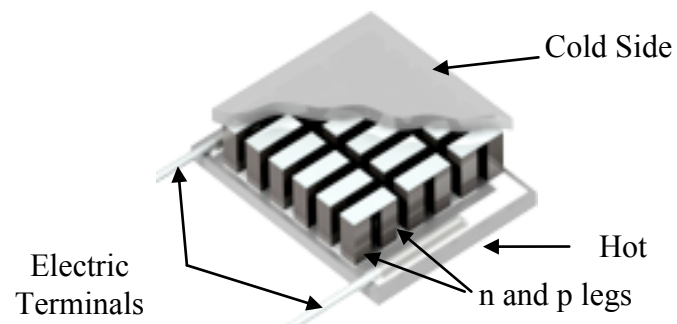


Figure 1.4. Stratified Schematic of a thermoelectric module.

Source: http://www.tec-microsystems.com/EN/Intro_Thermoelectric_Coolers.html.

1.2.3 Coolant Supply System

The cold side of the thermoelectric modules is in contact with the engine coolant supply. Engine coolant used in automobiles such as ethylene glycol generally has high specific heat capacity; hence the variation in coolant temperatures during heat transfer is within the range of 5°C. The rectangular blocks with coolant supply are attached to the cold side of modules to maintain temperatures around 100°C. However, this increases the load on car radiator and may lead to increase in radiator size.

1.2.4 Bypass System

The exhaust gas temperature depends on engine running condition and can shoot upto very high temperatures during extreme load conditions. Thus, exhaust temperatures may exceed safer limits of thermoelectric components resulting in impairment of devices. Design of a bypass flow system to prevent such scenarios is a critical part of this analysis. The bypass system can be located within or outside to the thermoelectric generator. A control valve may be utilized in addition to facilitate the hot gas transfer under bypass conditions.

1.3 Major Challenges

The major challenges associated with modeling of thermoelectric generators for automobiles are:

- 1) Thermoelectric Materials – The low figure of merit (ZT) values for the currently viable thermoelectric materials account for low overall system energy conversion efficiencies. Significant research activities are going on to improve the ratio of

electrical to thermal conductivity in multiple doped semi-conductors. The maximum possible efficiency of a thermoelectric device for hot side T_H and cold side T_C temperatures is given by Eq. (1.1) at various ZT s [3]. To achieve a device efficiency of 25% for automobile application, the thermoelectric materials must have a bulk material ZT of 4 and above.

$$\eta_{\max} = \frac{T_H - T_C}{T_H} \frac{\sqrt{1 + ZT} - 1}{\sqrt{1 + ZT} + \frac{T_C}{T_H}} \quad (1.1)$$

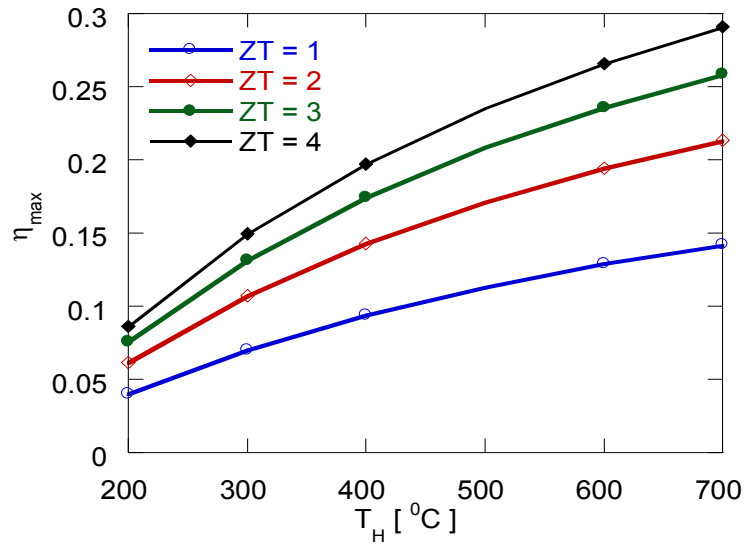


Figure 1.5. Maximum efficiency for a thermoelectric device at various T_H with $T_C = 100^\circ\text{C}$ using Eq. (1.1) [3].

- 2) Engine back pressure – The installation of thermoelectric generators amounts to additional pressure drops along the exhaust pipeline. The viscous drag on the heat exchanger fins and generator walls amount to considerable pressure drops. The variations in cross-sections along manifolds too add up, amounting to net pressure

drop. The increased back pressure leads to adverse effects on the automobile engine; hence reducing engine efficiency and decreasing fuel economy.

- 3) Topology – The shape of the thermoelectric generator governs the heat transfer and fluid flow characteristics in the flow region. The available volume for a TEG design is limited and restricted for a vehicle type. Inefficient topology design may end up losing waste heat energy, increased device cost, etc. The device must fit properly the geometrical constraints for an automobile.
- 4) Heat exchanger – The design of the heat exchanger is very critical for efficient thermo-electric energy conversion. The gas flows in the TEG have Reynolds numbers (based on hydraulic diameter) in the range of 1000-5000 thereby placing it in a transition region between laminar and turbulent. Because there is a very limited pressure drop available in the exhaust gases, it is difficult to attain good heat transfer coefficients under these conditions. Deployment of large number of fins would result in marginal gain in heat transfer with increased pressure drop, weight and cost; whereas heat exchanger with inadequate fin design (number and thickness) would result in insufficient heat transfer. Optimization of design would result in extraction of high proportions of heat energy from the poorly conducting hot gas. Cost and weight considerations limit the usability of highly conductivity materials for e.g. Copper for bulk production
- 5) Engine Radiator – The coolant system needs to be redesigned to handle extra heat rejection from the cold junction of the thermoelectric modules. Car radiator size needs to be increased to enhance heat transfer to ambient air.

- 6) Weight and Cost of device – As mentioned above, weight and cost are too major roadblocks for development of thermoelectric generators on a mass scale production. Expensive thermoelectric materials and heavier TEGs will not help in reasonable fuel savings over a normal usage period of an automobile.

1.4 Literature Survey

A comprehensive theoretical study concluded that a TEG powered by exhaust heat could meet the electrical requirements of a medium sized vehicle [1]. Yang [4] argues that thermoelectric technology has the ability to draw on as much as tens of kilowatts of heat losses in vehicles, providing a substantial thermal energy reservoir. As automobile exhaust gases are typically of the range of 400-800°C, high temperature thermoelectric devices are required for at least part of the flow path.

Inclusion of a TEG in the exhaust system imposes additional pressure drops due to the viscous drag on the fin surfaces and cross-sectional area changes. High pressure drops can lead to considerable loss in fuel economy. Also, power generation from a TEG strictly depends on engine driving conditions. Large variations in exhaust temperatures and gas flow rates present challenges in the proper conditioning of any electric power generated. Finally, the cost effectiveness of TE materials and the additional weight of the TEG [5] are other constraints that make system level modeling and commercialization a daunting task.

Thermoelectric generators have relatively low efficiency (typically around 5%) and have, historically, had restricted usage in specialized medical, military and space applications [6]. Thermoelectric converters have been used in deep space probes since the

1950's due to the ease of scalability and the overall simplicity as compared to alternative approaches [7]. However, the recent improvements of the energy conversion efficiencies [4,8–10] of TE materials, combined with increased interest in energy efficiency and fuel economy, has led to an unprecedented increase in research into their potential deployment in environments where heat energy is free or cheap like solar radiation [11,12], automobile exhaust [13–15], gas turbines and diesel cycle cogeneration systems [16], etc. In situations where the supply of waste heat is freely available, efficiency of conversion is not an overriding consideration and things such as simplicity, scalability and packaging are more important. Environmental regulations and increasing energy costs indicate a significant role for waste heat generators in automobiles [9]. Morelli [18] assessed critical issues considered for exhaust gas generator design such as location, heat transfer from exhaust, generator mass, thermoelectric stability, and overall environmental friendliness. It was emphasized that internal finning and diffuser arrangement in the TEG system are important to minimize the temperature difference between the hot gas and the hot side of the thermoelectric device.

1.4.1 Thermoelectric Generator Design

The first automotive exhaust TEG was constructed in 1963 [19]. In the second half of the last century, prototypes were developed by Porsche [19], Hi-Z [20,21], Nissan Motors [22], and Clarkson University in collaboration with GM [23,24]. All of these TEGs have used exhaust gases and engine coolant as the heat source and sink, respectively. Hsiao et al. [25] built a one-dimensional thermal resistance model for a TEG and found the performance on the exhaust pipe is better than on the radiator. Karri et al [26] highlighted

the use of a thermoelectric generator placed in the exhaust stream of a sports utility vehicle (SUV) and a stationary, compressed natural gas (CNG) fueled engine generator set. Kim et al [28] has proposed a low heat temperature TEG model which works on engine coolant as the source and that could replace a conventional radiator without any additional components. Numerical models [28–30] have been developed to assess TEG performance at various engine operating conditions using plate/fin heat exchangers and commercial Bi_2Te_3 based modules.

A diesel engine TEG application modeled by Espinosa et al [15] was composed of $\text{Mg}_2\text{Si}/\text{Zn}_4\text{Sb}_3$ for high temperatures followed by Bi_2Te_3 for low temperature. It was shown that for exhaust gas temperatures in the range of 250-350°C, the use of only high temperature modules could be a simple and cost-effective solution. Their work addresses the effect of the number of thermoelectric elements and electrical connections. Other work by Yu et al [1] has proposed a system for output electrical power conditioning to maximize power transfer to charge the battery under different working conditions. Researchers at BMW obtained 200 W of electrical power from a TEG comprising 24 Bi_2Te_3 modules in a 3 L engine driven BMW 535i vehicle at 130 km/h [5,31]. Crane et al [32] have mentioned the evolution from planar topology of TEG to a cylindrical shape during phase 3-4 of TEG design of BSST¹ led US DOE project implemented in 6 cylinder inline BMW engine at the National Renewable Energy Laboratory (NREL) in Golden Colorado. The bench test of BSST's cylindrical TEG designed for the Ford Lincoln MKT and the BMW X6 has reported electrical power generation exceeding

¹ BSST is a wholly owned subsidiary of Amerigon dedicated to the advancement of thermoelectric research in the areas of both temperature control and power generation.

700W [33]. General Motors mentioned that achieving 350 W and 600 W is possible when operating a Chevrolet Suburban under city and highway driving conditions, respectively, with an average of 15 kW of heat energy was available over the drive cycle [34]. Meisner has outlined the General Motors progress the in development of various phases of TEG prototypes by using Bi-Te and Skutterudite modules in the Chevrolet Suburban vehicle [35,36].

The overall performance of a TEG is not only determined by the figure-of-merit or ZT of the TE materials, but more importantly the overall thermal profile in a TEG. There is a large temperature drop from the hot gas to the TE modules and then to the coolant, as well as along the flow direction. Xuan et al. [37] employed a phenomenological model to study the effects of internal and/or external interface layers on thermoelectric devices performance. Liang et al [38] have discussed the effect of thermal and electrical contact resistances on power output from a thermoelectric generator with modules connected in parallel to a single load resistor. Improved thermal interface materials hold the promise of maximizing heat conduction on both sides of the thermoelectric modules (TEM) [39–41].

Table 1.1. Previous efforts in Automotive TEG prototype development.

No.	Reference	Automobile	Electric Power	TE Technology
1	Birkholz [19] (1988)	Porshe 944 engine	58W	90 FeSi ₂ thermoelements
2	Bass et al [20,21] (1994)	Cummins NTC 350 Class 8 diesel engine	1068 W	72 Hi-Z TEMs (13W) based on Bi ₂ Te ₃
3	Ikoma et al [22] (1998)	3000 cc gasoline engine (Nissan Motors)	35.6W	72 TEMs based on B and P doped Si ₂ Ge
4	Matsubara [42,43] (2002)	2000 cc Toyota Estima	266W	6 segmented TEMs (Skutterudites / Bi ₂ Te ₃) and 4 HZ-14 TEMs (based on Bi ₂ Te ₃ from. HI-Z Technology, Inc.)
5	Thatcher [23,24] (2007)	1999 GMC Sierra pickup truck	170 W	16 HZ-20 TEMs (based on Bi ₂ Te ₃ from. HI-Z Technology, Inc.)
6	Eder [31] (2009)	3L twin-turbo gasoline engine BMW 535i	200W	24 TEMs based on Bi ₂ Te ₃
7	Crane (BSST) [32] (2009)	3L BMW inline 6 cylinder with two turbocharger	125W	2 stage segmented TE elements (half-Heusler alloy(Zr, Hf based), Bi ₂ Te ₃) near hot gas inlet and Bi ₂ Te ₃ elements near exit
8	Kim et al [27] (2010)	Placed on radiator of 2L engine SUV	75W	72 TEMs based on Bi ₂ Te ₃
9	Meisner [35,36] (2011)	GM Chevrolet Suburban	30W/TEM near inlet and 15W/TEM near rear end	42 Bi ₂ Te ₃ based TEMs (phase 2-prototype)

1.4.2 Thermoelectric Material

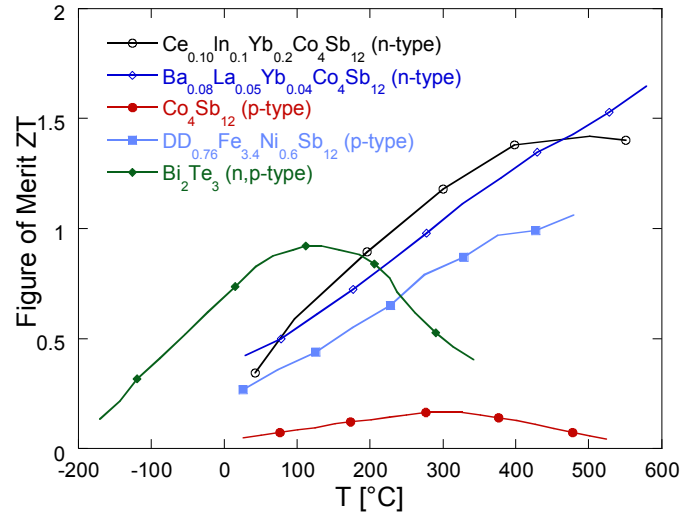


Figure 1.6. ZT curve for thermoelectric materials [8–10,44,45].

Over the last several decades, alloy-based TE materials including $\text{Bi}_2\text{Te}_3 - \text{Sb}_2\text{Te}_3$ and Si-Ge systems have been extensively studied and optimized for use in their different temperature ranges [3,4,46]. TEMs based on FeSi_2 [19], PbTe [47] have been used for the exhaust generators. 6-8% conversion efficiency was estimated for the segmented TE modules with a $\Delta T = 560^\circ\text{C}$ [38]. Bass et al [20,21] constructed a 1 kW thermoelectric generator based on bismuth telluride technology operated using the turbo exhaust outlet of a 14-L Cummins NTC 275 diesel engine. Recently, interest has renewed in the investigation of new and more efficient TE materials, in particular, nano-scale materials [4] including super-lattice structures [4], nanowires [39,40], quantum dots [4], and nanostructured-bulk alloys [4]. Increased materials efficiency has been realized by taking advantage of electronic band structure engineering [4,49] and phonon engineering [3, 39]. When integrated into automotive exhaust systems, the potential exists for fuel savings approaching 5%. Matsubara [14,43] made a high efficient thermoelectric stack TEG for

automobiles composed of segmented legs using highly doped CoSb_3 and filled skutterudites $\text{RM}_4\text{Sb}_{12}$ ($\text{R} = \text{Ce, Yb}$; $\text{M} = \text{Co, Fe, Ni, Pt, Pd}$) followed by HZ-14 modules and achieved 5% to 10% efficiency, depending on engine operating conditions. The operating range was 350-750°C and it was demonstrated that $ZT = 1.5$ to 2.0 will be needed to attain a goal of 10% overall efficiency.

Established TE semiconductors exhibit poor figures of merit operating temperatures exceeding 500°C [3,46]. Recent research in high performance multiple filled skutterudites [8,9] has shown $ZT > 1.5$, for n-type materials, at high temperatures as shown in Figure 1.6. Additionally, skutterudites have higher performance than standard Bismuth-Telluride devices at temperatures above 200°C.

As discussed by Hendricks et al. [50] a thermoelectric generator should be studied as an integrated solution. The reason is that thermoelectric material properties and heat exchanger performance are closely linked. As most of the prior efforts have explored installation of the TEG on an existing vehicle, there were limitations in the volume and topology of the TEG. In the present study, we explore optimal TEG designs assuming a rectangular topology with a fixed volume constraint. In addition, this work explores the potential to use hybrid TEGs with skutterudites being applied in highest temperature regions and Bismuth Telluride modules in regions where their output exceeds that of skutterudites modules.

1.5 Motivation

The challenges associated with the development of thermoelectric technology for application in automobiles create numerous venues for further research. The upcoming research activities in thermoelectric materials and new improvements like topological study and heat exchanger optimization, altogether, make this an interesting problem.

- 1) Advent of multiple filled Skutterudites [8,44,45] with enhanced nanostructure and operating temperatures close to the automobile vehicle exhaust temperature have demonstrated higher ZT performance (Figure 1.7) and promises to be a good thermoelectric material for application of interest .

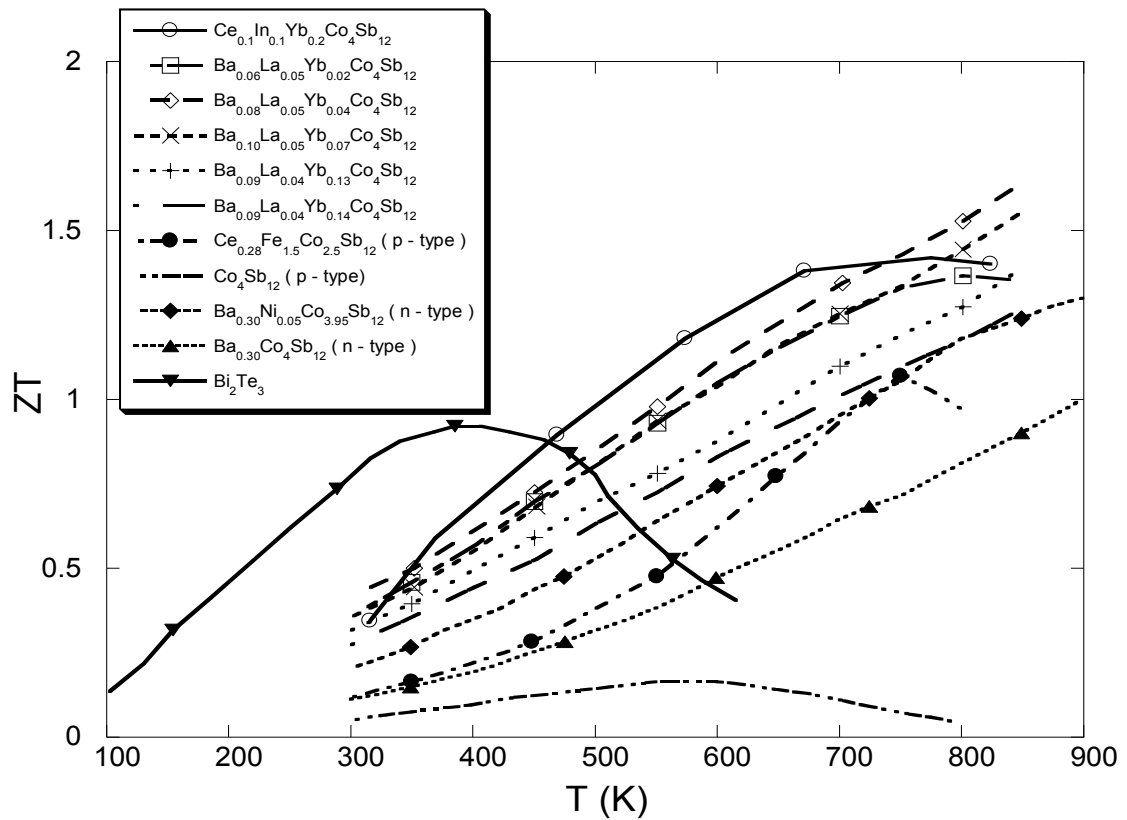


Figure 1.7. Figure of Merit ZT values for Thermo-electric materials [8,44,45].

- 2) The study of various possible topologies for thermoelectric generator has been overlooked till date and not given due importance in existing literature. Analysis of various topologies ranging from rectangular, hexagonal and circular could lead to highly efficient thermoelectric modules arrangement and bypass pipe design.
- 3) Optimized heat exchanger integrated in selected topology could provide high heat transfers with incurred pressure drop within the predefined limits for internal combustion engines.

As evident from Figure 1.7, thermoelectric modules exhibit higher ZTs for selected range of temperature. Hybrid arrangement of thermoelectric modules on the hot surfaces could be much beneficial resulting higher system efficiencies.

1.6 Objectives of Present Study

The current study focusses primarily on following main objectives:

- 1) Maximization of electrical power generation for a given volume by study and comparison of various topologies – rectangular, cylindrical and hexagonal ducts for thermoelectric generators with provision of a bypass system.
- 2) Optimization of heat exchanger configurations for maximization of electric power generation with induced engine back pressure within the predefined limit.
- 3) Study of hybrid combinations of thermoelectric modules – Skutterudites and Bismuth Telluride for placement on hot surfaces of thermoelectric generator.
- 4) Optimization of geometric configurations of thermoelectric modules to maximize electric power generation for automotive heat transfer profiles.
- 5) Modeling axial conduction effects in liner and analyze associated impact on TEG performances.

1.7 Thesis Organization

Chapter two describes the system level developed to assess the performance of various TEG configurations. TE types, heat exchanger designs and overall TEG topologies. Chapter three summarizes the results of the TEG optimization for rectangular, cylindrical and hexagonal topologies. Chapter four presents thermoelectric design study for skutterudite based thermoelectric modules. Chapter five investigates axial conduction effects in hot wall lining and its impact on TEG performance. Chapter six presents thesis summary and topics for future investigation.

CHAPTER 2. THERMOELECTRIC GENERATOR MODEL

2.1 Modeling of Thermoelectric Generator System

Various topologies were considered for the shape of thermoelectric generator ranging from rectangular box to circular cylinders. The thermoelectric generator system can be visualized a network of thermal resistances. Thermoelectric components can be modeled as equivalent thermal resistances. The generator is discretized into small control volumes distributed along the flow direction. Detailed description of design models will be explained later in this chapter. Here are the basic assumptions taken as a part of modeling

2.1.1 Assumptions

Below are the important assumptions for system level modeling:

- 1) 1-D steady state analysis of fluid flow is considered with flow direction along length being the dimension with variation.
- 2) The exhaust gas is assumed to be air with temperature dependent properties
- 3) The variation in fluid properties and thermoelectric properties with temperature is along considered along the flow direction

- 4) The convection heat transfer between the thermoelectric legs and the top surface of the generator is neglected.
- 5) Thomson effect is not taken into consideration
- 6) Temperature averaged over junction temperatures are used to compute thermoelectric properties for each legs
- 7) Uniform distribution of thermoelectric couples over the entire available module surface.
- 8) The contact electrical resistance at the copper conductive tabs in the thermoelectric couple is not considered.

2.1.2 Volume Discretization

The thermoelectric generator domain is discretized in to small control volumes along the exhaust flow direction. The temperature is assumed to be uniform inside the control volume. Inside a control volume, the available hot surface is designated as A_{Base} . 80% of A_{Base} is assumed to be covered by uniform distribution of thermoelectric modules represented as A_{module} . The number density of thermoelectric couples is known a-priori for commercial thermoelectric modules and hence the approximate number of thermoelectric n-p legs can be computed for the each control volume represented as A_{module} .

$$n_{CV,TEC} = \text{NumberDensity} * A_{Module} \quad (2.1)$$

The remaining 20% of A_{module} is considered to be covered by thermal insulation represented as A_{Ins} . The symmetry in flow region helps in simplifying the domain under

investigation. For e.g. longitudinal topology has a central symmetry; hence only a upper half domain is simulated. The modeling of thermal resistance network is explained in details in following section.

2.1.3 Thermal Resistance Network

The thermoelectric generator system can be modeled as thermal resistance network. The thermal circuit for a typical thermoelectric generator system is shown in a schematic (Figure 2.1).

The hot side heat exchanger assembly can be modeled as an effective thermal resistance given by Eq. (2.2). Fin resistance modeling for plate fin heat exchanger assembly can be found in Incropera [51]. Here η_0 is the overall fin effectiveness; A_t is the total area of the heat exchanger i.e. fin surface area and the base area in a control volume. \bar{h}_g is the average heat transfer coefficient and is based on fin channel Reynolds number. The thermal resistances for top surface of the device, ceramic slab, thermal grease and the insulation can be given by Eq. (2.1) - (2.5).

$$R_{fin,eq} = 1 / (\eta_0 \bar{h}_g A_t) \quad (2.2)$$

$$R_{TEG,base} = t_{base} / (\kappa_{base} A_{base}) \quad (2.3)$$

$$R_{ceramic} = t_{ceramic} / (\kappa_{ceramic} A_{Module}) \quad (2.4)$$

$$R_{grease} = t_{grease} / (\kappa_{grease} A_{Module}) \quad (2.5)$$

$$R_{Ins} = t_{Ins} / (\kappa_{Ins} A_{Ins}) \quad (2.6)$$

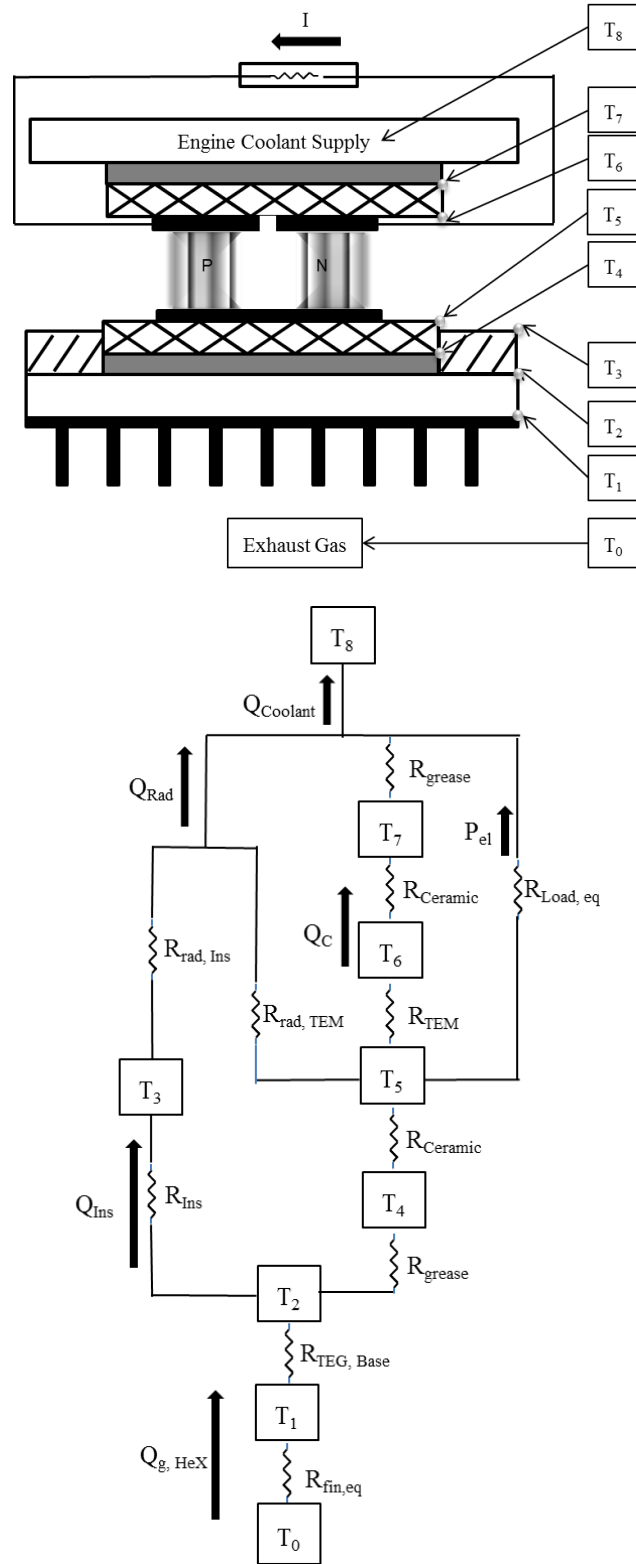


Figure 2.1. Thermal resistance network and temperature locations

Radiation heat transfer is considered for hot exposed surfaces i.e. insulated top surface and the part of thermoelectric modules' hot surface not covered by the TE legs. The expressions for radiation heat transfer coefficient and the radiation resistances for these surfaces are given by Eq. (2.7) - (2.10). Here, A_{TEC} and A_{Ins} are the areas of a TE couple and thermally insulated surface in a control volume respectively.

$$R_{rad,Ins} = 1 / (h_{rad,Ins} A_{Ins}) \quad (2.7)$$

$$R_{rad,TEM} = 1 / [h_{rad,TEM} (A_{Module} - n_{CV,TEC} A_{TEC})] \quad (2.8)$$

$$h_{rad,TEM} = \varepsilon_{TEM} \sigma (T_5^3 + T_5^2 T_8 + T_5 T_8^2 + T_8^3) \quad (2.9)$$

$$h_{rad,Ins} = \varepsilon_{Ins} \sigma (T_3^3 + T_3^2 T_8 + T_3 T_8^2 + T_8^3) \quad (2.10)$$

The thermoelectric properties of n and p legs are the functions of temperature. The properties are averaged over the junction temperatures. The properties seebeck coefficient (S), thermal conductance (K), internal electrical conductance (R_{el}) can be computed for a thermoelectric couple as given by Eq. (2.11) - (2.13).

$$S_{TEC} = S_p - S_n \quad (2.11)$$

$$K_{TEC} = \frac{\kappa_p A_p}{L_p} + \frac{\kappa_n A_n}{L_n} \quad (2.12)$$

$$R_{el,TEC} = \frac{L_p \rho_p}{A_p} + \frac{L_n \rho_n}{A_n} \quad (2.13)$$

$$ZT_{TEC} = \frac{\langle S_p - S_n \rangle^2 T}{\left[\langle \rho_p \kappa_p \rangle^{1/2} + \langle \rho_n \kappa_n \rangle^{1/2} \right]^2} \quad (2.14)$$

Similarly, ZT for a thermocouple can be computed as shown in Eq. (2.14). Equivalent thermal resistances for thermoelectric components can be defined by manipulation of equations. Across the thermocouple junction, open circuit voltage can be defined as:

$$V_{oc} = S_{TEC} (T_5 - T_6) \quad (2.15)$$

The electrical current through the thermocouple, connected to an external electrical load resistance ($R_{el,L}$), can be specified as

$$I = \frac{V_{oc}}{(R_{el,L} + R_{el,TEC})} \quad (2.16)$$

Hence, the heat transfer from the hot side and cold side of the thermocouple junction system is given as:

$$Q_H = S_{TEC} T_5 I - \frac{1}{2} I^2 R_{el,TEC} + K_{TEC} (T_5 - T_6) \quad (2.17)$$

$$Q_C = S_{TEC} T_6 I + \frac{1}{2} I^2 R_{el,TEC} + K_{TEC} (T_5 - T_6) \quad (2.18)$$

And the electrical power output across the external load resistance is given as difference of Eq. (2.17) and Eq. (2.18).

$$P_{el,TEC} = Q_H - Q_C = I^2 R_{el,L} \quad (2.19)$$

Hence, the thermal resistances are modeled to complete the network branches along path 5-8 in Figure 2.1. Since, the thermal energy transfer through these thermoelectric couples is in a parallel fashion; their contribution in a control volume can be summed up in an equivalent module resistance given as:

$$R_{TEM} = \frac{(T_5 - T_6)}{n_{CV,TEC} (Q_H - P_{el,TEC})} \quad (2.20)$$

Whereas equivalent load resistance for branch 5-8 can be written as:

$$R_{Load,eq} = \frac{(T_5 - T_8)}{n_{CV,TEC} P_{el,TEC}} \quad (2.21)$$

Similarly, the thermal resistances in the branches 0-2 and 2-8 (insulation and TEM) can be added up together for a thermal circuit as:

$$R_{02} = R_{fin,eq} + R_{TEG,Base} \quad (2.22)$$

$$R_{28,Ins} = R_{Ins} + R_{rad,Ins} \quad (2.23)$$

$$R_{28,TEM} = R_{grease} + R_{ceramic} + \left(\begin{array}{c} R_{rad,TEM}^{-1} + \\ \left(R_{TEM} + R_{ceramic} + R_{grease} \right)^{-1} \\ + R_{Load,eq}^{-1} \end{array} \right)^{-1} \quad (2.24)$$

Using the resistances in the top and bottom branches, an explicit expression for T_2 in terms of T_0 and T_8 can be derived as:

$$T_2 = \frac{T_0 R_{02}^{-1} + T_8 \left(R_{28,Ins}^{-1} + R_{28,TEM}^{-1} \right)}{R_{02}^{-1} + \left(R_{28,Ins}^{-1} + R_{28,TEM}^{-1} \right)} \quad (2.25)$$

For the topologies with symmetry like longitudinal flow model, gas bulk temperature at the end of each i^{th} CV boundary can be computed from energy balance as:

$$T_{g,i+1} = T_{g,i} - Q_{g,HeX} / \left(\left(\dot{m}_g / 2 \right) C_{P,air} \right) \quad (2.26)$$

Table 2.1. Inputs required in thermal resistance network.

Parameters	Value	Unit
Geometry		
Thermoelectric Generator Volume	0.003592	m ³
Exhaust Inlet and Outlet Pipe Diameter	0.0635	m
Dimensions for Rectangular topology [length, height, width]	[0.01 – 2.0, 0.01 - 0.35, 0.01 - 1.2]	[m, m, m]
Dimensions for Circular topology [Outer Diameter, Inner diameter]	[0.05 – 0.20, 0.01 - 0.04]	[m, m]
Fins (Copper) [thickness, spacing] Thermal conductivity	[1 - 8, 1 - 8] 401	[mm, mm] Wm ⁻¹ K ⁻¹
Thermoelectric Module		
Skutterudite Module [Cross-section, Height] TEC [N _{TEC} , Cross-section, Height]] ϵ_{Module} Thermoelectric Material	[0.0508 x 0.0508, 0.007] [32, 0.002x0.002, 0.004] 0.55 Ba _{0.08} La _{0.05} Yb _{0.04} Co ₄ Sb ₁₂ (n type)[8] DD _{0.76} Fe _{3.4} Ni _{0.6} Sb ₁₂ (p type) [9]	[m ² , m] [-, m ² , m] [-] [-] [-]
Bismuth Telluride Module [Cross-section, Height] TEC [N _{TEC} , Cross-section, Height] ϵ_{Module} Thermoelectric Material	[0.04013 x 0.04013, 0.004] [127, 0.004x0.004, 0.002] 0.55 Bi ₂ Te ₃ [10]	[m ² , m] [-, m ² , m] [-]
Fluid		
Air Properties	Ideal gas Formulation [EES]	[-]
Materials		
Thermal Grease (Grafoil Laminate) Gap Thermal conductivity	0.001 5	m Wm ⁻¹ K ⁻¹
Thermal Insulation (Min-K)[52] Gap Thermal conductivity ϵ_{Ins}	0.002 0.0334 0.75	m Wm ⁻¹ K ⁻¹ [-]
Thermoelectric Base (Copper) Thickness Thermal Conductivity	0.008 401	m Wm ⁻¹ K ⁻¹

2.1.4 Pressure Drop Calculations

The fluid flow across the thermoelectric generator induces pressure drops throughout. The changes in cross-sections at entry port i.e. exhaust inlet pipe to TEG and exit port lead to pressure drop or gain depending on the area ratios at the transition. The pressure drop is calculated using Borda-Carnot Eq. (2.27) and Eq. (2.28) [49]. Due to turbulent flow pipe regime for mass flow rate 20-100g/s ($Re = 12000-60000$), flow transition between exhaust pipe and TEG cross-section can be approximated as sudden expansions or contractions. The expressions for pressure change across sudden expansion (Exp) and contraction (Con) from section 1 to 2 are given as follows:

$$\Delta P_{Exp} = -d_{air} \frac{A_1}{A_2} \left(1 - \frac{A_1}{A_2} \right) v_{air,1}^2 \quad (2.27)$$

$$\Delta P_{Con} = \frac{1}{2} d_{air} \left(\frac{1}{\mu} - 1 \right)^2 \left(\frac{A_1}{A_2} \right)^2 v_{air,1}^2 \quad (2.28)$$

$$\mu = 0.63 + 0.37 \left(\frac{A_2}{A_1} \right)^3 \quad (2.29)$$

The viscous drag effect on the fin surfaces adds to the pressure drop along the length of the TEG. Pressure drop across the heat exchanger assembly given in Eq. (2.30) is calculated by computing friction factor f based on Reynolds number and hydraulic diameter of a fin channel for a given aspect ratio [51]. The friction factor depends on the fluid flow regime.

$$\Delta P_{HeX} = \sum_{CV} f \Delta x_{CV} d_{air} \frac{v_{ch,air}^2}{2} \quad (2.30)$$

2.1.5 Solution Methodology

Since, the non-linear thermal resistances depend on thermoelectric material properties and its terminal temperatures, the temperatures in the thermal circuit must be solved in an iterative manner. The thermoelectric properties and thermal resistances are updated at each iteration step until the temperatures don't change beyond a tolerance value (10^{-6}). The solution consists of two iteration loops: inner and outer iteration. Outer iteration loop runs until the gas bulk temperature is converged for each control volume. Inner iteration loops until the temperature and resistances values converge within a control volume based on the mean gas bulk temperature supplied by outer iteration loop. The sequence of solution of equations for the control volumes is as follows:

- 1) Initialize coolant temperature (T_{coolant}), inlet gas bulk temperature ($T_{g,i}$) and mass flow rate (\dot{m}).
- 2) Assume gas bulk temperature at the end of i^{th} CV ($T_{g,i+1}$).
- 3) Outer Iteration Loop-
 - a. Compute mean gas bulk temperature as given in Eq. (2.31) and pass it to inner iteration loop.

$$T_{g,i,\text{mean}} = (T_{g,i} + T_{g,i+1}) / 2 \quad (2.31)$$

- b. Inner Iteration Loop:
 - i. Assume T_2 and other temperatures (based on T_2 for first iteration) inside a CV based on $T_{g,i,\text{mean}}$ and T_{coolant} .
 - ii. Compute thermoelectric parameters and resistances based on these temperatures
 - iii. Compute T_2 in Eq. (2.25) and compute relative error from Eq. (2.32)

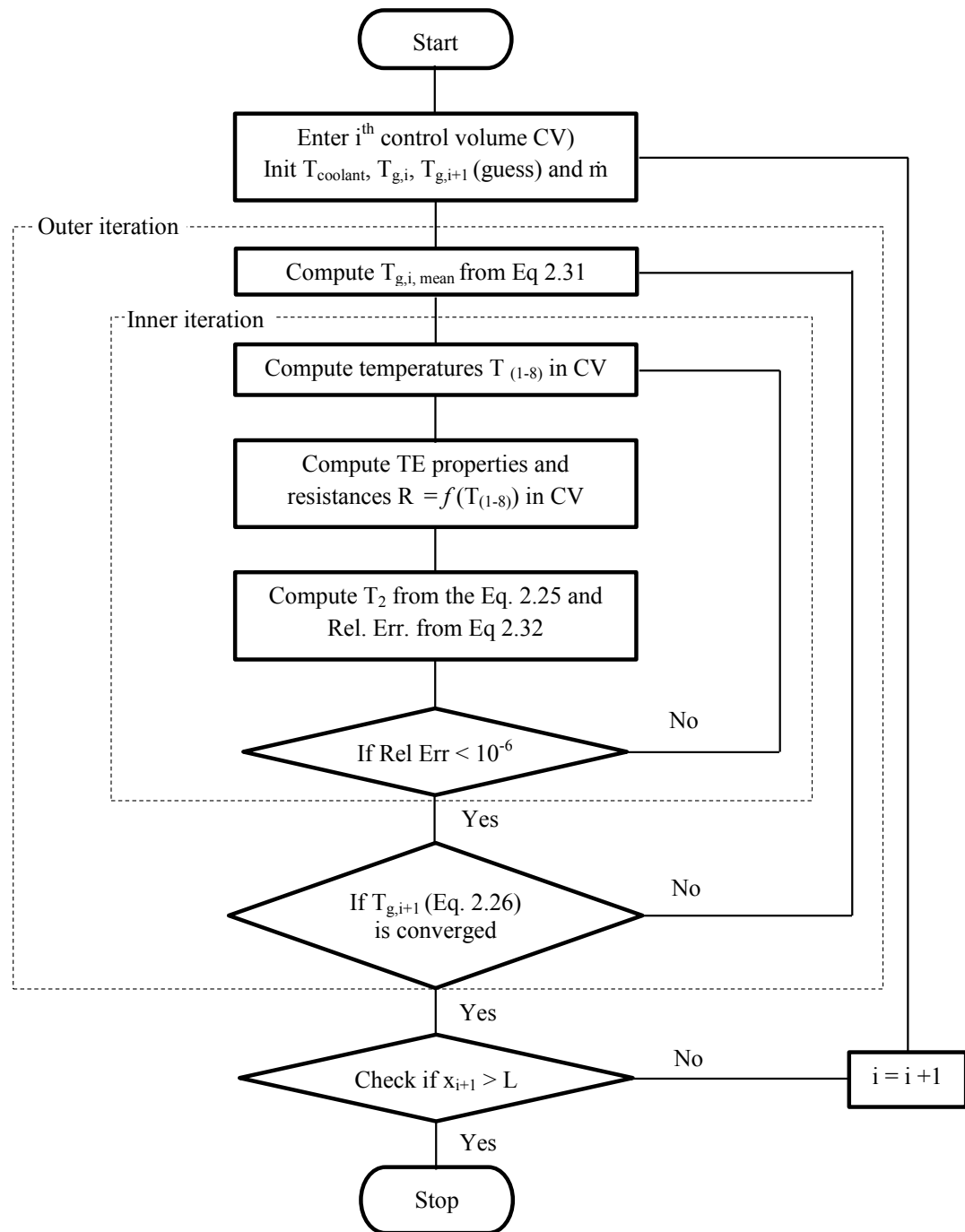


Figure 2.2. Flowchart for the solution methodology.

$$\text{Rel. Err.} = \sum \left| \frac{R_j - R_{j+1}}{R_j} \right| + \sum \left| \frac{T_j - T_{j+1}}{T_j} \right| \quad (2.32)$$

Check for convergence i.e. if relative error $< 10^{-6}$

iv. If converged, compute $T_{g,i+1}$ using Eq. (2.26) and exit the inner iteration loop

v. If not converged, update temperatures and resistances and reiterate for inner loop.

c. Check for convergence for $T_{g,i+1}$, if not, go to step 3

d. If converged, exit the outer loop

4) Proceed to next $i+1^{\text{th}}$ CV and repeat onwards from Step 2

During the solution of thermoelectrical and thermodynamical parameters in the flow domain, parameters like electrical power, heat transfer rates are stored as arrays for post-processing of results.

2.2 Design Model for Thermoelectric Generator

Various designs were modeled for thermoelectric generator for maximization of electrical power output. The designs can be primarily classified into two topologies:

1) Rectangular

a. Longitudinal Flow Configuration

b. Transverse Flow Configuration

2) Circular

a. Hexagonal

b. Cylindrical

2.2.1 Rectangular Topology

The rectangular topology can be divided into two configurations – (i) longitudinal and (ii) transverse. The names signify the arrangement of the thermoelectric modules w.r.t to the parallel exhaust flow in a rectangular topology.

2.2.1.1 Longitudinal Flow Configuration

Salient features:

- 1) The thermoelectric modules are located on the top and the bottom surface of the box and arranged uniformly over the available surface (80% of total surface area) as shown in Figure 2.3
- 2) The remaining 20% area is thermally insulated to minimize heat leakage.
- 3) Lateral walls are thermally insulated.
- 4) Plate fin heat exchanger is integrated inside the box volume.
- 5) The cold side of the modules is cooled by engine coolant system.
- 6) The entry and exit ports of the box are connected to exhaust pipe (not shown in schematic).
- 7) The bypass pipe is attached separately near the inlet to the generator with help of a control valve and is not shown in the design.

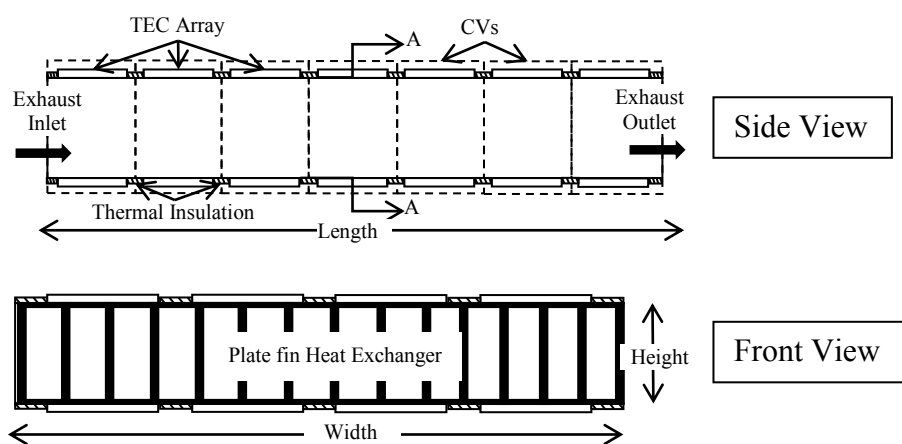
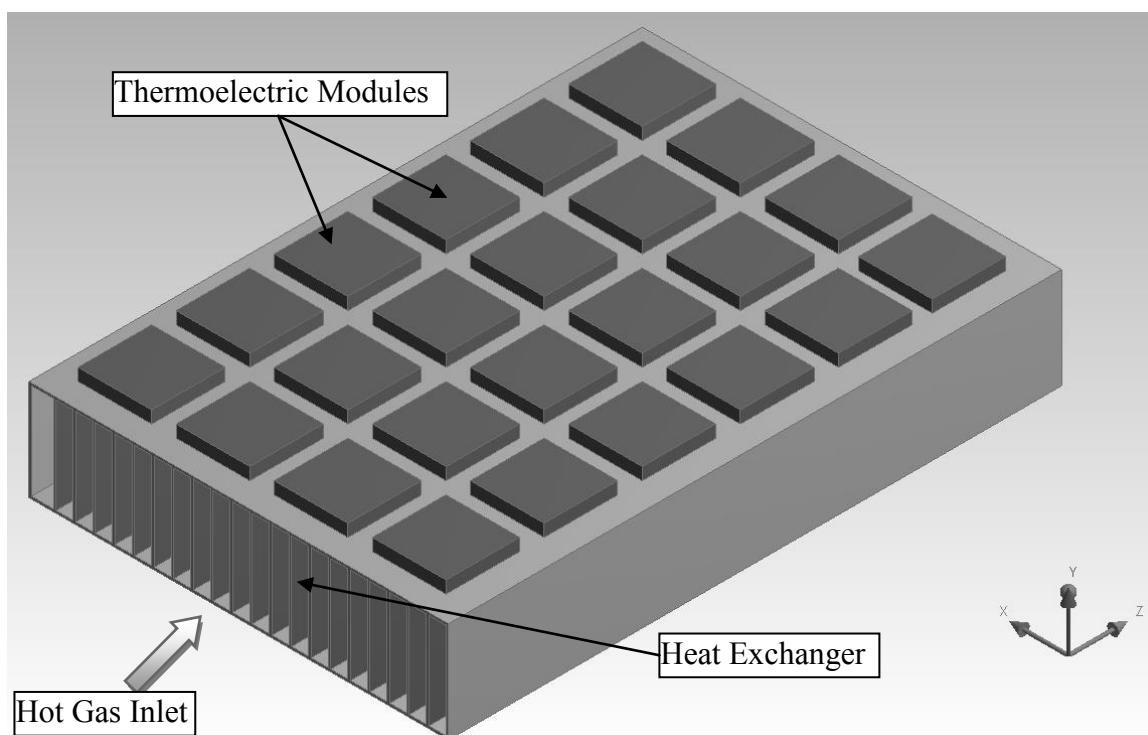
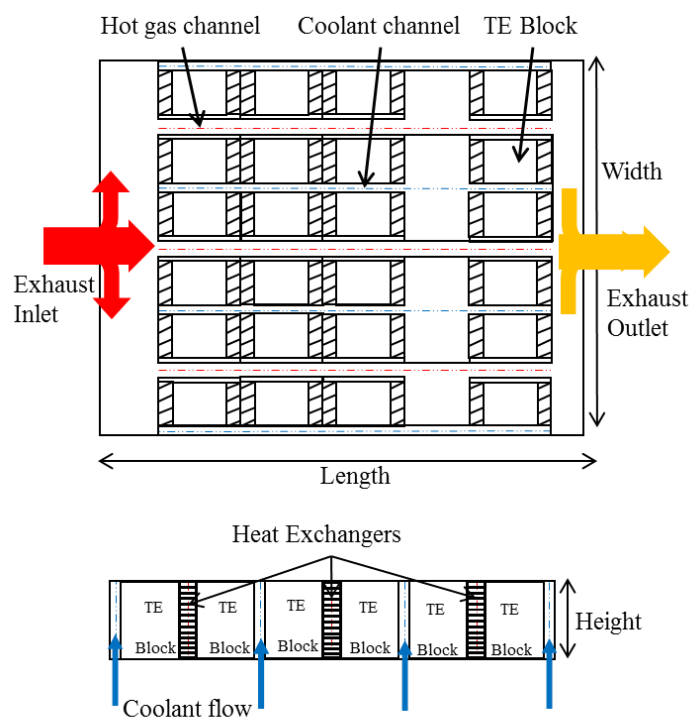
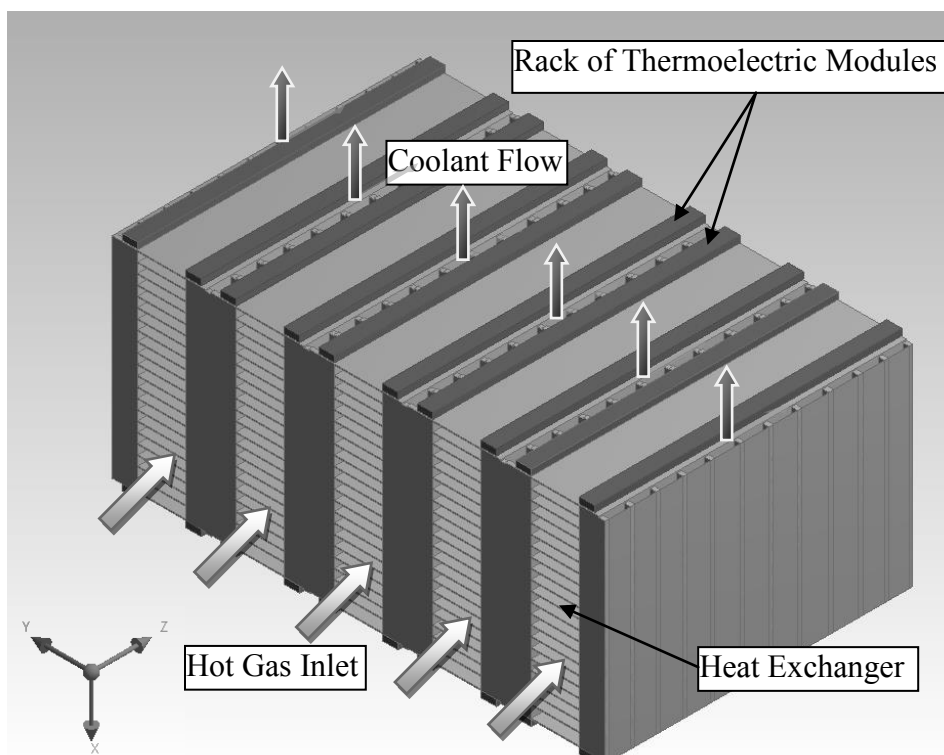


Figure 2.3. Longitudinal Flow Configuration.

2.2.1.2 Transverse Flow Configuration

Salient features:

- 1) The thermoelectric modules are stacked vertically along the flow path inside in the cuboid.
- 2) There are separate channels for hot gas flow (front to back) and coolant flow (bottom to top) as shown in Figure 2.4
- 3) Exhaust gas flow is distributed axially from centrally-located inlet pipe as shown in schematic.
- 4) The hot gas channels are integrated with plate fin heat exchangers as shown.
- 5) Top and bottom walls are thermally insulated
- 6) The bypass pipe is attached separately to inlet supply pipe and is not shown in the generator design.



Top view of TEG (top) and front view (bottom)

Figure 2.4. Transverse Flow Configuration.

2.2.2 Circular Topology

The topologies having circular symmetry are considered as test models in this section. Two types of circular configuration (i) regular hexagon and (ii) cylinder are considered for analysis. The circular configurations have a provision of bypass pipe running axially through the designs.

2.2.2.1 Hexagonal Configuration

Salient features:

- 1) The thermoelectric modules are placed on the outer surface of the hexagonal pipe
- 2) The inner hexagonal pipe acts like a central bypass pipe to offset high temperature effects as shown in Figure 2.5
- 3) The annular region is integrated with plate fins running along the length of the generator.
- 4) Cold side of modules are attached to engine coolant modules (not shown)

2.2.2.2 Cylindrical Configuration

Salient Features:

- 1) The thermoelectric modules are placed on the outer curved surface of the cylindrical pipe
- 2) The inner pipe acts like a central bypass pipe as shown in Figure 2.6
- 3) Plate fin heat exchanger is placed inside the annular region similar to hexagonal configuration
- 4) Cold side of modules are attached to engine coolant modules (not shown)

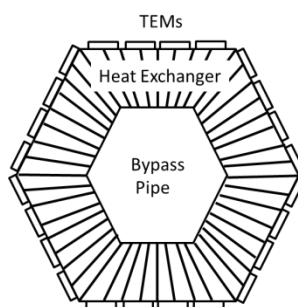
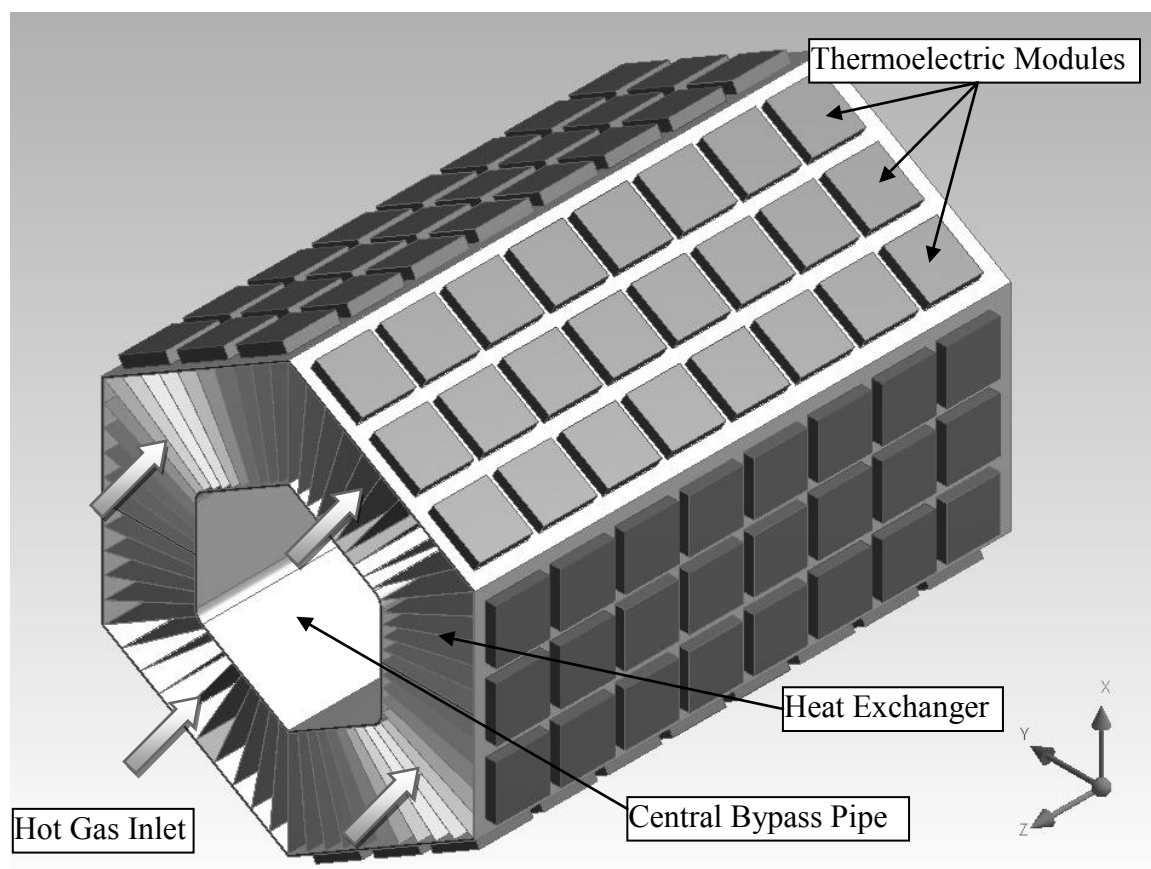


Figure 2.5. Hexagonal Configuration.

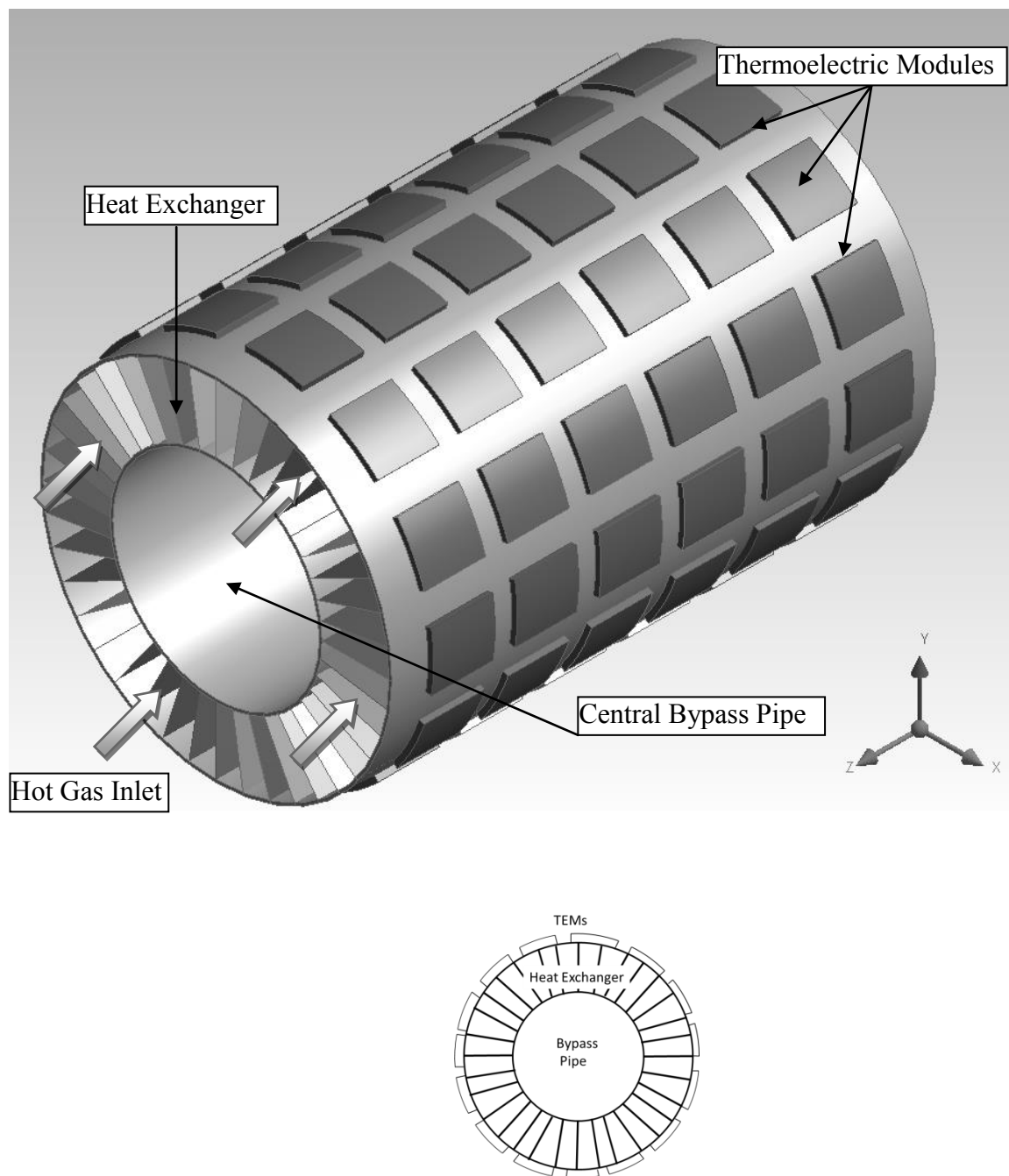


Figure 2.6. Cylindrical Configuration.

2.3 Verification and Validation

This section checks the accuracy and consistency of the C++ code developed for running the test models and formulating the results. The basis for the study was motivated from the General Motors TEG prototype. Due to improper power conditioning and faults in electrical-mechanical assembly integration, the test runs were not successful. The incidents of shortage in electrical lines have been reported by General Motors and power measurements were not accurate. Since, the experimental results are not available till date, it is practically impossible to validate it with a physical case. The code was in fact verified by checking grid independence. The energy balance was too performed on the four test models to verify that the resultant solutions obey energy conservation principles. The inlet conditions were $\dot{m}_{in} = 35 \text{ g/s}$ and $T_{in} = 550^\circ\text{C}$.

2.3.1 Grid Independence

The numerical code was run for a various grid sizes ranging from as coarse as 2 to 128 elements along the flow direction. The physical quantity of interest i.e. electrical power was plotted with the number of grid elements for all four models as shown in Figure 2.7 to Figure 2.10. Grid Independence was run for extreme cases for each of the four models to compute reasonable size of grid element for each model. The generated electric power and the relative error is plotted against increasing grid size for each model in Figure 2.7 to Figure 2.10. The relative error was calculated as:

$$Err_{rel,i} = \frac{P_{el,i-1} - P_{el,i}}{P_{el,i}} \times 100 \% \quad (2.33)$$

The subscript ‘ $i-1$ ’ stands for the coarser grid and ‘ i ’ for the finer grid size. Grid size of 0.001 was found to satisfy the grid independence for most of the cases for each model.

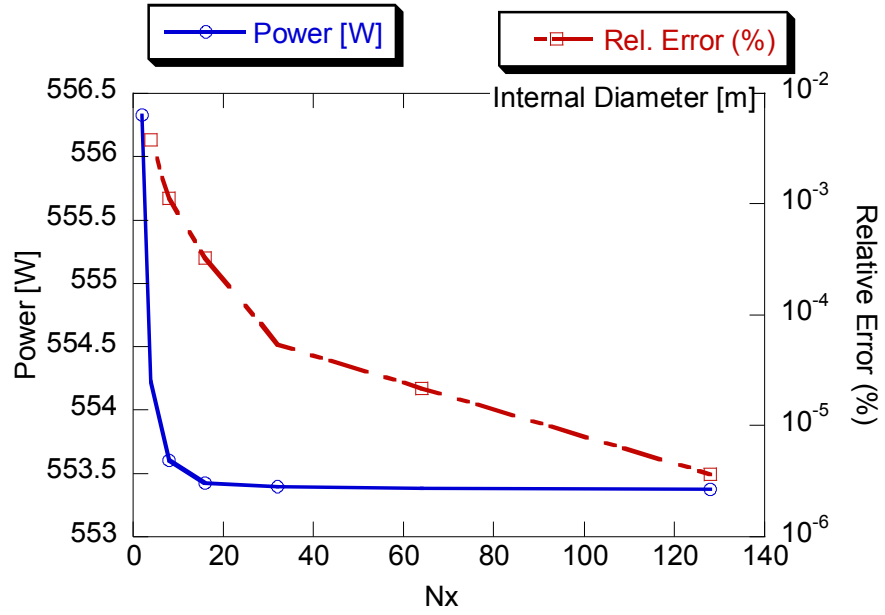


Figure 2.7. Grid Independence study for Longitudinal Flow Model.

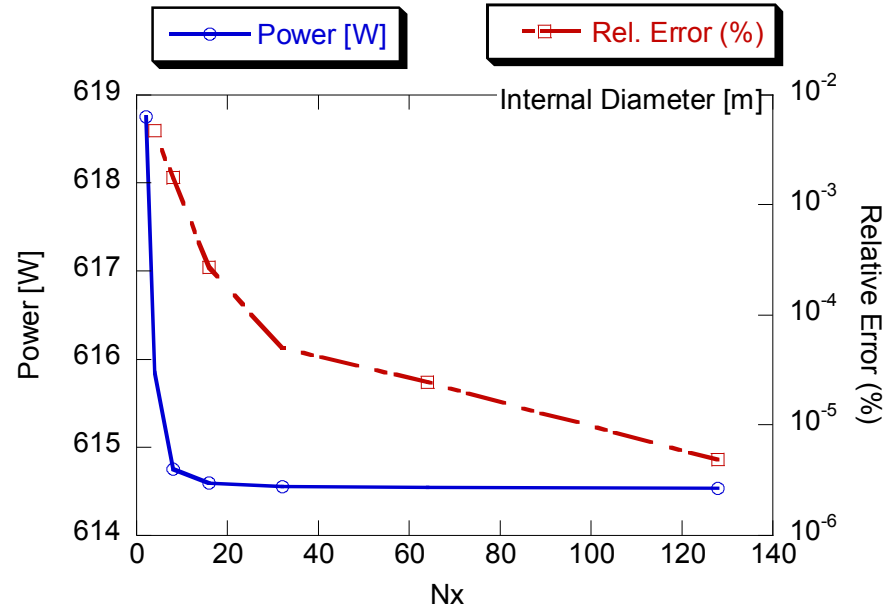


Figure 2.8. Grid Independence study for Transverse Flow Model.

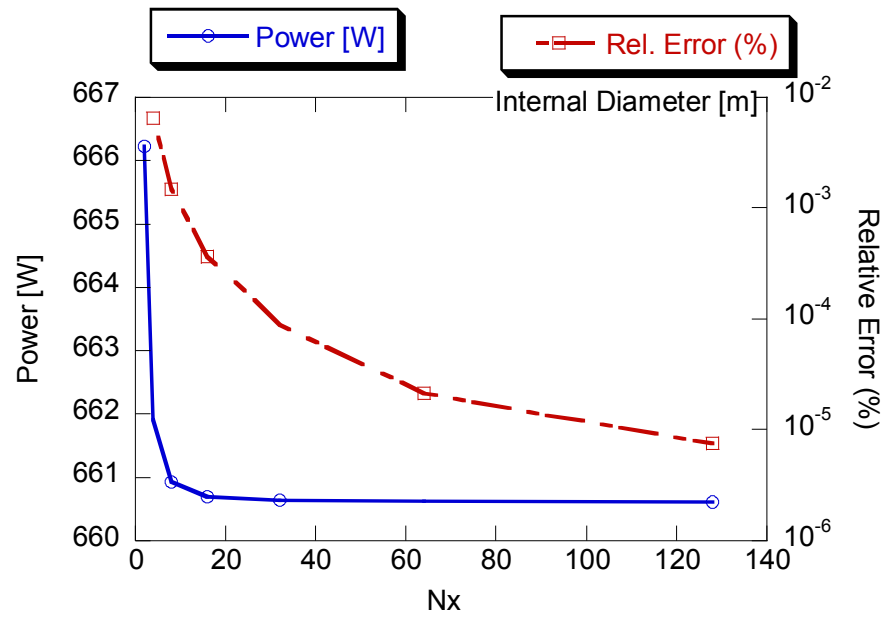


Figure 2.9. Grid Independence study for Hexagonal Model.

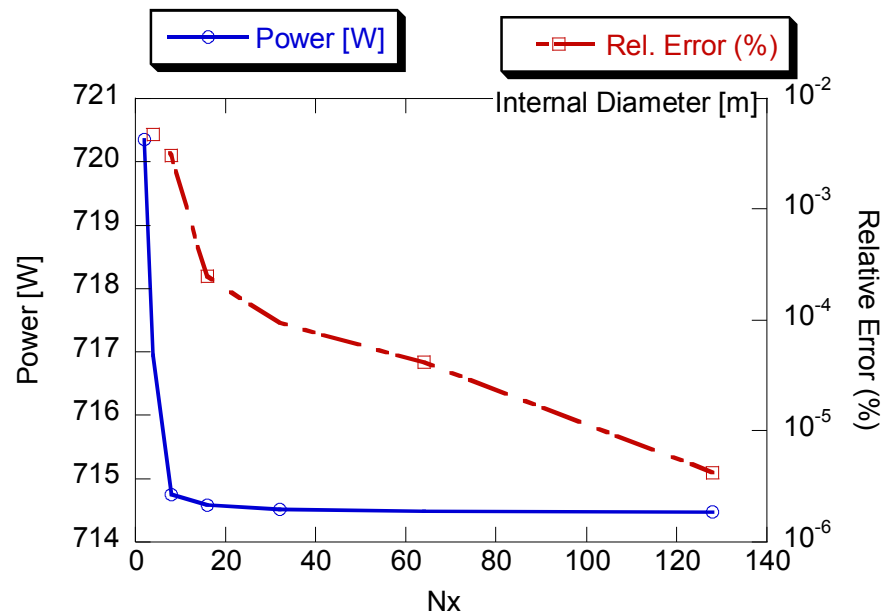


Figure 2.10. Grid Independence study for Cylindrical Model.

2.3.2 Energy Balance

The code was verified to insure basic energy conservation principles. The energy balance was performed for all the four models under analysis. The enthalpy influx rate \dot{H}_{in} is calculated by multiplying air enthalpy at 550°C with mass flow rate of 35 g/s. Similarly, the enthalpy outflow \dot{H}_{out} was calculated at the exit temperatures. The enthalpy change $\Delta \dot{H} = \dot{H}_{in} - \dot{H}_{out}$ is the energy transferred by the gas to the generator. $\dot{Q}_{coolant}$ is the rate at which energy is rejected due to conduction from cold side and the radiation effects. \dot{Q}_{trf} is the sum of generated electrical power (\dot{P}_{el}) and heat rejection ($\dot{Q}_{coolant}$). The energy imbalance (Err) is computed from the difference of \dot{Q}_{trf} and $\Delta \dot{H}$. The relative error (%) for all the models analyzed is less than 0.052 %.

Table 2.2. Energy Balances for four Models.

Model	\dot{H}_{in} [W]	\dot{H}_{out} [W]	$\Delta \dot{H}$ [W]	\dot{P}_{el} [W]	$\dot{Q}_{coolant}$ [W]	\dot{Q}_{trf} [W]	Err [W]	Err [%]
Longitudinal	29669.5	19033	10636.5	553.4	10088.6	10641.9	0.0055	0.052
Transverse	29669.5	20335	9334.5	614.5	8722.5	9337	0.0025	0.027
Hexagonal	29669.5	19792.5	9877	660.6	9220.4	9881	0.0004	0.041
Cylindrical	29669.5	17930.5	11739	714.4	11027.8	11742.2	0.0032	0.027

CHAPTER 3. TOPOLOGY STUDIES AND PERFORMANCE ANALYSIS

The basic models discussed in Section 2.2 were run for various parameters to study their influence on the electrical power generated. This chapter will discuss these results supplemented with analysis on dependence on critical parameters for each model. The chapter is divided into smaller sub sections for the convenience of the readers:

1. Baseline Model
2. Analyzed Topologies
 - A. Rectangular configuration
 - I. Longitudinal
 - II. Transverse
 - B. Circular configuration
 - I. Hexagonal
 - II. Cylindrical
3. Model Comparison

The first subsection discusses results of the baseline model which was developed by General Motors as a part of TEG development. The remaining subsections present analysis primarily based on optimization study of topologies discussed in previous chapter. The inlet flow conditions are described briefly in the next subsection.

3.1 Inlet Conditions

The inlet conditions of hot exhaust gas to the thermoelectric generator depend on engine running conditions. The exhaust data for Chevrolet Suburban vehicle was made available by General Motors, USA. The inlet exhaust mass flow rate ranges from 0 to 100 g/s whereas the inlet temperature varies from 180°C to 700°C. For the sake of simplicity in analysis, the inlet values were averaged over the engine running cycle for steady state analysis. The average mass inlet conditions were calculated as 35 g/s and 550°C.

3.2 User Inputs for Parametric Studies

The inputs chosen for this analysis were taken from the General Model's baseline model. The materials properties used for insulation, thermal grease, etc. were chosen from the baseline model itself. The material properties except thermoelectric materials are assumed to be independent of temperature variation. For thermoelectric materials, look up methods are used to interpolate values from temperature dependent property data tables. The geometrical specifications of prototype skutterudites and commercial Bi_2Te_3 modules from Marlow Industries are used for modeling. The specifications used for the thermoelectric modules were also derived from the same prototype. These user inputs have been presented in Table 3.1.

Table 3.1. User Inputs.

Parameters	Value	Unit
Geometry		
Thermoelectric Generator Volume	0.003592	m ³
Exhaust Inlet and Outlet Pipe Diameter	0.0635	m
Dimensions for Rectangular topology [length, height, width]	[0.01 – 2.0, 0.01 - 0.35, 0.01 - 1.2]	[m, m, m]
Dimensions for Circular topology [Outer Diameter, Inner diameter]	[0.05 – 0.20, 0.01 - 0.04]	[m, m]
Fins (Copper) [thickness, spacing] Thermal conductivity	[1 - 8, 1 - 8] 401	[mm, mm] Wm ⁻¹ K ⁻¹
Thermoelectric Module		
Skutterudite Module [Cross-section, Height] TEC [N _{TEC} , Cross-section, Height] ϵ_{Module} Thermoelectric Material	[0.0508 x 0.0508, 0.007] [32, 0.002x0.002, 0.004] 0.55 Ba _{0.08} La _{0.05} Yb _{0.04} Co ₄ Sb ₁₂ (n type)[8] DD _{0.76} Fe _{3.4} Ni _{0.6} Sb ₁₂ (p type) [9]	[m ² , m] [-, m ² , m] [-] [-] [-]
Bismuth Telluride Module [Cross-section, Height] TEC [N _{TEC} , Cross-section, Height] ϵ_{Module} Thermoelectric Material	[0.04013 x 0.04013, 0.004] [127, 0.004x0.004, 0.002] 0.55 Bi ₂ Te ₃ [10]	[m ² , m] [-, m ² , m] [-]
Fluid		
Air Properties	Ideal gas Formulation [EES]	[-]
Materials		
Thermal Grease (Grafoil Laminate) Gap Thermal conductivity	0.001 5	m Wm ⁻¹ K ⁻¹
Thermal Insulation (Min-K) Gap Thermal conductivity ϵ_{Ins}	0.002 0.0334 0.75	m Wm ⁻¹ K ⁻¹ [-]
Thermoelectric Base (Copper) Thickness Thermal Conductivity	0.008 401	m Wm ⁻¹ K ⁻¹

3.3 Baseline Geometry

The prototype run by General Motors was used as a benchmark model for the current analysis. This prototype was designed for Chevrolet Suburban vehicle [35,36]. The baseline model has a longitudinal configuration in a rectangular topology with skutterudite modules mounted on top and bottom surface of the thermoelectric generator. The basic configuration details of the model and heat exchanger are presented in Table 3.2. The baseline case was run for various input conditions as mentioned in Section 3.1.

Table 3.2. General Motors' baseline model configuration.

Parameter	Value	Unit
Height	38	mm
Width	224	mm
Length	413.1	mm
Fin Thickness	3.3 (Cu)	mm
Fin Spacing	6.35 (Cu)	mm

3.3.1 Effect of Mass flow Rate and Inlet Temperature

The baseline geometry was tested for varying input conditions i.e. mass flow rate and inlet temperature. As mentioned before, these conditions depend on the engine load and will guide the variations in electrical power output during a normal engine running cycle. Figure 3.1 represents the rise in electrical power generation with increasing flow

rate from 20-100 g/s of exhaust gas at $T_{in} = 550^{\circ}\text{C}$. The rise in mass flow rate increases the heat transfer rate from the hot gas through the thermoelectric modules and hence higher electrical power generation. On other hand, increased mass fluxes inside the heat exchanger increase the friction drag forces on the fins and hence increased pressure drop. This upward trend is represented by the Figure 3.2. The calculated pressure drop is found to be lesser than the allowed limit for a Chevrolet Suburban vehicle. However, the current 1D analysis does not account for recirculation effects near the inlet and exit ports arising due to high area ratios. The spatial variation in flow regimes along the width and height of the thermoelectric generator is too neglected; hence this is not the true measure of actual device pressure drop.

The similar trend is observed when the inlet exhaust temperature was varied within the range of 673K – 973K ($400^{\circ}\text{C} - 700^{\circ}\text{C}$) at an average mass flow rate of 35 g/s. as shown in Figure 3.3 The electrical power generation rate increases with increasing inlet temperature. The relatively hotter temperatures in the flow region raises the hot side temperature of the thermoelectric modules and hence higher seebeck potential is generated across the junctions. The variation in pressure drop with the varying inlet temperature is represented by Figure 3.4. The decrease in air density with higher inlet temperatures tends to increase the channel velocities. This explains the slight increase in pressure drop with the inlet exhaust temperature. The allowed limit for back pressure rise is 812 Pa for $\dot{m}_{in} = 35$ g/s.

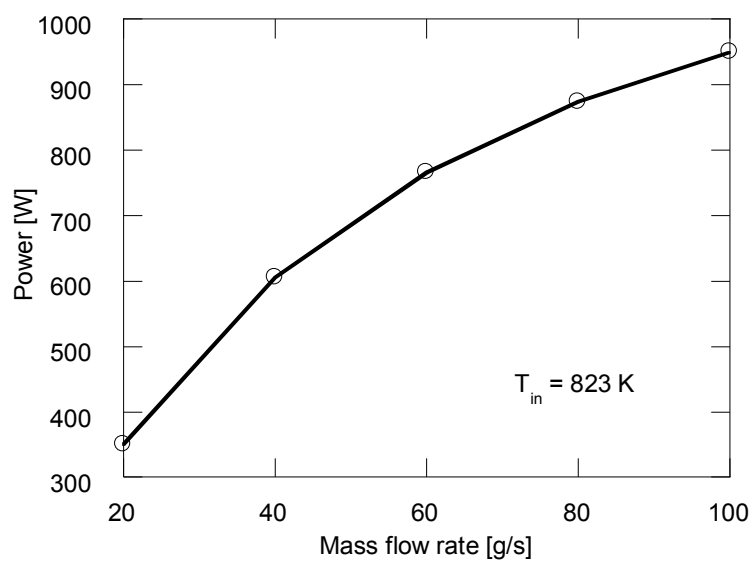


Figure 3.1. Power output vs. flow rate for Baseline Model at $T_{in} = 823 \text{ K}$ (550°C).

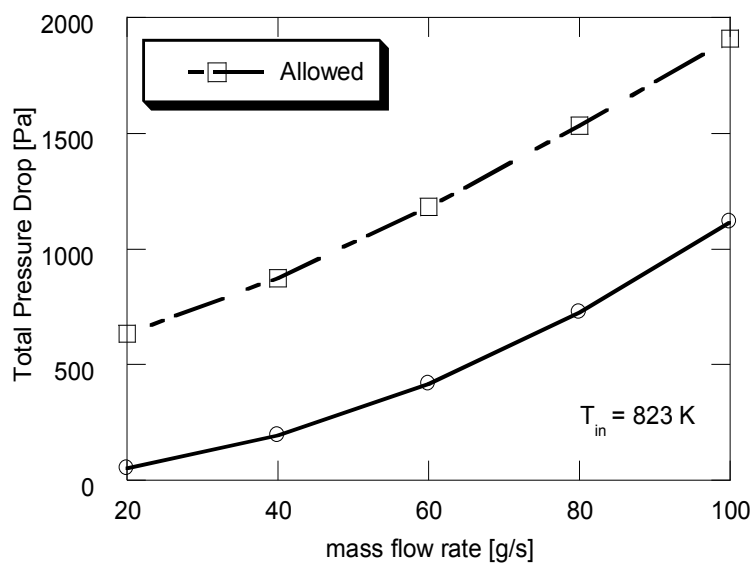


Figure 3.2. Total pressure drop vs. flow rate for Baseline Model at $T_{in} = 823\text{K}$ (550°C).

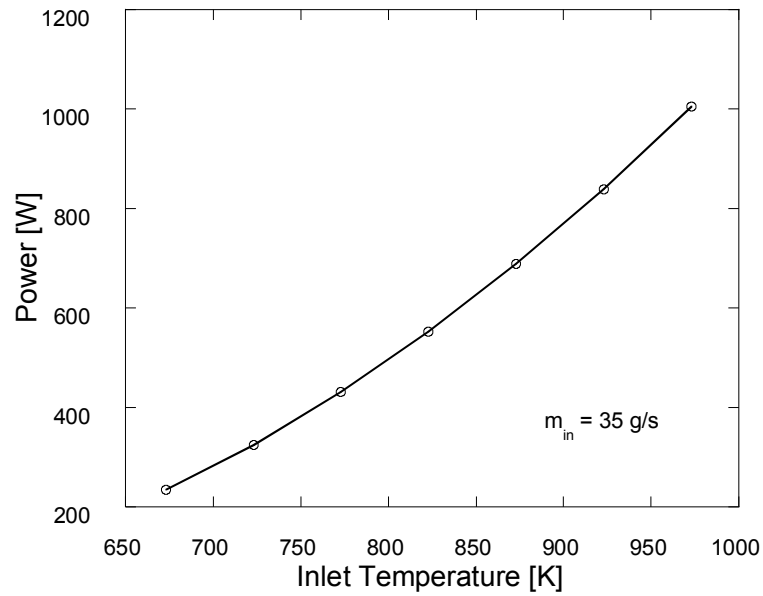


Figure 3.3. Power output vs. Inlet Temperature for Baseline Model at $m_{in} = 35 \text{ g/s}$.

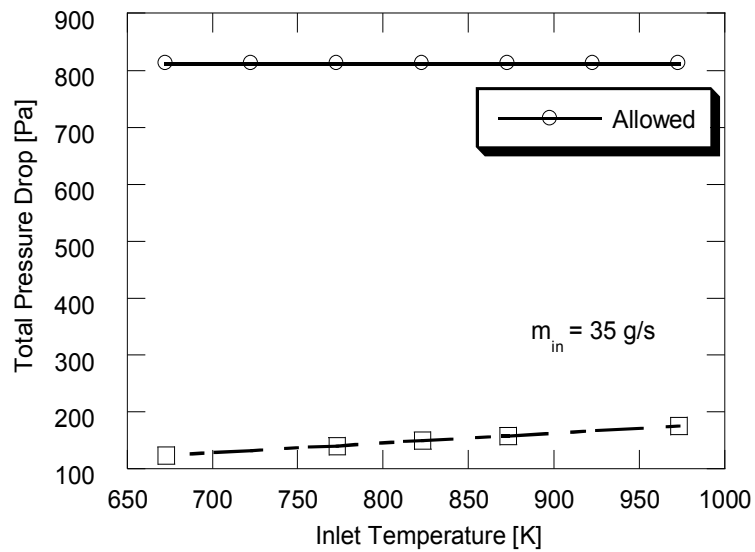


Figure 3.4. Total pressure drop vs. Inlet Temperature for Baseline Model at $m_{in} = 35 \text{ g/s}$. The allowed pressure drop is 812 Pa at given flow rate of 35 g/s.

Figure 3.5 represents the temperature drop across various materials in the thermoelectric generator along the flow direction of the exhaust gas. It is remarkable to note that there is a difference of more than 100 degrees between the gas bulk temperature and the hot side of the thermoelectric module. The temperature drop across the hot side contact by thermal grease is of the order of 30 degrees. However, the current analysis doesn't take into account the fin contact resistances, improper surface contacts due to thermal induced deformations, non-uniformity of thermal grease thickness, etc. Hence, the actual temperature drop is expected to be much higher than stated here. The temperature drop across the junctions decreases from 300 degrees to 120 degrees. For the skutterudites, ZT values decreases with the decrease in temperature (Figure 1.6), the modules near the inlet generate more electrical power than those near the rear end as observed from Figure 3.6. This exhibits that electrical power generation is very much dependent on the actual temperature difference across its junctions.

The energy fluxes were calculated by dividing the energy transfer rate per unit of top surface of the generator. The plot in Figure 3.6 represents the decreasing trend in the energy fluxes along the flow direction. The heat leakages due to radiation and the thermal insulation are very low as compared to conduction losses., hence most of the heat transferred by heat exchanger flows through the thermoelectric modules.

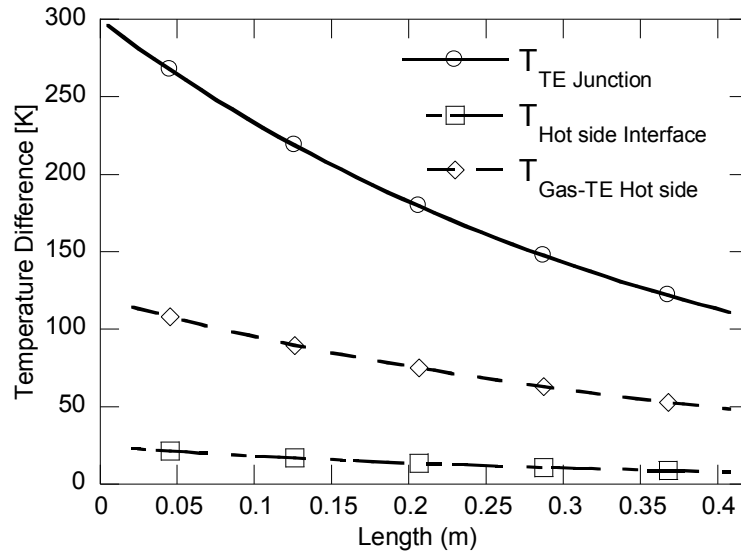


Figure 3.5. Temperature differences across materials along flow direction for Baseline Model at $\dot{m}_{in}=35\text{g/s}$ and $T_{in}=550^\circ\text{C}$.

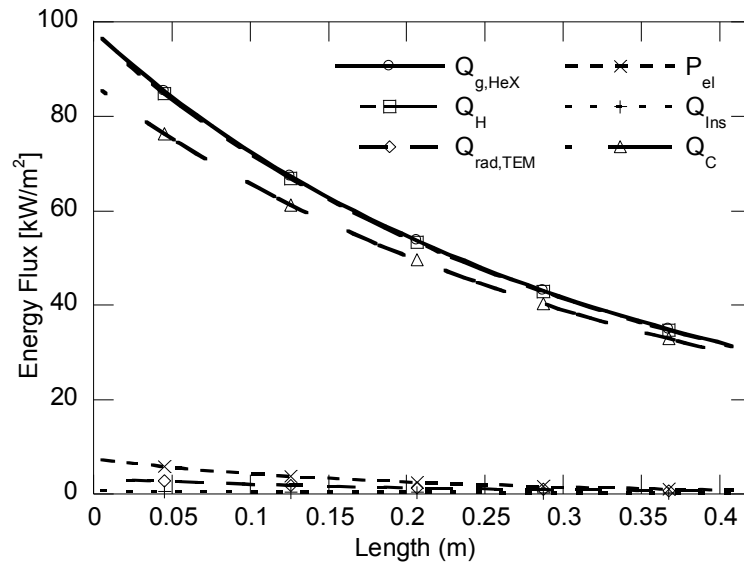


Figure 3.6. Energy flux along flow length for Baseline Model at $\dot{m}_{in}=35\text{g/s}$ and $T_{in}=550^\circ\text{C}$.

The pie chart in Figure 3.7 represents the energy distribution for the baseline model. The output efficiency of the baseline model in terms of electrical power generation is found to be 3.4%. Nearly 36% of incident energy leaves the generator to the environment as exhaust gas. 58% of the incident energy rate is rejected to the engine coolant system. The increased load on the coolant system implies bigger engine radiators to reject more heat to the environment.

Figure 3.8 represents the variation of thermoelectrical parameters along the flow length. The values have been normalized by their maximum values which occurs at $z = 0$. The parameters show a decreasing trend with the flow length. The ZT value of a thermoelectric couple decreases from a maximum of 0.88 to 0.60 at the exit. The maximum current value was found to be quite high as 13.9 A, however the Thomson effect was not considered in this analysis. Additionally, several thermoelectric couples in an actual thermoelectric module are connected in a serial electrical circuit; hence actual drawn current would be lesser. The current also depends on the actual vehicle electrical load. Improper matching of thermoelectric inner resistance to external load resistance can lead to significant loss in power generation. Hence, power conditioning of electrical output is critical.

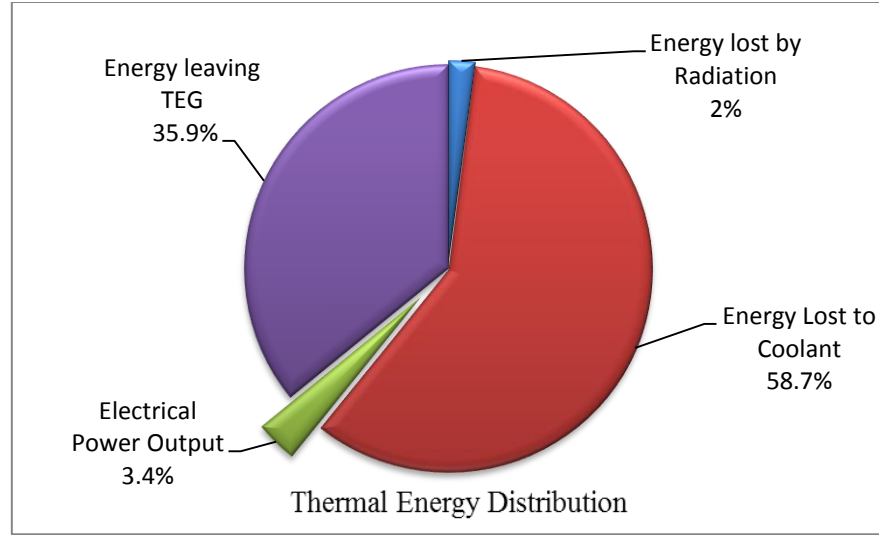


Figure 3.7. Thermal energy distribution for Baseline Model.

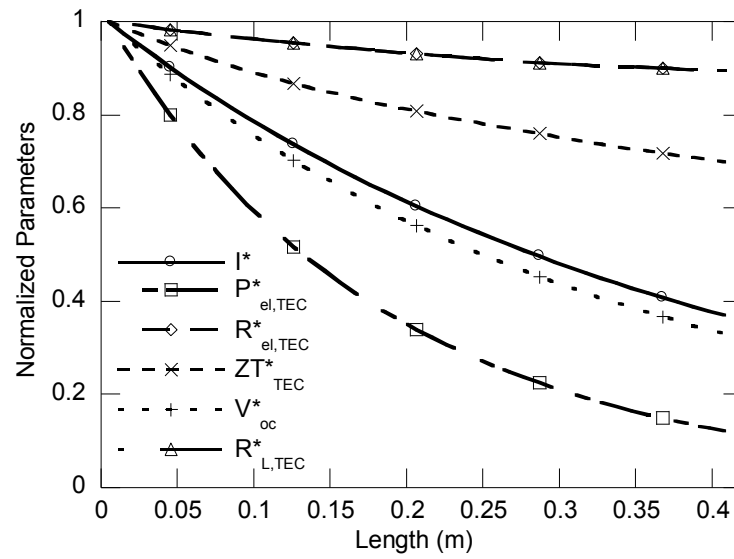


Figure 3.8. Normalized parameters along the TEG length at $\dot{m}_{in}=35\text{g/s}$ and $T_{in}=550^\circ\text{C}$.

Table 3.3. Thermoelectric Couple Parameters.

I_0 (A)	V_0 (V)	P_0 (W)	R_0 (Ω)	Rl_0 (Ω)	ZT_0
13.9	0.107	0.743	3.89E-3	3.89E-3	0.88

3.3.2 Major Conclusions

The analysis of the baseline model leads to major conclusions and provides us several ventures at which the baseline could be improved for this configuration.

- 1) The electrical power generation is a strong function of mass flow rate and inlet exhaust temperatures. The implications of varying inlet conditions could be very severe if proper conditioning of output power is not carried out.
- 2) The thermoelectric modules close to the inlet are exposed to the much higher gas temperatures and hence they generate higher electrical power output.
- 3) ZT value of high temperature skutterudites decrease considerably along the flow direction. Use of modules with higher ZTs at lower temperature near the rear end could be quite beneficial.
- 4) The heat transfer at average inlet conditions was around 60% of the incident energy for the given heat exchanger. By optimizing the fin spacing and thickness, the heat transfer rate can be enhanced considerably.

3.4 Rectangular Topology

The types of topologies discussed in 0 were analyzed for various set of test conditions and parameters for output optimization. This section presents the analysis done for flow configurations with rectangular topology.

3.4.1 Longitudinal Flow Configuration

This section primarily focuses on optimization of longitudinal flow configuration. This parameters variation was mostly motivated from the conclusions derived in Section 3.3.2. The model having dimensions as same as baseline model was selected to observe the impact of varying heat exchanger configuration. The number of fins and fin thickness for a plate fin type heat exchanger were varied and their impact on power output and pressure drop fin spacing was studied.

Figure 3.9 represents the electrical power generation at different fin configurations for average inlet conditions. This plot represents the power output with increasing number of fins of thickness varying from 2 mm to 8 mm. The associated pressure drop is represented in Figure 3.10. It is observed that for a given number of fins, thinner films incur comparatively lesser pressure drops. Both electric power output and pressure drop values increases with the number of fins. Large number of fins will result in high cost and weight of the thermoelectric generator. Configurations with optimized number of fins and thickness can output electrical power of range 600 to 700 W with pressure drops within the allowed backpressure limits.

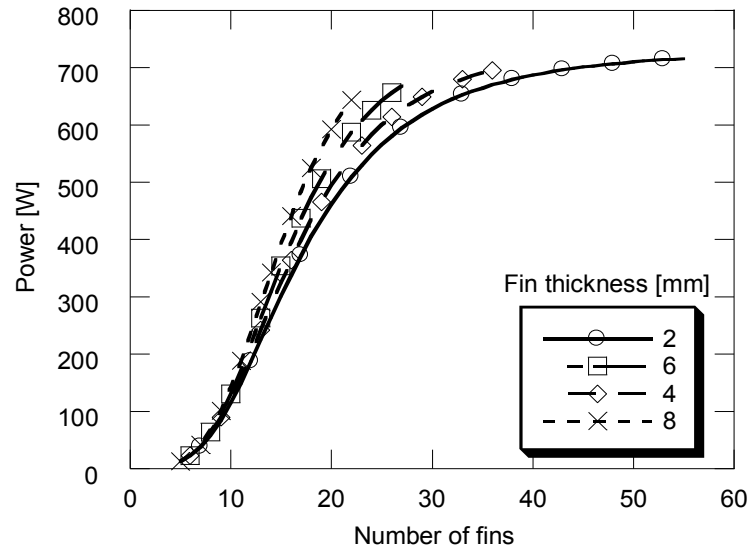


Figure 3.9. Power output vs. different fin configurations at $\dot{m}_{in}=35\text{g/s}$ and $T_{in}=550^{\circ}\text{C}$.

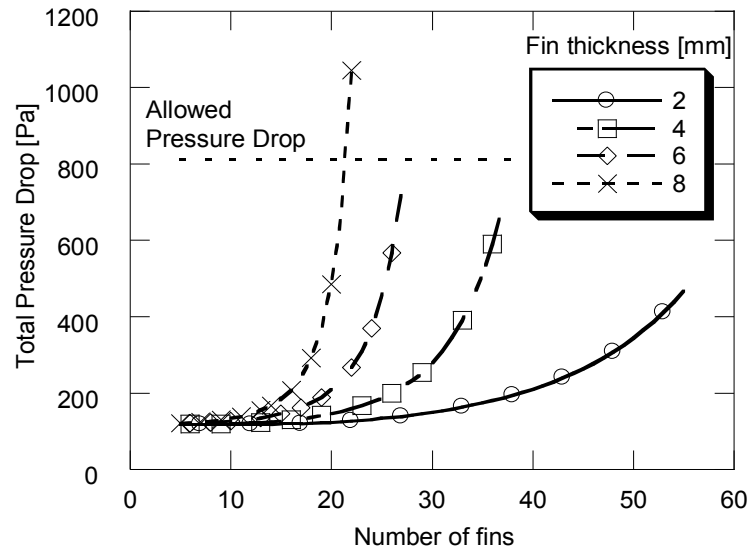


Figure 3.10. Total Pressure drop vs. different fin configurations at $\dot{m}_{in}=35\text{g/s}$ and $T_{in}=550^{\circ}\text{C}$.

As mentioned in previous sub-sections, the hot junction temperature drops considerably along the flow length of the generator. The associated ZT and power generation capacity of the Skutterudite modules also reduced along the flow direction. To overcome these shortcomings, use of thermoelectric modules exhibiting better ZT performance was encouraged. Bismuth Telluride based modules were considered as they perform well at lower hot side temperatures. Figure 3.11 shows the ZT values of thermoelectric couples from Skutterudite and Bismuth Telluride modules. To maximize ZT performance and prevent Bismuth Telluride based modules from damage; the cutoff temperature for transition was set at 550K. The baseline model was analyzed with two different configurations (a) Skutterudites (S) only and (b) hybrid arrangement of Skutterudite and Bismuth Telluride modules (SB).

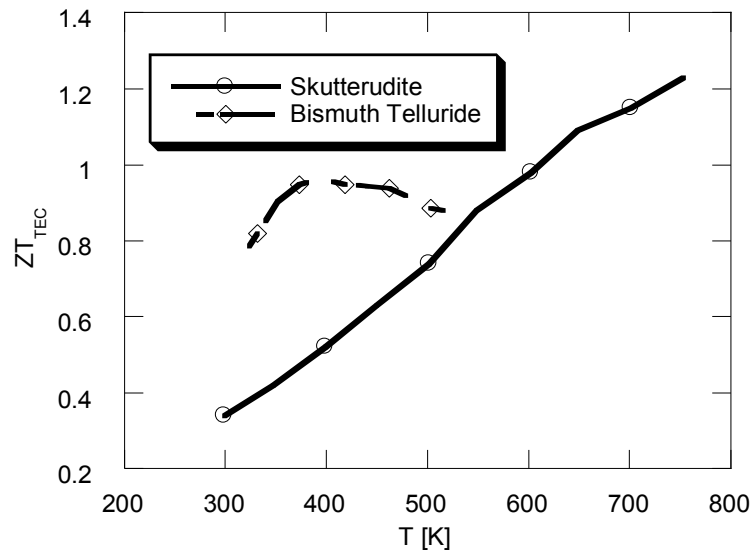


Figure 3.11. ZT values for a thermoelectric couple based on Skutterudite and Bismuth Telluride Modules. Cutoff temperature for transition is set at 550K.

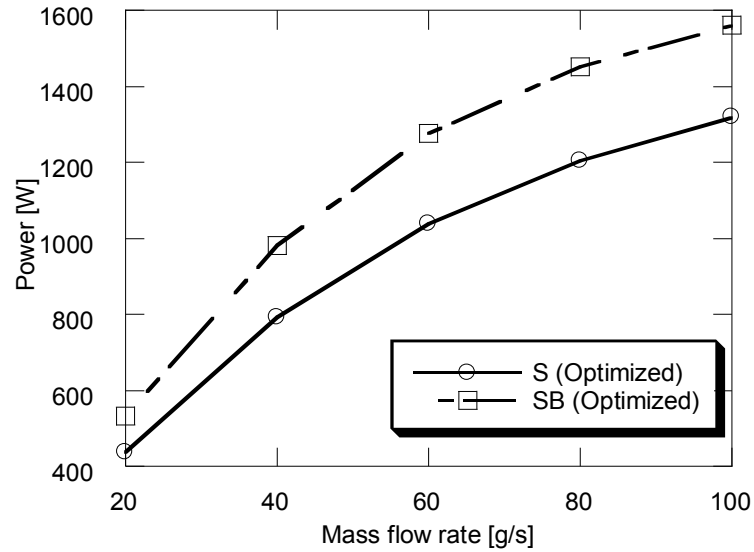


Figure 3.12. Power output vs. different mass flow rates at $T_{in}=550^{\circ}\text{C}$ for 'S' and 'SB' arrangement with optimized heat exchanger configuration. . S-SB and B-SB denote the number of separate Skutterudites and Bismuth Telluride modules required for 'SB' configuration.

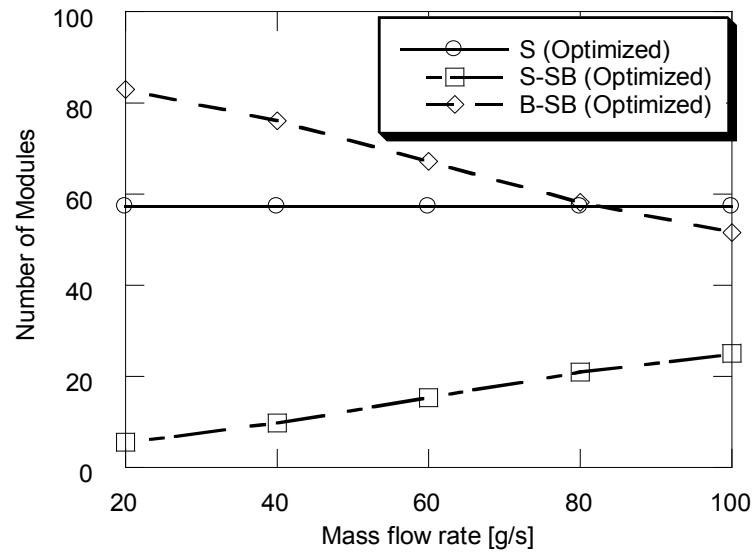


Figure 3.13. Number of TEMs vs. flow rates at $T_{in}=550^{\circ}\text{C}$ for 'S' and 'SB' arrangement with optimized heat exchanger configuration.

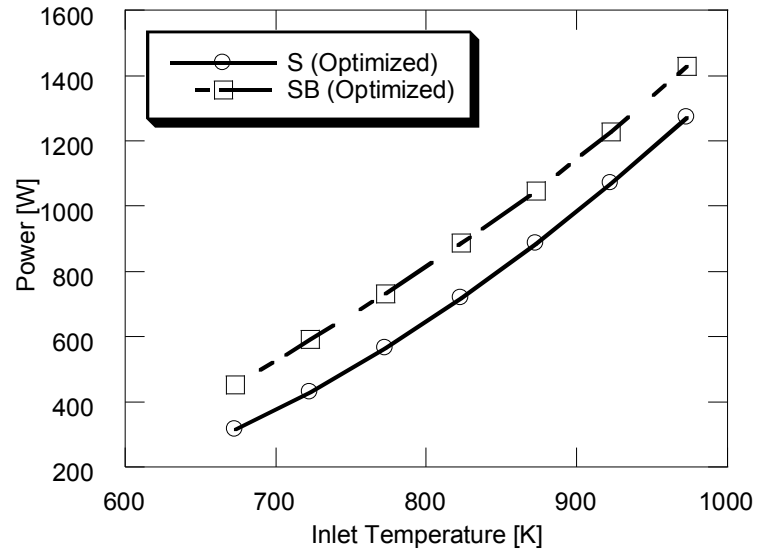


Figure 3.14. Power output vs. Inlet exhaust temperatures at $\dot{m}_{in}=35$ g/s for 'S' and 'SB' arrangement with optimized heat exchanger configuration.

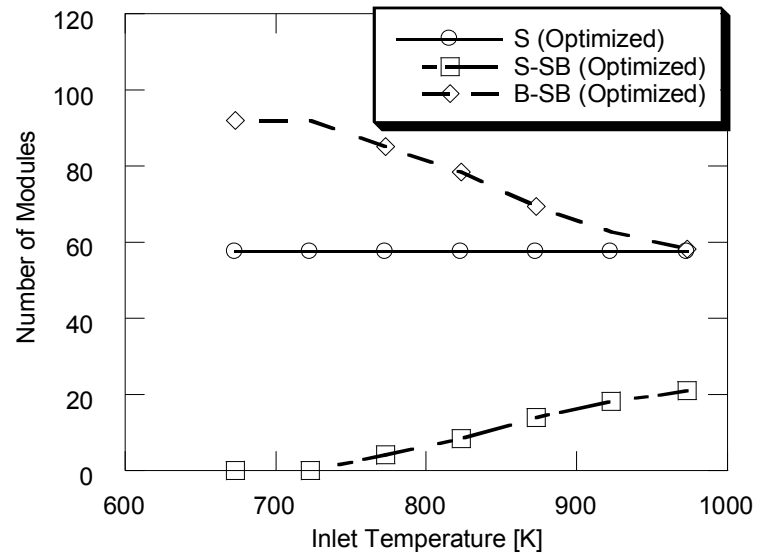


Figure 3.15. Number of TEMs vs. Inlet exhaust temperatures at $\dot{m}_{in}=35$ g/s for 'S' and 'SB' arrangement with optimized heat exchanger configuration.

Figure 3.12 and Figure 3.14 show the benefit of using hybrid arrangement of modules on power output for varying mass flow rate and inlet temperature respectively. This suggests that for a given surface area and inlet conditions, more electrical power can be generated by the use of hybrid configurations than using the skutterudites alone. Since, the inlet conditions decide the location of cutoff temperature along the flow direction, the number of skutterudite and bismuth telluride modules required in a hybrid 'SB' configurations differs with the inlet conditions as shown in Figure 3.13 and Figure 3.15. It is observed that number of skutterudite modules increases with increasing mass flow rate and inlet exhaust temperature whereas it decreases for the bismuth telluride modules. The analysis shows a relatively higher number of bismuth telluride modules since their cross-sectional area is lesser than skutterudite modules. Here cost could be an important factor to decide the relative number of type of modules to be used for actual applications.

The geometry of the model was varied keeping the total volume constant as the baseline model. The length, width and height of the generator was varied within predefined limits (refer to Table 3.1) for inlet mass flow rate of 35 g/s and temperature 550°C. The configurations were fitted with optimized heat exchanger configurations. However, topologies with pressure drop exceeding 812 Pa were disregarded. Figure 3.16 represents a 3D plot of electrical power output for skutterudite only arrangements. It is observed that wider and flatter (minimum height) generators generate the maximum possible electrical powers.

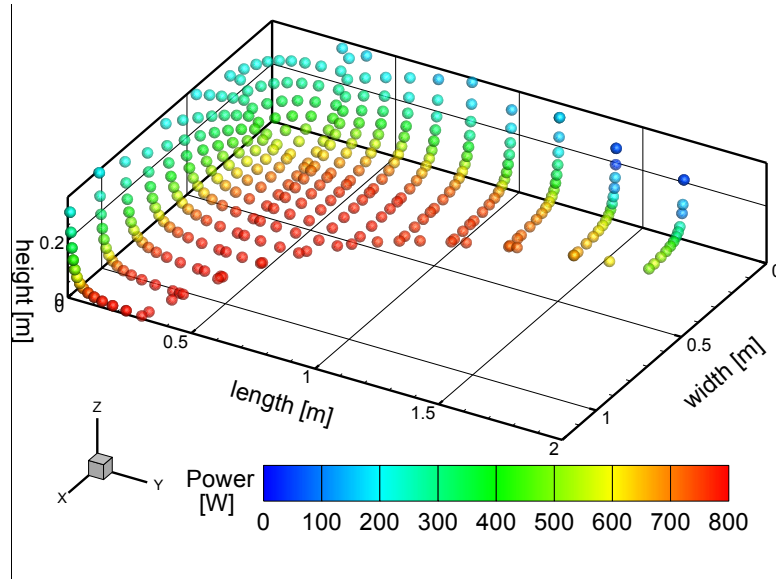


Figure 3.16. 3D plot of Power output at optimized fin configurations at $\dot{m}_{in}=35$ g/s and $T_{in} = 550^{\circ}\text{C}$.

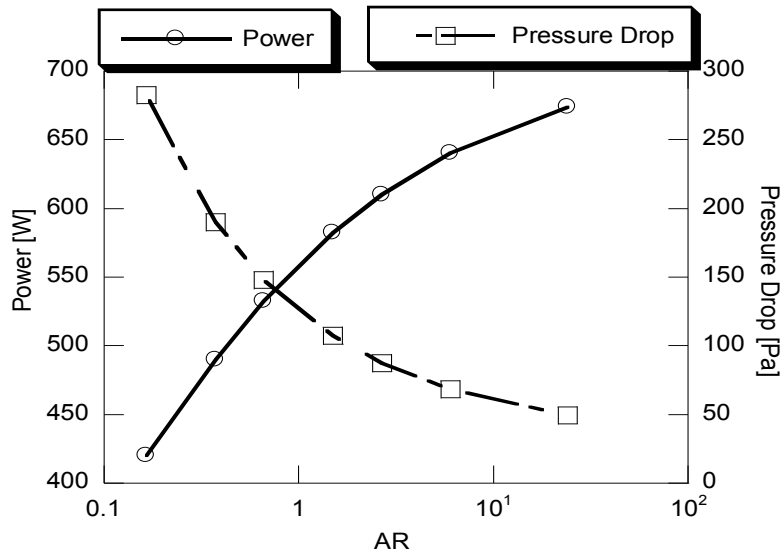


Figure 3.17. Power output and pressure drop variation at different aspect ratio ($AR = \text{width/length}$) at fixed generator height of 38 mm using 50 skutterudites (Inlet: $\dot{m}_{in}=35$ g/s, $T_{in} = 550^{\circ}\text{C}$ for with $t_{fin} = 3.3$ mm and $s_{fin} = 6.35$ mm).

Another analysis was performed by keeping the height same as 38 mm and changing the aspect ratio ($=\text{width}/\text{length}$) to accommodate 50 skutterudite modules on top and bottom surfaces of the generator. Figure 3.17 shows that power output is higher at high aspect ratios or wider generators and associated pressure drops are lesser due to shorter lengths.

3.4.2 Major Conclusions

The analysis of the longitudinal flow configurations model leads to following findings:.

- 1) The heat exchanger configurations play a major role in electrical output and the pressure drops. Optimized number of fins and thickness (or spacing) can help generators produce electrical output of desired range of 600-700 W while keeping the backpressure gain well below 812 Pa for average inlet conditions.
- 2) Use of hybrid arrangements of thermoelectric modules is an advantage for augmented electrical power generation for a given inlet condition.
- 3) Wide and flat (with minimum practical height) thermoelectric devices generate the maximum possible electrical power of the order of 800W.
- 4) Wider and shorter (in length) generators exhibit much higher electrical power output and quite lesser associated pressure drops for a given number of thermoelectric modules.

3.4.3 Transverse Configuration

This section presents analysis on transverse configuration in a rectangular topology. As mentioned in previous section, the hot exhaust flows through the channels inside the domain and thermoelectric modules are located inside the box as longitudinal racks. The plate fin heat exchangers are integrated within the hot channels. The number of racks inside box volume controls the total number of thermoelectric modules for a given rectangular shapes.

Figure 3.18 represents the effect of change in channel width on the power output, number of modules and pressure drop (in Figure 3.19) for a rectangular domain with fixed heat exchanger configuration. The channel width controls the total number of thermoelectric racks inside the TEG volume, hence the number of modules decreases as the channel width increases as shown in right axis. Similarly, the power generation rate too decreases with channel width. The curve has a staircase pattern and it shows a drop once a thermoelectric module rack is eliminated. There is sudden drop in power generation for very small channel width because the effective heat exchanger area decreases and hence heat transfer to the modules is inadequate. Figure 3.19 represents the pressure drop with varying channel width. Pressure drop is found to be very high at lower channel widths having smaller cross-sections. However, for this case the observed pressure drops are much higher than the allowed limits.

Fixed TEG Geometry

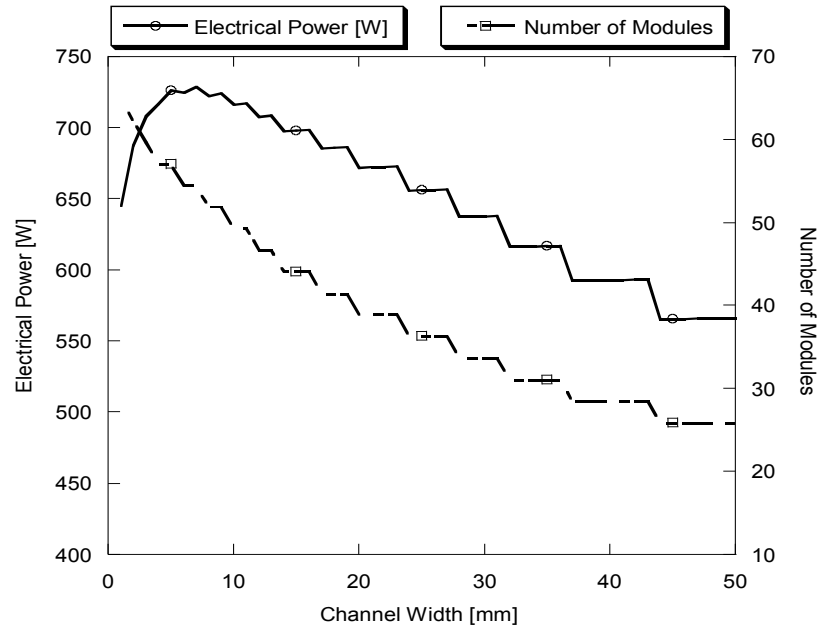


Figure 3.18. Left Y axis represents electrical power output with varying channel width (1 mm - 50 mm) with $N_{fin} = 9$ per channel ($t_{fin} = 2\text{ mm}$, $s_{fin} = 2.2\text{ mm}$) with baseline geometry (height: 3.8 cm, width: 22.4 cm and length: 41.3 cm) at $\dot{m}_{in} = 35\text{ g/s}$ and $T_{in} = 550^\circ\text{C}$. Right Y axis displays number of skutterudite modules.

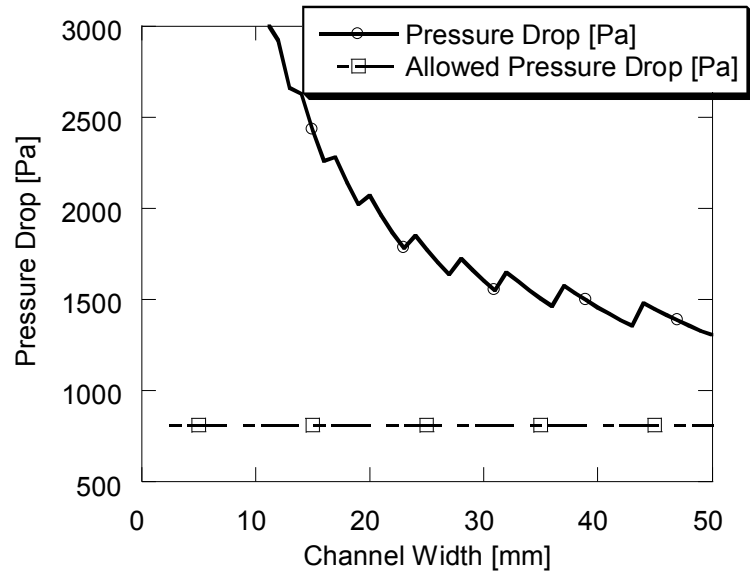


Figure 3.19. Y axis represents total pressure drop with varying channel width for same inputs mentioned in Figure 3.18.

Several configurations were tested by modifying the aspect ratios of the transverse configurations. The TEG length was fixed as multiples of module side i.e. only one module is placed along the length of the TEG. This was done to insure that thermoelectric modules face the highest temperature at gas side. The aspect ratio (width/height) was varied and its impact was studied. The geometries with optimized heat exchanger configuration and optimized number of skutterudite modules; and pressure drop within the predefined limit were considered for results analysis.

Figure 3.20 shows the power output rate for varying aspect ratios for three different flow rates. It is found that the power generation doesn't vary much with the geometry changes. It can be accounted by the fact that all the thermoelectric modules face the same hot gas bulk temperature (since the TEG length is one module height). However, there is a quite difference in the power generation rates as the mass flow rates increases which has been demonstrated by the longitudinal configuration. The bottom graph displays the number of TEMs required to achieve the generation rate at various aspect ratios. It is found that 50-60 skutterudite modules fall in the optimum range independent of inlet mass flow rate. The pressure drop for these cases were found to be well below ($< 60\%$) the allowed backpressure limit. This could be explained with the fact that TEG length is of only one module width, hence pressure drops due to viscous drag on fins will not be quite high.

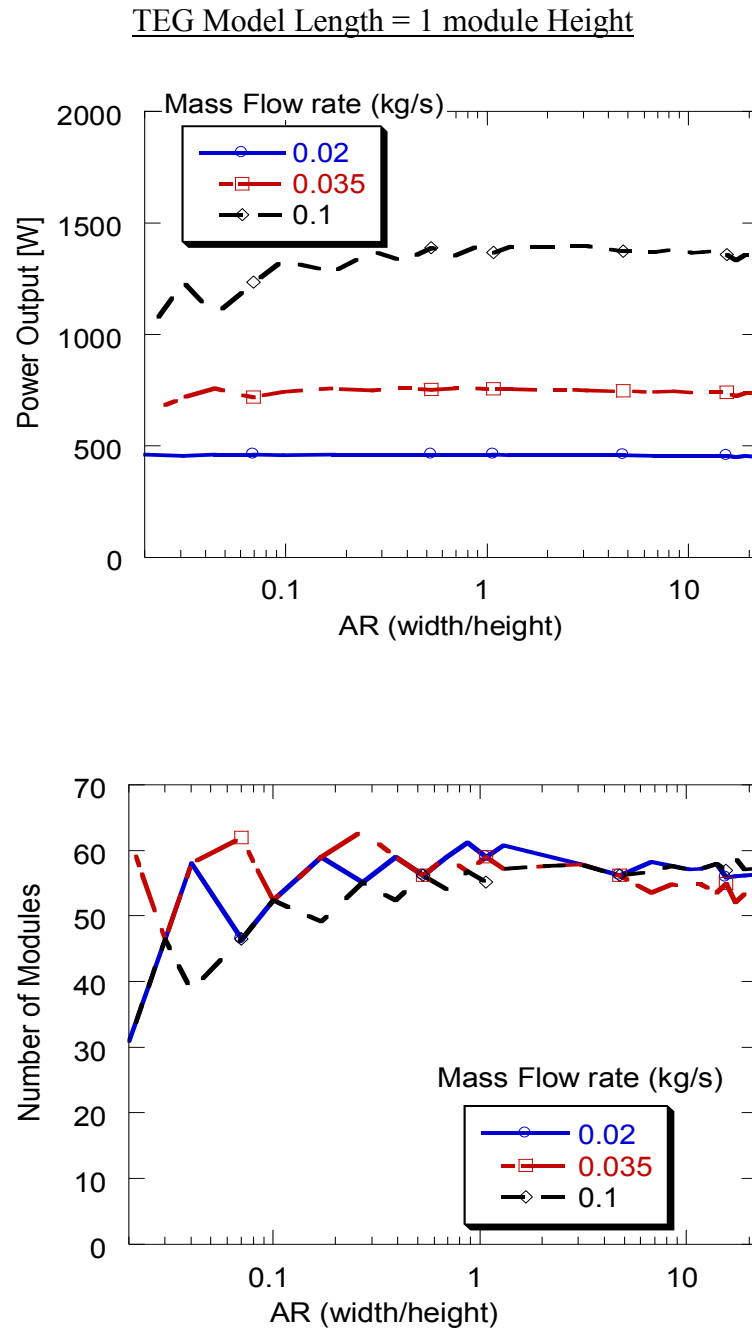


Figure 3.20. The top figure shows the optimized power output with respect to varying AR (aspect ratio = width/height) keeping the length equal to 1 module side at $T_{in} = 550^{\circ}\text{C}$. The legend shows electrical output at different mass flow rates. The bottom figure represents number of skutterudite modules required for each configuration.

Adding to previous behavior, the effect of the number of skutterudite modules was also studied by varying the aspect ratios. The number of modules was limited to 20, 40 and 60 and their impact was noted on the power output. It is found that aspect ratio doesn't have any significant impact on the power generation rate. This is important to note that there is not much gain in power output if the number of modules is switched from 40 to 60 which is not the case from 20 to 40 modules. Hence, to obtain a power output range around 700W, 40 skutterudite modules will be sufficient. Adding more number of modules may lead to slight increase in electrical power output but will result in additional cost of TEG.

The bottom plot represents the total pressure drop incurred for different aspect ratio at different number of modules. To accommodate higher number of thermoelectric modules inside the rectangular domain at a given aspect ratio (TEG width), the channel width has to be reduced. This increases the fin channel Reynolds number and hence higher pressure drops. Again this supports the fact, that use of 40 modules in this case would be quite beneficial than going for much higher number of thermoelectric modules.

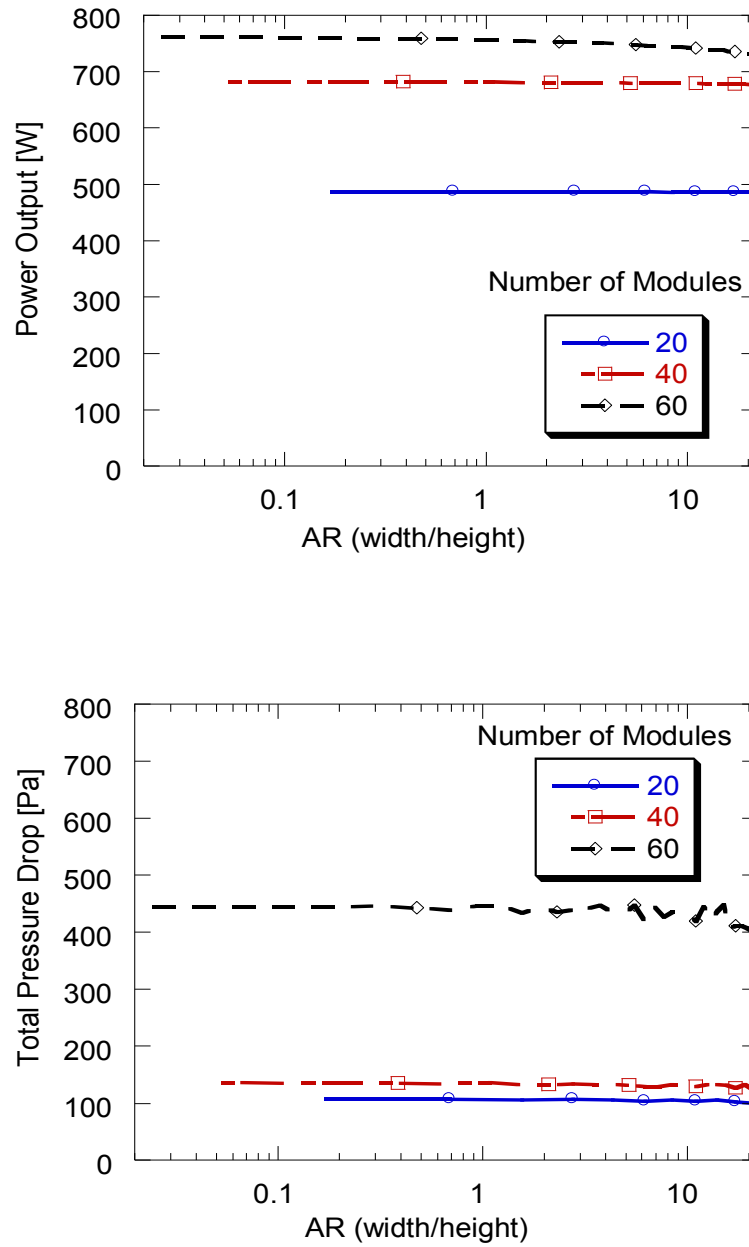


Figure 3.21. The top figure shows the optimized power output with respect to varying AR (Aspect ratio = width/height) keeping the length equal to 1 module side for $\dot{m}_{in} = 35$ g/s and $T_{in} = 550^\circ\text{C}$. The colored curves show electrical output at different number of skutterudites modules as shown in legend. The bottom figure shows the pressure drop occurred for the same case.

3.4.4 Major Conclusions

- 1) The analysis of the configurations with TEG length = one module show that 50-60 skutterudite modules will be sufficient to generate power of the order of 700W at average inlet conditions.
- 2) The electrical power generated is a strong function of the inlet mass flow rate. However the optimized numbers of modules are independent of inlet conditions and the aspect ratio.
- 3) The analysis with limited number of modules exhibit power output of the order of 700W at average inlet conditions with 40 skutterudite modules.
- 4) Marginal gain in electrical power is observed when number of modules is increased from 40 to 60.
- 5) The power output is independent of the varying aspect ratio since the thermoelectric modules are subjected to same gas bulk temperature within TEG length for cases having fixed or unlimited number of modules.
- 6) The associated pressure drops are found to be quite low since the TEG length is restricted to one module side.

3.5 Circular Topology

This section discusses the topologies having a circular symmetry. The central bypass pipe is a common feature for these topologies. This protects the thermoelectric devices from over-heating of thermoelectric modules, high backpressure in engine, etc. The results from hexagonal and cylindrical configurations are discussed in following sub-sections.

3.5.1 Hexagonal Topology

The cross-section of the hexagonal topology is bounded by inner and outer diameters. The effect of variation in these two diameters was studied on power output and pressure drop while keeping the whole volume constant. Figure 3.22 represents the power output generated for average inlet conditions for optimized heat exchanger configurations. The inner diameter was varied within 0.01 m to 0.04 m and outer diameter from 0.06 m to 0.2 m. It is observed that power output reaches a maximum of 658W at outer diameter of 0.105 m. The number of modules is found to be 42 at this maximum. The power output is nearly independent of inner diameter for higher values of diameter. However, the power output decreases considerably at higher values of inner diameter. This can be explained by the fact that the effective surface area of heat exchangers in the annular region decreases. The effective number of skutterudite modules decreases with increasing outer diameter or decreasing generator's length due to fixed volume constraint. Figure 3.23 represents the associated pressure drops which decreases with increasing outer diameter or decreasing device length. The configurations with higher inner diameter leads to smaller cross-sections for exhaust gas flow and hence relatively higher pressure drops.

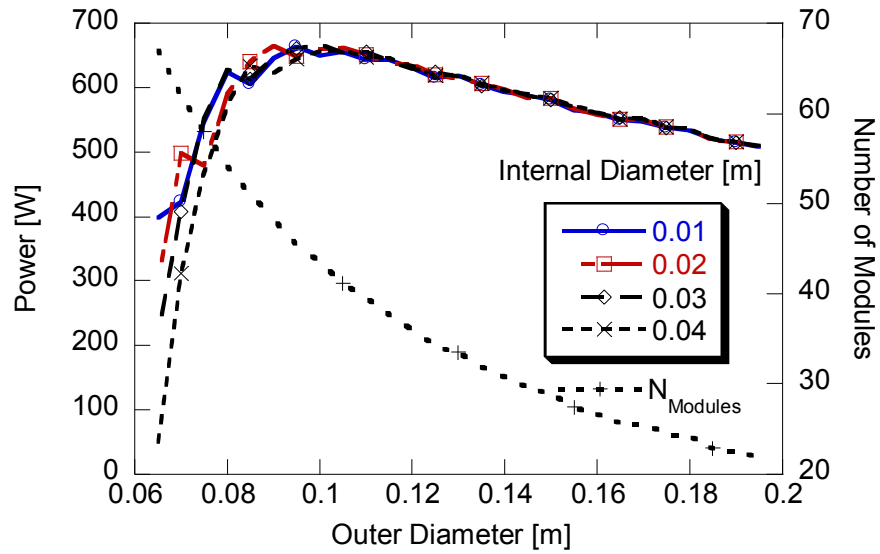


Figure 3.22. Power output with varying outer diameter for different inner diameters for ‘S’ configuration at $\dot{m}_{in} = 35$ g/s and $T_{in} = 550^\circ\text{C}$ for optimized heat exchanger configuration. Right Y-axis shows number of Modules.

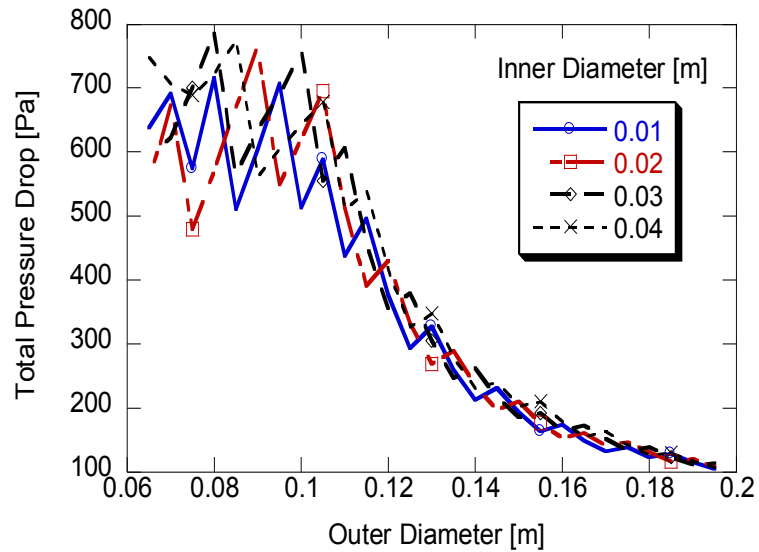


Figure 3.23. Total Pressure drop with varying outer diameter for different inner diameters for ‘S’ configuration at $\dot{m}_{in} = 35$ g/s and $T_{in} = 550^\circ\text{C}$ for optimized heat exchanger configuration.

The hexagonal topology was also studied for hybrid ‘SB’ and standalone ‘S’ arrangements of thermoelectric modules. These arrangements were compared for varying inlet conditions like mass flow rate (Figure 3.24) and inlet exhaust temperatures (Figure 3.26). The plots suggest increase in electrical power generation with increasing mass flow rate or inlet temperature. As evident from previous topological studies, it is observed that the hybrid arrangements of TEMs exhibit much higher electrical power output as compared to skutterudites only arrangement. Similarly, the number of skutterudites increases with increasing exhaust gas mass flow rate or inlet temperature as shown in Figure 3.25 and Figure 3.27.

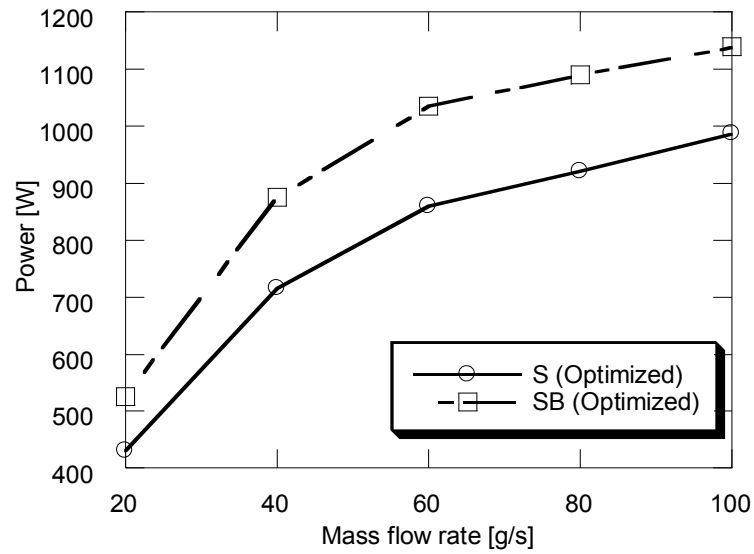


Figure 3.24. Power output with varying mass flow rates for outer diameter = 0.105m and inner diameter = 0.04 m for 'S' and 'SB' configuration at $T_{in} = 550^{\circ}\text{C}$.

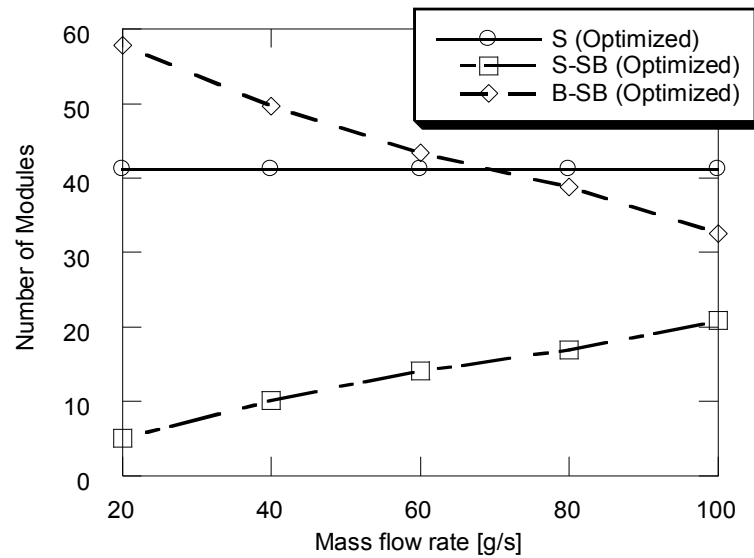


Figure 3.25. Number of Modules vs. mass flow rates for outer diameter = 0.105 m and inner diameter = 0.04 m for 'S' and 'SB' configuration at $T_{in} = 550^{\circ}\text{C}$.

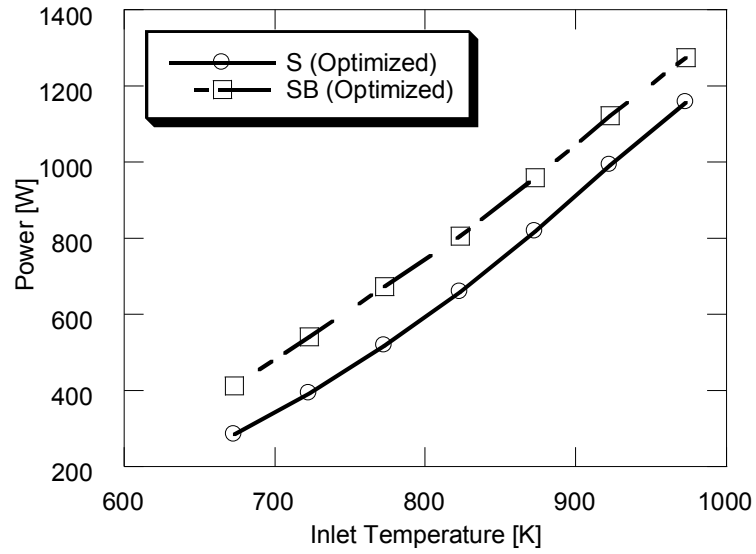


Figure 3.26. Power output with varying inlet temperatures for outer diameter = 0.105 m and inner diameter = 0.04 m for 'S' and 'SB' configuration at $\dot{m}_{in} = 35$ g/s.

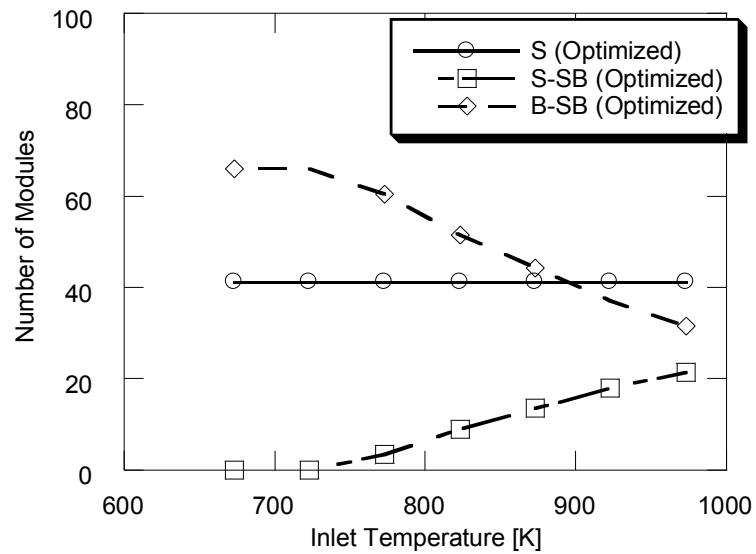


Figure 3.27. Number of Modules vs. varying inlet temperatures for outer diameter = 0.065 m and inner diameter = 0.04 m for 'S' and 'SB' configuration at $\dot{m}_{in} = 35$ g/s.

3.5.2 Major Conclusions

The major findings from current analysis were:

- 1) The hexagonal configuration has a provision of bypass system which is integrated inside the thermoelectric generator design.
- 2) Hexagonal configuration with shorter flow lengths exhibit higher electrical power and quite lesser pressure drops.
- 3) The electrical power reaches a maximum of 658 W at outer diameter of 0.105m for the given volume.
- 4) The generated power is independent of inner diameter size. However, the power output decreases considerably if inner diameter is comparable to outer diameter ($> 50\%$).
- 5) Hybrid arrangements guarantee much higher electrical power for a given heat exchanger configuration and inlet conditions.

3.5.4 Cylindrical Topology

This sub-section presents the results from the cylindrical topology. This model is similar to the hexagonal model except the thermoelectric modules are mounted on the curved outer surface. However, it might be difficult to achieve a very good thermal contact on curved surfaces for thermoelectric modules for practical applications

The inner and outer diameters of the cylindrical pipes were varied to assess the impact on generated electrical power and associated pressure drops with optimized heat exchangers. Figure 3.28 shows that electrical power output reaches to a maximum of 720 W at outer diameter of 0.08 m. The power generation rate decreases with increasing outer diameter since the number of thermoelectric modules that can be mounted on the outer curved surface decreases. The electrical power is almost independent of inner diameter values but it decreases considerably when inner diameter is comparable to outer diameter ($> 50\%$). As the inner diameter becomes comparable to the outer diameter, the effective surface area of heat exchanger in annular region decreases. The associated pressure drop curves in Figure 3.30 show a similar trend. After outer diameter of 0.1 m, the pressure drop decreases with the increase in outer diameter of the inner diameter. The selection of optimized heat exchangers for the outer diameter range 0.06 m to 0.1 m, limits the pressure drop below 812 Pa.

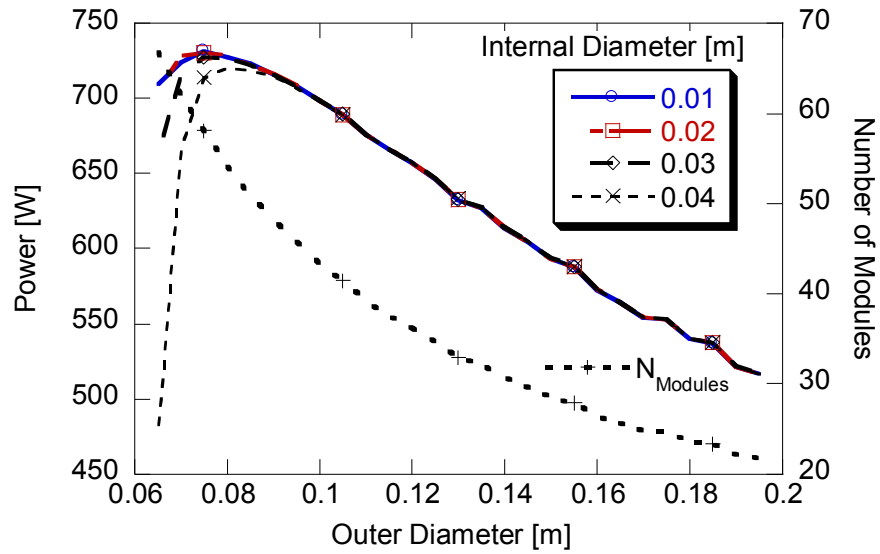


Figure 3.28. Power output with varying outer diameter shown for different inner diameters for ‘S’ configuration ($\dot{m}_{in} = 35$ g/s and $T_{in} = 550^\circ\text{C}$). Right axis shows the required number of Skutterudite Modules.

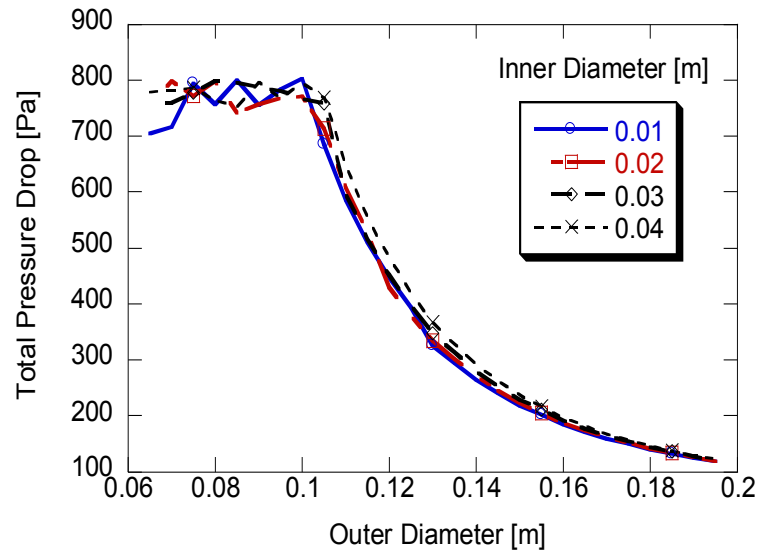


Figure 3.29. Total Pressure drop with varying outer diameter for different inner diameters for ‘S’ configuration ($\dot{m}_{in} = 35$ g/s and $T_{in} = 550^\circ\text{C}$).

The effect of varying inlet conditions was also studied on the output parameters as discussed in previous sub-sections. The inlet parameters like mass flow rate and the inlet temperature was varied within predefined limits and their impact on electrical power generation and pressure drop was studied. It is observed that electrical power generation rate increases with the increase in mass flow rate for ‘S’ configuration in Figure 3.30. The hybrid configurations of skutterudite and bismuth telluride generate much higher power than the skutterudite alone. All these results are calculated from the configurations with optimized heat exchangers.

Similar observation is found when the inlet temperature varies within the range of 400 °C to 700 °C as shown in Figure 3.32. The output power increases with the increasing inlet temperature. The hybrid arrangement ‘SB’ exhibits higher electrical power generation at a given inlet condition when compared to ‘S’ skutterudite only configuration. Figure 3.33 represents the required number of thermoelectric modules for ‘S’ and ‘SB’ configuration at varying inlet gas temperature. The number of the skutterudites in a hybrid ‘SB’ configuration increases with increasing inlet temperature since the cutoff point shift towards the exit of the device

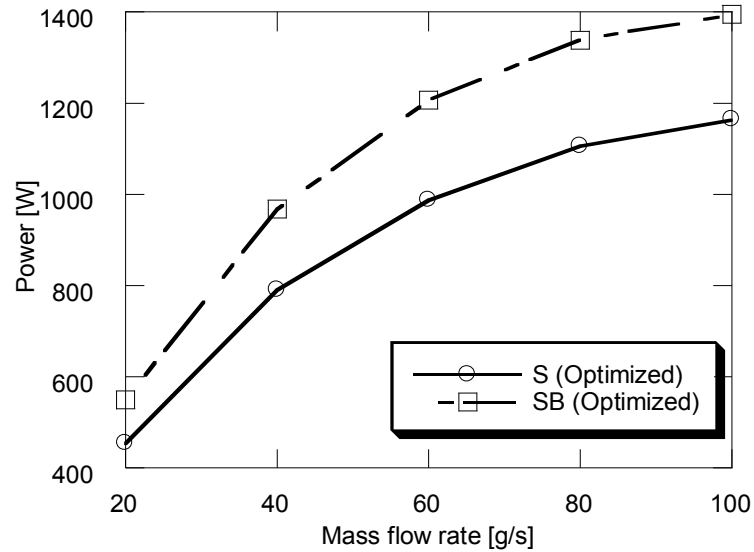


Figure 3.30. Power output with varying mass flow rates for outer diameter = 0.08 m and inner diameter = 0.04 m for 'S' and 'SB' configuration at $T_{in} = 550^{\circ}\text{C}$ for optimized heat exchanger configuration.

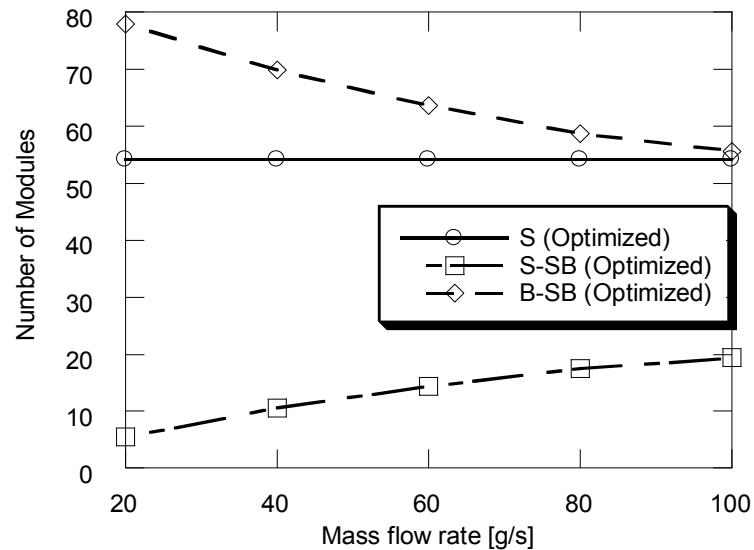


Figure 3.31. Required number of Modules with varying mass flow rates for outer diameter = 0.08 m and inner diameter = 0.04 m for 'S' and 'SB' configuration at $T_{in} = 550^{\circ}\text{C}$ for optimized heat exchanger configuration.

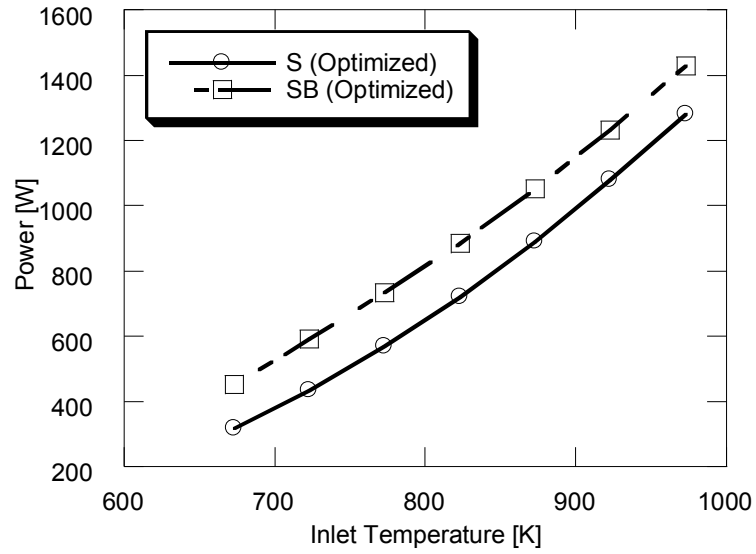


Figure 3.32. Power output with varying inlet temperatures for outer diameter = 0.08 m and inner diameter = 0.04 m for 'S' and 'SB' configuration at $\dot{m}_{in} = 35$ g/s.

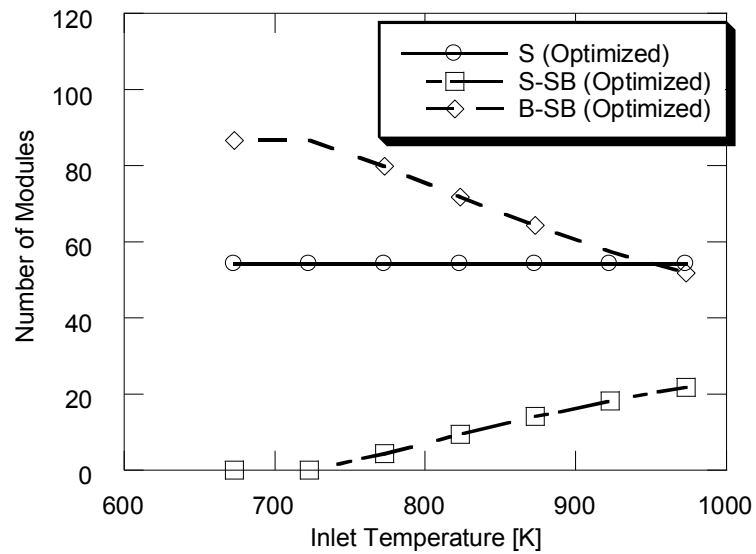


Figure 3.33. Required number of modules with varying inlet temperatures for outer diameter = 0.08 m and inner diameter = 0.04 m for 'S' and 'SB' configuration at $\dot{m}_{in} = 35$ g/s.

3.5.5 Major Conclusions

The conclusions are similar to ones derived for the hexagonal flow configuration as follows:

- 1) The cylindrical configuration has a provision of bypass system which is integrated inside the thermoelectric generator.
- 2) Cylindrical configuration with shorter flow lengths exhibit higher electrical power and quite lesser pressure drops.
- 3) The electrical power reaches a maximum of 720 W at outer diameter of 0.08 m and inner diameter of 0.04 m for the given volume which is quite higher than the hexagonal flow configuration.
- 4) The generated power is independent of inner diameter size. However, the power output decreases considerably if inner diameter is comparable to outer diameter ($> 50\%$).
- 5) Hybrid arrangements guarantee much higher electrical power for a given heat exchanger configuration and inlet conditions.

3.5.7 Model Comparison

The four models were compared in respect to electric power generation with the number of Skutterudite Modules at $\dot{m}_{in} = 35$ g/s and $T_{in} = 550^\circ\text{C}$.

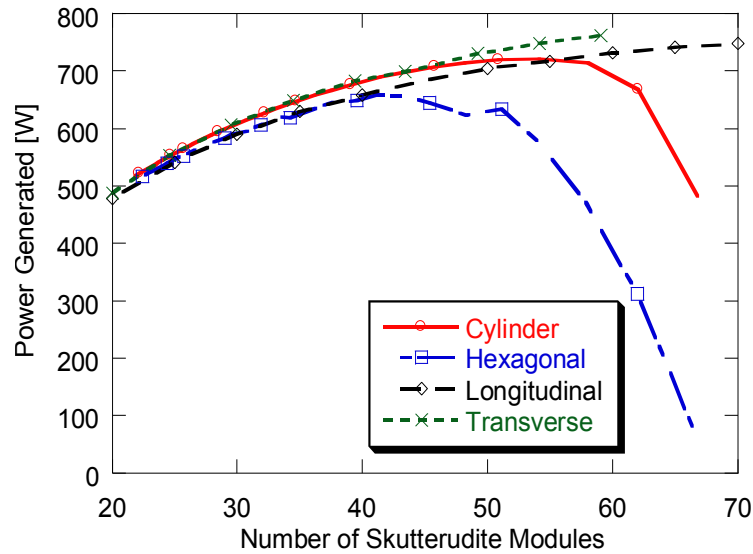


Figure 3.34. Power dependence of various designs on number of TEMs.

The models were of optimized geometry and with optimized heat exchanger configuration. It is evident from the Figure 3.34 that all the four models show a linear increase in electric power generation upto 40 Skutterudite modules. Transverse flow configurations fail to deliver after 60 modules since it becomes difficult to accommodate higher number of modules in the given volume. Topologies having circular flow configuration cannot accommodate higher number of modules as their length decreases. However these models with longer TEG's lead to considerable pressure drops which make them inefficient.

CHAPTER 4. OPTIMIZATION OF SKUTTERUDITE BASED THERMOELECTRIC MODULES

4.1 Introduction

System modeling of thermoelectric (TE) components requires solution of coupled thermal and electric fluxes through the n- and p-type semiconductor legs given the appropriate thermal boundary conditions at junctions. Such applications have large thermal gradients along the semiconductor legs where materials properties are strong functions of spatial varying temperature fields. In this present work, one-dimensional heat flux and temperature variations across thermoelectric legs have been solved using iterative numerical approach as a tool to optimize both TE module and TEG designs. Design trades are explored assuming the use of skutterudite as thermoelectric material that has potential for application to automotive applications where exhaust gas and heat exchanger temperatures typically vary from 100°C to 600°C. Dependencies of parameters such as leg geometry, fill fractions, electric current, thermal boundary conditions, etc., on leg efficiency, thermal fluxes and electric power generation have been studied in detail. Optimal leg geometries are computed for various automotive exhaust conditions.

4.2 Literature Survey

A number of analytical and numerical models [37,38,50,54] have been employed to assess the thermoelectrical generator system with varying levels of sophistication. Espinosa et al[14] employed $\text{Mg}_2\text{Si}/\text{Zn}_4\text{Sb}_3$ for high temperatures followed by Bi_2Te_3 for low temperatures.

This does account for the temperature dependent properties along the heat exchanger but not within the legs. Kumar [55–57] presented a thermal resistance network based model to analyze a thermoelectric generator system for a General Motors Co. prototype generator designed for Chevrolet Suburban. Junction averaged thermoelectric properties were used to calculate the Seebeck voltage potential and electrical power.

The optimization of these generators requires holistic approach to address each and every component of a generator system. The averaging techniques fail to deliver accurate results at the thermoelectric module level at higher electric current density conditions [48]. In addition, these techniques cannot be applied precisely for optimization of thermoelectric leg geometries as shown in APPENDIX. In these methods, the Thomson coefficient is taken as zero. Also, the material property variations along the thermoelectric leg height are not accounted. The high cost of rare-earth elements used in candidate TEM legs also enters as a prime variable in system trade-off studies.

To address these issues, the present work focuses on modeling the thermoelectric components of a TEG system subjected to conditions characteristic of automobile exhaust. A numerical model is implemented to study the interdependence of electrical power generation on leg height, junction conditions, and area ratio of n-type to p-type material [58]. The method captures the temperature dependent properties along a thermoelectric leg. Mesh independence is verified and the tool is used to analyze sample cases comparable to automobiles exhaust. The thermoelectric material for this study is limited to multiple filled Skutterudites [8,9]. These materials have desirable zT values at high temperature making them suitable for applications related to diesel and gasoline engines. The following section provides a description of the implemented model, followed by the results and conclusions from the study.

4.3 Numerical Modeling

The thermal and electrical fluxes through the thermoelectric legs of a TE couple (one n-type and one p-type leg) are studied using the numerical model by Shih [58]. A TE module will be comprised of many of such TE couples connected in series electrically and thermally in parallel. The n- and p-type legs have been discretized lengthwise into segments as shown in Figure 4.1. Segment '0' is in contact with cold junction and N^{th} segment is in contact with hot side junction. Here T_H and T_C are hot side and cold side junction temperatures. I is the electric current through the thermoelectric legs whereas R_O is the load electrical resistance.

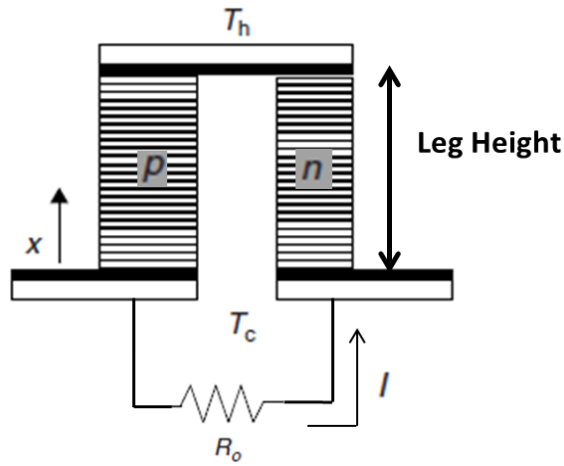


Figure 4.1. Schematic of a thermoelectric couple with discretization along leg height

Assuming 1-D conduction along the thermoelectric leg, the steady state energy balance of a thermoelectric element is reduced to Domenicali's equation [59] as shown below.

$$\frac{\partial}{\partial x} \left(\kappa(x) \frac{\partial T(x)}{\partial x} \right) = -\rho(x) J^2 + JT(x) \frac{\partial S(x)}{\partial x} \quad (4.1)$$

$$q(x) = JT(x)S(x) - \kappa(x) \frac{\partial T(x)}{\partial x} \quad (4.2)$$

where $\kappa(x)$ is the thermal conductivity, $\rho(x)$ is the electrical resistivity, and $S(x)$ is the Seebeck coefficient of the thermoelectric materials as they vary along the leg height dimension ' x '. $T(x)$, $q(x)$ and J are the temperature, heat flux, and current density flux, respectively. In Eq. (4.1), the left hand term is the Fourier conduction in one dimension, the first term in right hand side is the joule heating and last term includes both Peltier (∇S at junction) and Thomson (∇S in thermal gradient) effects. In Eq. (4.2), the first term on right hand side is the entropy transport term and second term being the thermal conduction.[59]. Eq. (4.2) can be substituted in Eq. (4.1) to derive equation in terms of heat flux $q(x)$ as:

$$\frac{dq(x)}{dx} = \rho(x)J^2 [1 + Z(x)T(x)] - \frac{JS(x)q(x)}{\kappa(x)} \quad (4.3)$$

where $Z(x)$ is the figure of merit as:

$$Z(x) = \frac{S^2(x)}{\rho(x)\kappa(x)} \quad (4.4)$$

Eq. (4.2) can be rearranged as Eq. (4.5) as first order equation.

$$\frac{dT(x)}{dx} = \frac{1}{\kappa(x)} [JT(x)S(x) - q(x)] \quad (4.5)$$

For n - type thermoelectric legs, Eq. (4.3) - (4.5) can be discretized along the leg height as a set of algebraic equations represented by Eq. (4.6) - (4.7) [58]. The subscript m denotes the m^{th} TE discrete segment where $m = 0$ and $m = N$ are the segments attached to cold side and hot side junctions respectively. A finite difference method is used to discretize gradient terms using the first order forward difference approximation. Prescribed hot side junction T_N (N^{th} segment) and the cold side junction T_0 (0^{th} segment) temperatures serve as boundary conditions. Current density flux through each leg is a

parametric input to these equations. Since, Eq. (4.6) and Eq. (4.7) are coupled; they have to be solved iteratively to calculate heat fluxes through each TE leg. The properties of thermoelectric legs are averaged over a discrete thermoelectric segment. These calculations are performed for n- and p - type leg of the TE couple.

$$T_{m+1} = T_m + \frac{dx}{\kappa_m} [JT_m S_m - q_m] \quad (4.6)$$

$$q_{m+1} = q_m + \left[\rho_m J^2 (1 + Z_m T_m) - \frac{JS_m q_m}{\kappa_m} \right] dx \quad (4.7)$$

The leg efficiency is the ratio of the electric power generated to the thermal power available at hot side junction. For the n- or p- type leg, this may be expressed as [58].

$$\eta_{n,p} = \frac{J_{n,p} \left(\int_0^L S_{n,p}(x) \frac{dT(x)}{dx} dx + J_{n,p} \int_0^L \rho_{n,p}(x) dx \right)}{q_{h_{n,p}}} \quad (4.8)$$

The first term in the numerator is the summation of Seebeck potentials along the leg height, and the second term is the potential loss due to electric resistance. For a module comprised of a single n and single p type leg, the efficiency can be expressed:

$$\eta_T = \frac{\eta_p Q_{h_p} + \eta_n Q_{h_n}}{Q_{h_p} + Q_{h_n}} = \frac{\eta_p q_{h_p} A_p + \eta_n q_{h_n} A_n}{q_{h_p} A_p + q_{h_n} A_n} \quad (4.9)$$

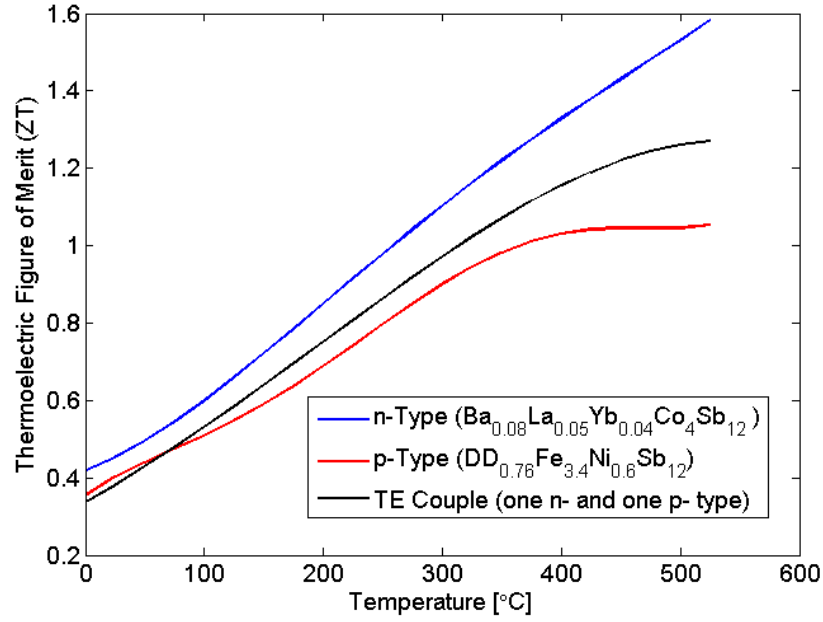


Figure 4.2. ZT curves for the Skutterudites [8,9].

The mesh independence was first verified assuming a skutterudite module, n-type $\text{Ba}_{0.08}\text{La}_{0.05}\text{Yb}_{0.04}\text{Co}_4\text{Sb}_{12}$ and p-type $\text{DD}_{0.76}\text{Fe}_{3.4}\text{Ni}_{0.6}\text{Sb}_{12}$ TE material (as shown in Figure 4.2 [8,9]). The spatial varying material properties $S(x)$, $\rho(x)$ and $\kappa(x)$ were tabulated as functions of temperature. The numerical code uses a data lookup function to read the corresponding material property table and derives value using linear interpolation. The leg efficiencies were calculated using Eq. (4.8) for n- and p- type skutterudite legs at $J_p = 50.9 \text{ A/cm}^2$ and $J_N = -37.1 \text{ A/cm}^2$ respectively. The cold side temperature T_c is fixed to 100°C for calculations throughout this study. The junction temperature difference ΔT ($T_H - T_C$) was set to 450°C and leg height (L_x) as 10 mm. The provided values for $J_p = 50.9 \text{ A/cm}^2$ and $J_N = -37.1 \text{ A/cm}^2$ are the optimal current flux densities for $\Delta T = 450^\circ\text{C}$, L_x as 10 mm which have been discussed later. The respective leg efficiencies were plotted versus increasing counts of discrete segments along leg height (mesh size - N_x) as shown in Figure 4.3. It was found that the solutions vary less than 0.02% from the finest mesh if

a mesh size of 80 is employed. However, the value of $N_x = 500$ is used throughout remaining calculations in this chapter.

Figure 4.4 shows the temperature and heat flux profiles along the TE legs for Skutterudite. Since material properties are functions of temperatures, we observe spatial variations in flux profiles. It should be noted that temperatures of TE segments must match at the boundary junctions whereas the respective heat fluxes do not match since input current densities are different.

Eq. (4.8) was used to calculate respective leg efficiencies for various electric current densities. Figure 4.5 shows that there exists an optimal current density for each n or p type leg which can be explained by Eq. (4.8). The magnitude of the numerator will decrease for lower current density values; however the total voltage potential will decrease with higher current density values with increasing electric resistive potential loss. Table 4.1 summarizes the optimal conditions for both leg types; it is noteworthy that n-type legs are more efficient than their counterpart p-type legs.

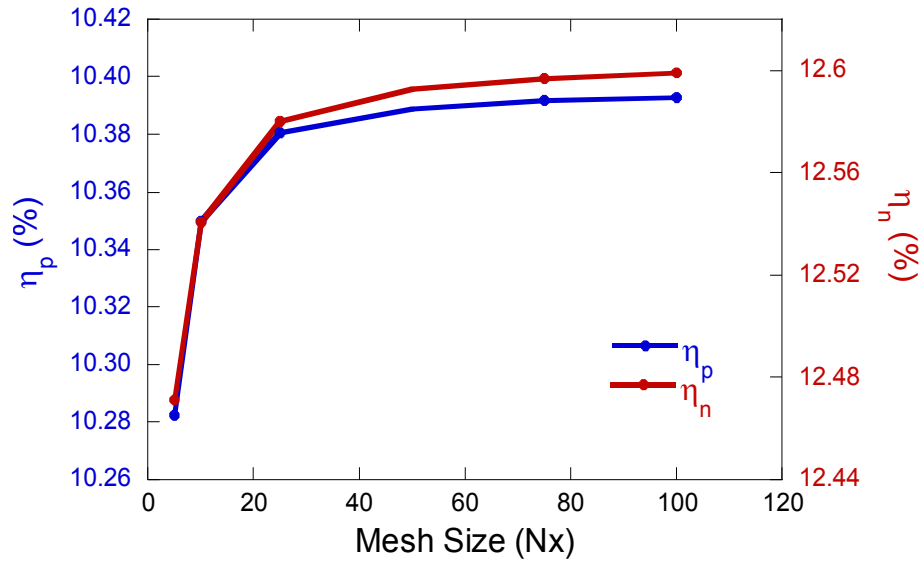


Figure 4.3. Mesh independence study at respective current density fluxes at $J_p = 50.9 \text{ A/cm}^2$, $J_n = -37.1 \text{ A/cm}^2$, $\Delta T = 450 \text{ }^\circ\text{C}$ and $L_x = 10 \text{ mm}$.

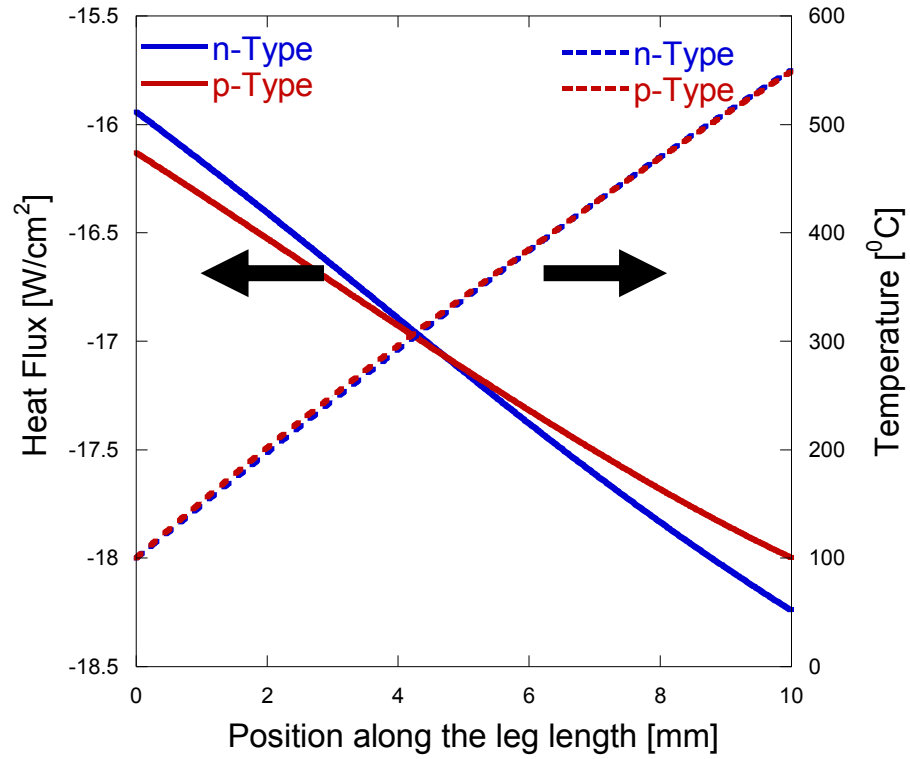


Figure 4.4. Heat flux and temperature profiles along the TE legs at $J_p = 50.9 \text{ A/cm}^2$, $J_N = -37.1 \text{ A/cm}^2$, $\Delta T = 450^\circ\text{C}$ and $L = 10 \text{ mm}$.

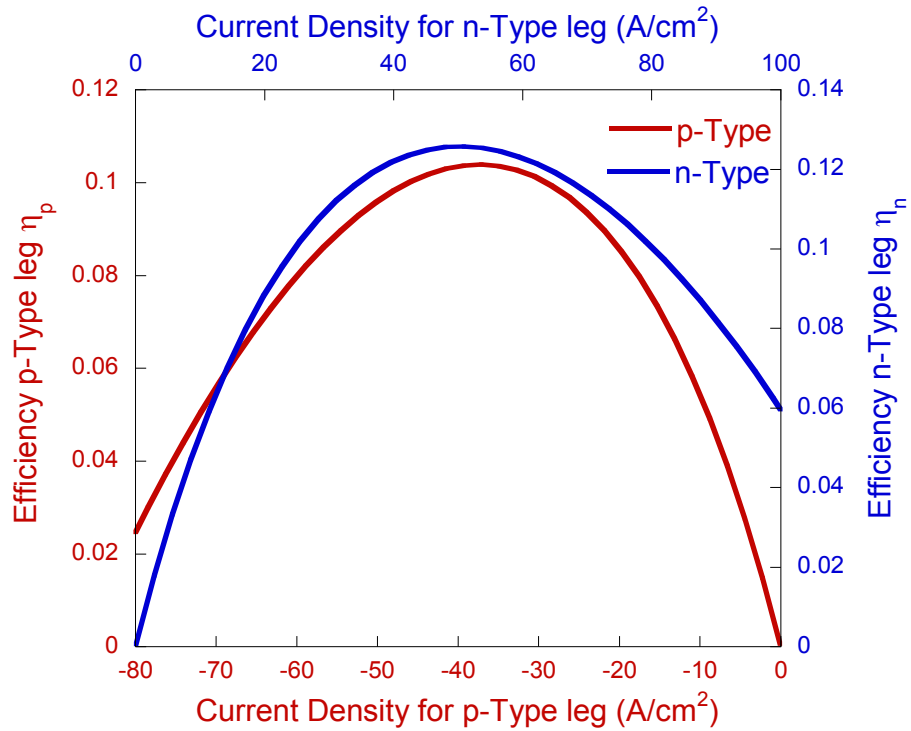


Figure 4.5. Respective leg efficiencies vs. input current density fluxes with $\Delta T = 450^\circ\text{C}$ and $L = 10 \text{ mm}$.

Table 4.1. Optimal current density values for Skutterudites for leg height $L_x = 10$ mm

$\Delta T_{\text{Junction}}$ (°C)	$\eta_{\text{Peak,n}}$	J_n (Opt.) (A/cm ²)	$\eta_{\text{Peak,p}}$	J_p (Opt.) (A/cm ²)
450	0.126	50.32	0.104	-37.34
350	0.101	40.53	0.084	-29.83
250	0.074	30.00	0.061	-21.76
150	0.045	18.64	0.036	-13.26
50	0.015	6.42	0.012	-4.42

4.4 Thermoelectric Module Optimization

As represented in Figure 4.1, the TE module modeled here consists of a single n- and single p-type TE leg. At steady-state operation the electric current is identical through both legs, as such the ratio of cross-sectional area can be represented as $|-J_p A_p| = |J_n A_n| = |I|$. The following analyses highlight the implication of parameters such as input current density flux, TE leg area ratio (A_n/A_p), junction temperatures and leg height on the thermoelectric module efficiency.

First, the module efficiency dependence on the area ratio was examined. Figure 4.6 shows the module efficiency computed by Eq. (4.9) for various area ratios (A_n/A_p) at $\Delta T = 450^\circ\text{C}$ and $L_x = 10$ mm. For Skutterudites, the maximum module efficiency (11.33%) occurs at optimal area ratio of 0.8. The module efficiency, equation (Eq. (4.9)), doesn't change as long as the area ratio (A_n/A_p) remains constant which also limits J_n for a given value of J_p . This implies that the proper sizing of A_p can help to achieve the maximum

module efficiency. However, the sizing of A_P (or A_N) will depend on the magnitudes of electric current and thermal energy considerations

The TEM efficiency variation with leg height was studied by fixing the area ratio at 0.8. The results shown in Figure 4.7 and Figure 4.8 demonstrate the impact of leg height on module efficiency at various current density fluxes and heat fluxes, respectively. An optimal condition exists for both of these parameters indicating that leg height cannot be independently optimized without considering local heat transfer conditions within the TEG. Since most TEG designs employ a flow-path that subjects TE modules to varying temperatures (hottest at inlet and coldest at outlet of TEG), a truly optimal design will then require differing leg heights or fill fractions (shown later) at various points in the gas path due to changing heat fluxes at various duty cycles.

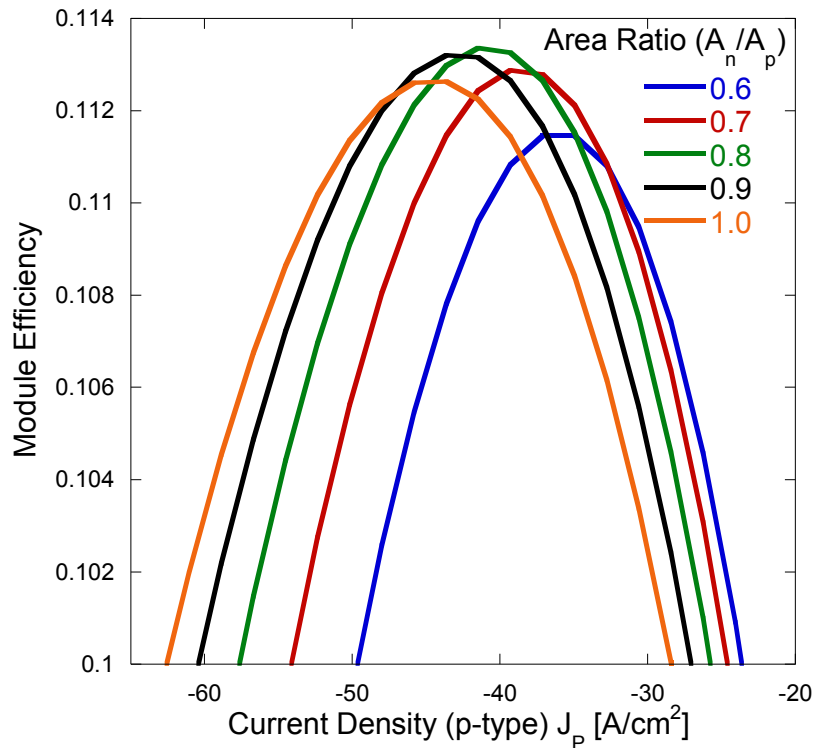


Figure 4.6. TE Module vs. Current Density Values at $\Delta T = 450^\circ\text{C}$ and $L_x = 10\text{ mm}$.

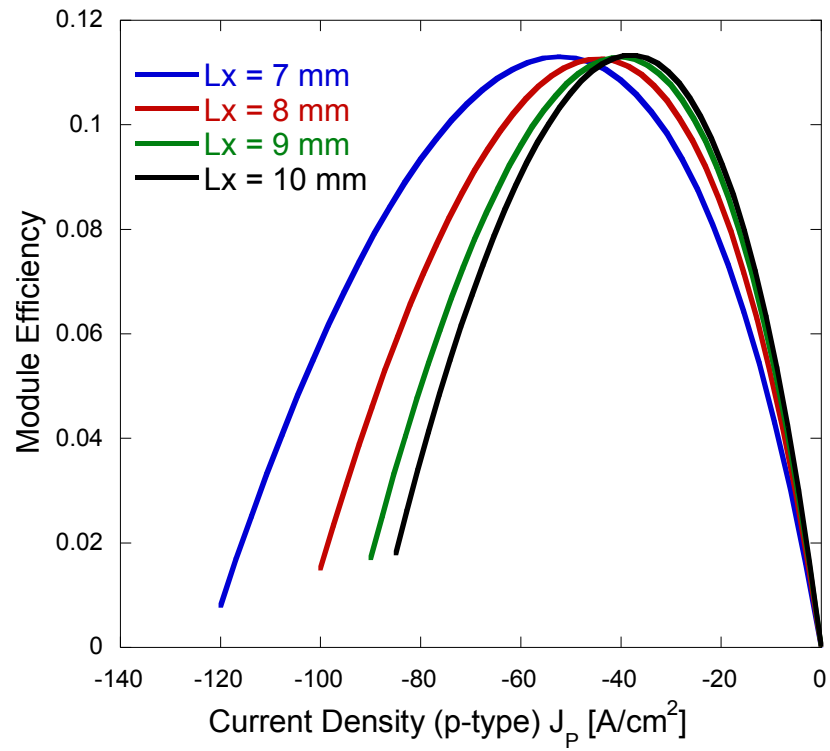


Figure 4.7. TE efficiency vs. J_p for various leg heights at $\Delta T = 450$ °C and $A_N/A_P = 0.8$.

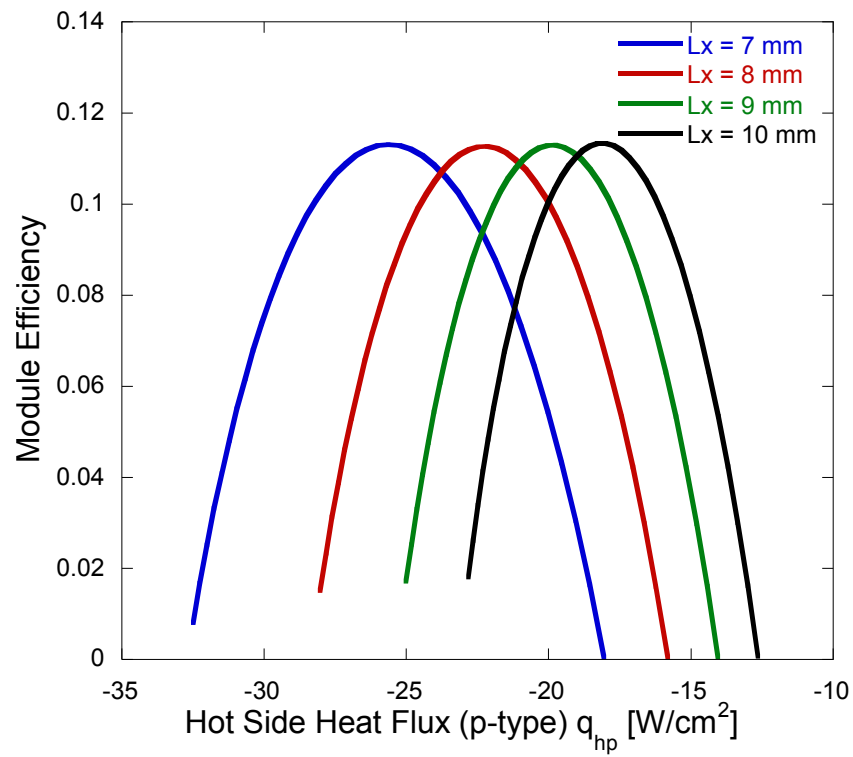


Figure 4.8. TE efficiency vs. hot side heat flux for various leg heights at $\Delta T = 450$ °C and $A_N/A_P = 0.8$.

Figure 4.9 and Figure 4.10 show the variation in module efficiency with respect to varying hot side inputs (J_p , q_{HP}) at $L_x = 10$ mm and $A_N/A_P = 0.8$ for various junction temperatures. There is an upper limit for a given ΔT across a TE module. The possible maximum module efficiency decreases with decreasing ΔT across junctions. These plots serve as a tool for thermoelectric design based on operating regimes (junction temperatures).

For skutterudites used here, the maximum module efficiency (11.35%) occurs at an optimal area ratio of 0.8 for specified conditions of $\Delta T = 450^\circ\text{C}$ and $L_x = 10$ mm. The cross-sectional areas of the TE legs can be varied without affecting the module efficiency as long as A_N/A_P ratio is constant. For a given A_N/A_P and ΔT , maximum efficiency is attainable at different J_p or q_{HP} . However, maximum possible efficiency is limited by ΔT and decreases with decreasing thermal gradient across junctions (ΔT).

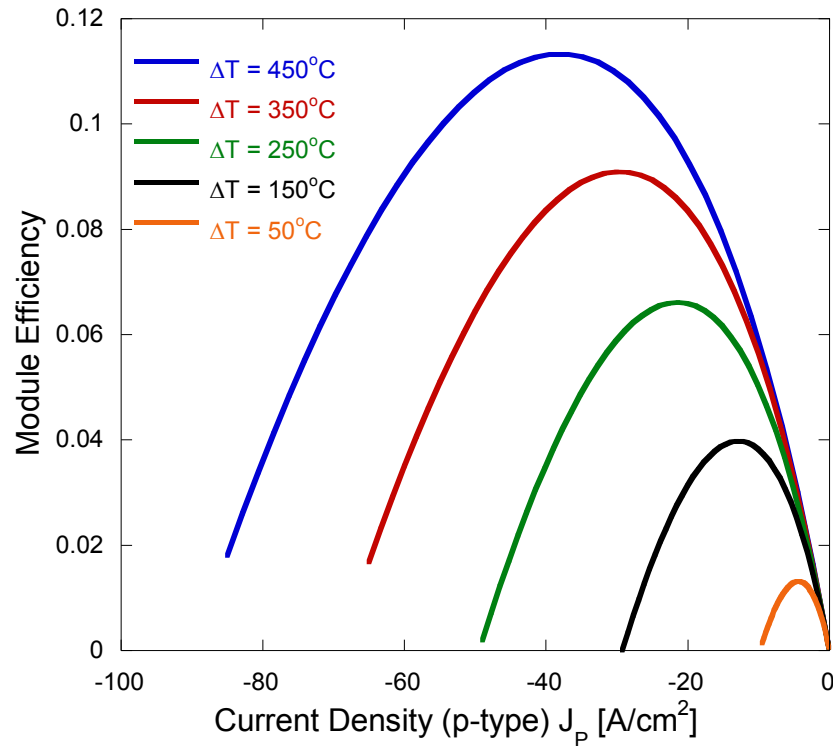


Figure 4.9. TE efficiency vs. J_p for various ΔT at $L_x = 10$ mm and $A_N/A_P = 0.8$.

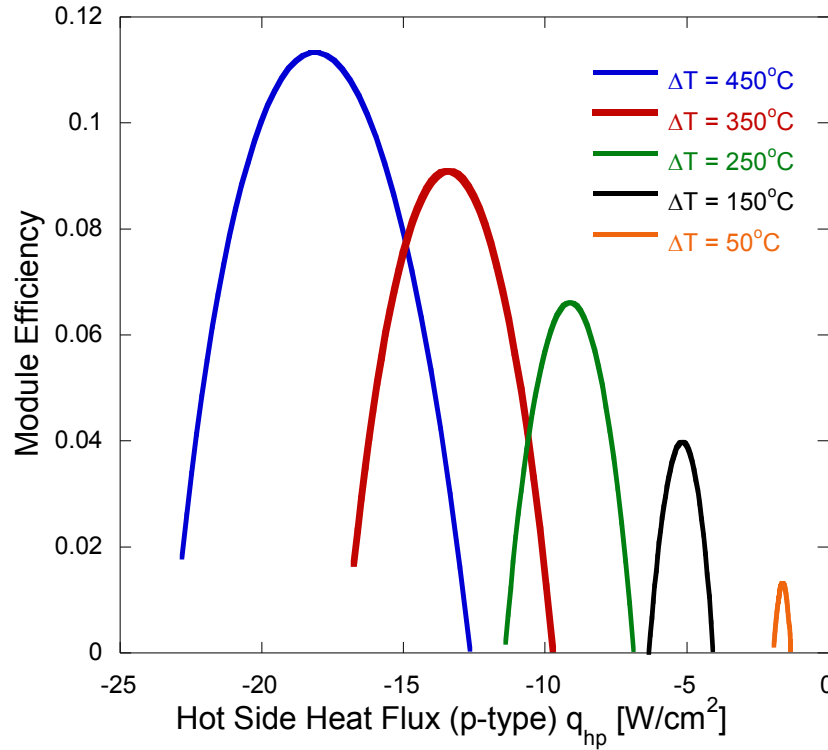


Figure 4.10. TE efficiency vs. hot side heat flux for various ΔT at $L_x = 10$ mm and $A_N/A_P = 0.8$.

4.5 Thermoelectric Design for TEG Optimization

As discussed previously, thermal energy can be extracted from exhaust gas for thermoelectric power generation. Waste heat extraction can be facilitated by allowing poor conducting gas to pass through a heat transfer mechanism such as a heat exchanger. Peak exhaust gas temperatures lie in the range of 550°C to 650°C providing the thermoelectric modules a waste heat energy supply in the range of 10 kW a mid-sized vehicle [55]. The following steps illustrate the approach taken for thermoelectric designing of such systems

- 1) The average heat flux is calculated for a given TE module area based on fill fraction.
- 2) The calculated heat flux is matched to that of a TE module at a given leg height, ΔT , and A_N/A_P .

3) Subsequently, electric power estimates and volume of TE materials are calculated.

Here, two scenarios are considered to assess the efficacy of thermoelectric design as represented by Figure 4.11. . The heat transfer happens across a heat exchanger surface having width = 0.5 m and length = 0.5m. Case 1 represents configurations where heat transfer and temperature are uniform at the heat exchanger surface in a TEG system. In Case 2, the heat transfer and temperature profiles at surface vary along the flow direction. The variation along the flow direction can be visualized as a series of step decrements numbering 1 to 5 as shown in Figure 4.11 for ease of calculation. One step length is equal to $1/5^{\text{th}}$ of the flow direction length. Certain percentage of the heat transfer area is covered by thermoelectric legs and is represented by fill fraction. 90% of incident thermal energy is assumed to be conducted through the thermoelectric legs and thus generating electrical power. The remaining 10% is assumed to be lost through the conduction in insulators filled between TE legs and via radiation losses. The optimal leg area ratio (A_N/A_P) of 0.8 is taken for all subsequent calculations. The cold side junction temperature is approximated as the coolant temperature and kept fixed at 100°C.

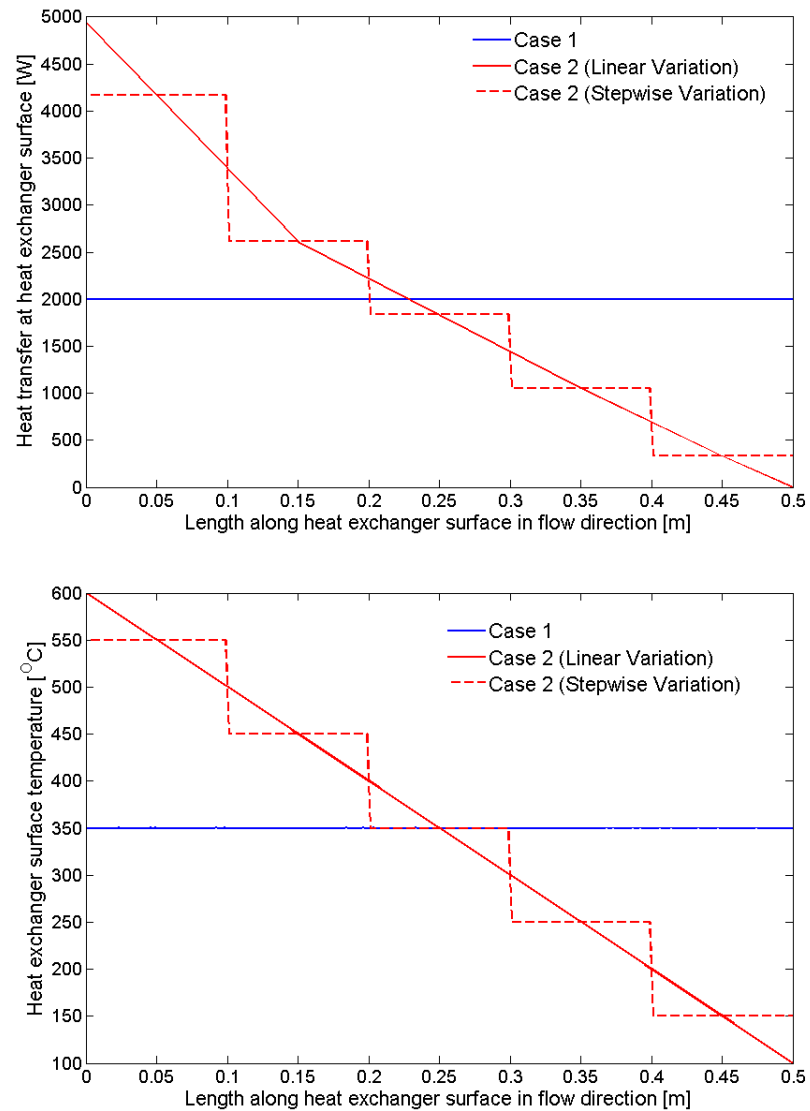


Figure 4.11. Variation of heat transfer and temperature over a heat exchanger surface for Case 1 and Case 2. The linear variation is approximated as stepwise profile in five steps for Case 2.

4.5.1 Case 1: Uniform Heat Transfer and Temperature

In this case, there is a uniform supply of 10 kW thermal energy through the exhaust gas over 2500 cm² of heat transfer surface area which is in conjunction with hot side surface of thermoelectric modules. For example, after deducting the losses and transfer inefficiencies, the average heat flux value over the surface is 18 W/cm² for a 20% fill

fraction and varies with different fill fraction values. A uniform $\Delta T = 250^\circ\text{C}$ is assumed across TE hot and cold side junctions. The calculations for Skutterudite TE modules were run for a range of TE leg heights and fill fractions. Figure 4.12 shows the estimated power generation for a given thermal energy and surface temperature conditions. Figure 4.13 shows the volume of TE material required to generate power that appears in Figure 4.12. The fill fraction increases with leg height to match surface heat flux and generate same order of electrical power. This in turn increases the required amount of TE material volume. The TE modules with leg height of 3.75 mm and a fill fraction of 15% predict generation of 593.8W of electrical power; and require just 140.6 cm^3 of skutterudite material over 2500 cm^2 of heat exchanger area.

4.5.2 Case 2: Varying Heat Transfer and Temperature

This case mimics transfer in a TEG that has a gas path that has successive heat extraction along its length. The heat transfer and temperature profiles are equally distributed area-wise in five steps along the flow direction. Figure 4.14 shows the electrical power generated at various leg heights (3mm – 7mm) for optimal fill fraction. The optimal fill fraction along the steps in the flow direction and required total material volumes are plotted in Figure 4.15. The electrical power generation capacity of TE couples decreases considerably along the flow direction and is less than 10W for Step 5 signifying strong dependence of TE efficiency on the junction ΔT . TE modules with leg height of 4.5mm and having a fill fraction of 20% for Step1 and 15% for Steps 2-5 generates electrical power of 758.9 W; requiring 33.8 cm^3 of TE material. The thermoelectric couples in the Step 5 for this configuration only generate 3.39 W of electrical power.

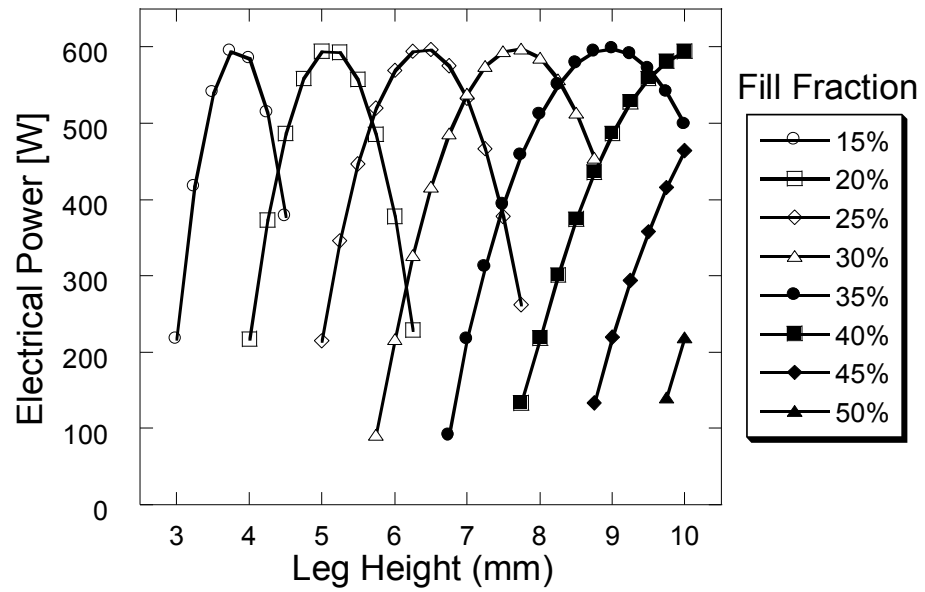


Figure 4.12. Electrical power estimates versus leg height at different fill fraction for Case 1 with area ratio (A_N/A_P) fixed at 0.8 for skutterudite.

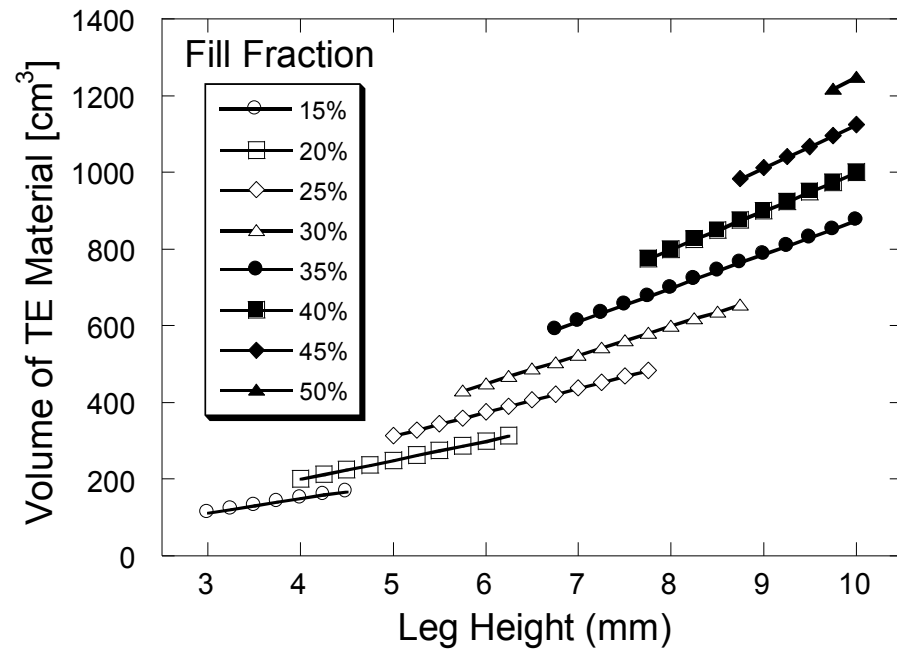


Figure 4.13. Required volume of TE materials for Case 1 at different fill fractions.

Electrical power generation at various leg height and optimized fill fraction for steps 1 to 5

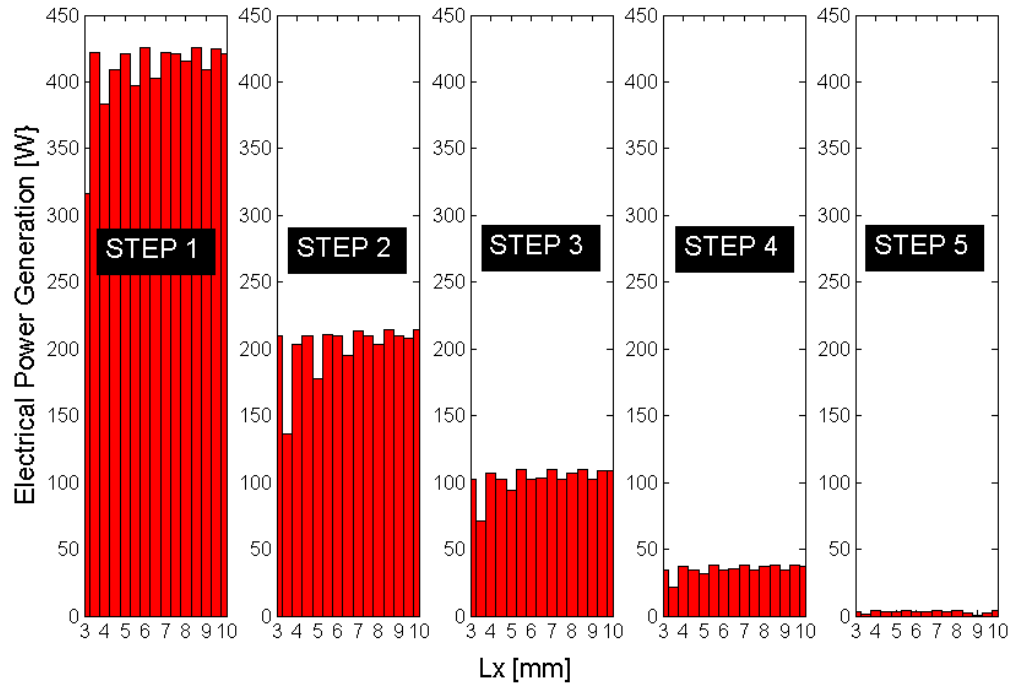


Figure 4.14. Electrical power generation at various leg heights for optimal fill fraction and $A_N/A_P = 0.8$. The steps 1-5 represent each row of TE couples arranged along the flow direction.

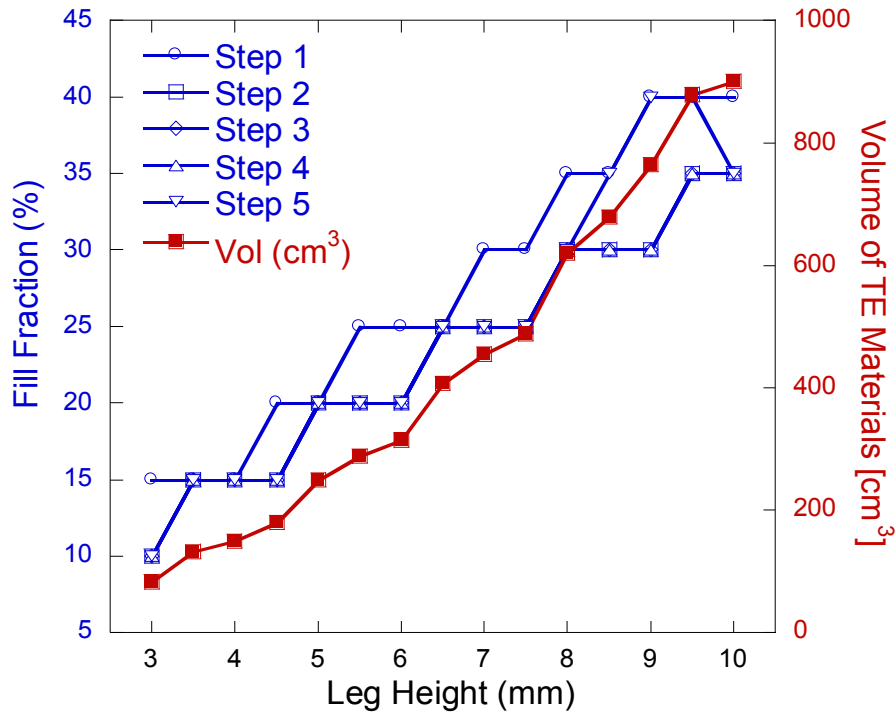


Figure 4.15. Optimal fill fractions at various leg heights for Steps 1-5 varying along the flow direction (Case 2). The right axis shows the required volume of Skutterudite material.

Table 4.2 summarizes the energy distribution and optimal configuration for both cases. The optimal configuration for Case 2 suggests having a variable fill fraction along flow direction.

Table 4.2. Electrical power generation for both cases.

	Surface Heat transfer [kW]	Electrical Power [W]	Efficiency [%]	Optimal leg height (mm)	Optimal Fill fraction [%]	Volume of Skutterudite [cm ³]
Case 1	10.0	593.8	5.9	3.75	15	140.6
Case 2	10.0	758.9	7.6	4.5	20,15,15,15,15	180

4.6 Conclusions

A numerical method has been implemented and simulated to calculate heat transfer and temperature profiles for n and p type thermoelectric legs for Skutterudite material. The leg efficiencies are found to be strong functions of electric density (current), junction temperature differences, and leg height. Leg height, fill fraction, and area ratio (A_N/A_P) play an important role in TEM optimization for any maximum power generation study. However, maximum module efficiencies are limited by junction temperatures. Iterative method provides accurate design tools to optimize TEMs for cases related to automotive waste heat recovery. The careful selection of leg height and fill fraction helps to meet the maximum electrical power generation while minimizing material requirements. For a fixed heat exchanger surface, to generate same amount of power, longer thermoelectric legs require higher fill fractions or larger cross-sectional areas to match the hot side heat flux. But this in turn increases the volume of Skutterudite material required. For automotive applications considered here (10 kW heat supply over 0.25 m² of heat exchanger surface), leg heights in range of 3 mm to 5 mm are found to effectively generate maximum possible electrical power.

CHAPTER 5. EFFECT OF HOT WALL AXIAL CONDUCTION ON THE PERFORMANCE OF THERMOELECTRIC GENERATORS

This chapter discusses the axial thermal conduction calculations in the metallic wall liner sandwiched between heat exchanger and the thermoelectric module. The previously discussed numerical model has been improved to include axial conduction effects and solve thermal fluxes, and temperature profiles in the liner. The simulations are run with various parameters - inlet conditions (flow rates and exhaust inlet temperatures), liner material (copper and stainless steel), and liner thickness. Subsequently, the conduction effects on the temperature distributions and power generation estimates are presented.

5.1 Axial Conduction in Hot Wall Liner

The axial conduction in the metal wall liner could be detrimental for proper functioning of a thermoelectric generator (TEG) since it serves to reduce the effective temperature difference between thermoelectric legs and hence, the power generation. The magnitude of conduction will vary with the material and the thickness of the wall liner, as well as the design of the TEG itself.

The TEG numerical model presented in previous chapters is modified further to study the axial conduction effects on TEG performance. The TEG output power dependence on geometry and inlet flow conditions has been explored and discussed in detail in CHAPTER 2.

5.2 Numerical Model

The schematic of the lower half of a thermoelectric generator is presented in Figure 5.1. Hot gas flows axially in the upper passage from left to right in the Figure. The top surface in Figure 5.1 is a symmetry plane since only half of the TEG system is being modeled as mentioned in CHAPTER 2. The hot gas wall liner is the metallic TEG base in which axial conduction is being considered. As we are considering application to an automotive exhaust, a stainless steel material would generally be employed in order to sustain the hot and corrosive exhaust environment. Since the TEM array located below this TEG liner is of low thermal conductivity, we presume that axial conduction effects are dominated by the metal wall material and for this reason axial conduction is neglected in the other layers below this liner.

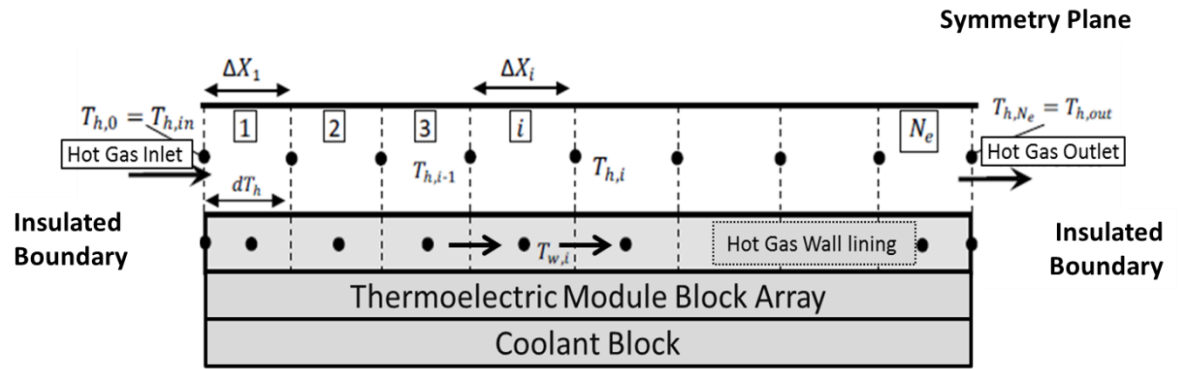


Figure 5.1. Schematic of a longitudinal thermoelectric generator with control volumes for hot gas passage and the hot gas wall lining

Figure 5.2 shows the thermal energy transport through the control volumes (CV) at the i^{th} location from the exhaust gas entry. Here, $H_{\text{Gas},i}$ represents the gas enthalpy available at the left face of gas CV and is calculated as given in Eq. (5.1). Here, C_p is specific heat capacity of exhaust gas and \dot{m} is the mass flow rate. The quantity $T_{\text{gavg},i}$ in

Figure 5.2 is the average gas bulk temperature in the i^{th} CV. The quantity $Q_{\text{gas},i}$ is the thermal energy transferred by the heat exchanger to hot wall CV and is calculated as the difference of gas enthalpies at adjacent faces ($H_{\text{gas},i} - H_{\text{gas},i+1}$) in the gas CV.

$$H_{\text{gas},i} = \dot{m} C_p T_{\text{gas},i} \quad (5.1)$$

The quantity $T_{w,i}$ is the cell centroid value of wall temperature in i^{th} hot wall liner CV. The ' T_w ' terms in $i-1^{\text{th}}$ and i^{th} liner CVs are coupled due to axial conduction term ' $Q_{\text{Axial},i}$ ' as shown in Eq. (5.2). Here, $R_{w,i}$ is the axial thermal resistance, k_w is the thermal conductivity of the wall material, and t_w is the thickness of liner.

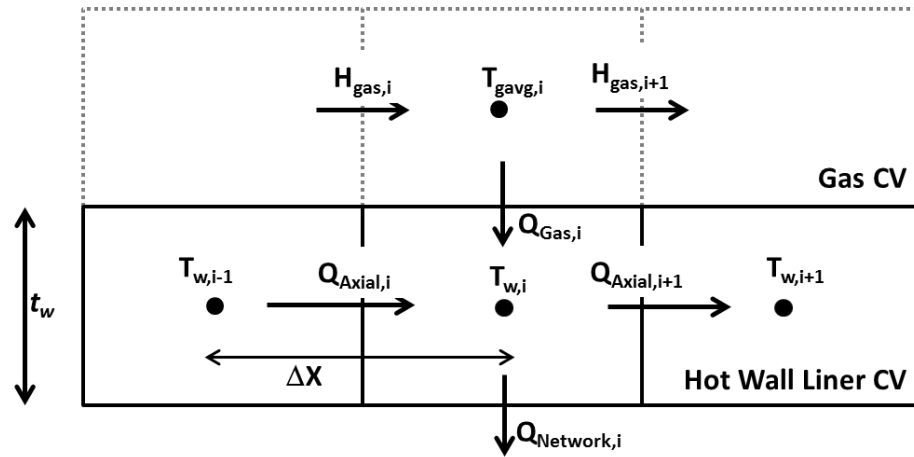


Figure 5.2. Thermal energy transport in i^{th} hot wall liner and gas CV

$$Q_{\text{Axial},i} = \frac{(T_{w,i-1} - T_{w,i})}{R_{w,i}}; \quad R_{w,i} = \frac{\Delta x}{\kappa_w t_w} \quad (5.2)$$

The TEG resistance model discussed in CHAPTER 2 was modified to account for axial conduction calculations in the TEG metallic base as shown in Figure 5.3. The resistance network was split along the TEG metallic wall resistance term ' $R_{\text{TEG,base}}$ '. Hence $Q_{\text{Network},i}$ in Figure 5.2 is equivalent to thermal energy flowing through the

resistance $R_{\text{TEG,base}}$ in Figure 5.3. The axial conduction term in Eq. (5.2) is discretized using a centered finite difference as:

$$T_{w,i-1} - 2T_{w,i} + T_{w,i+1} = R_{w,i} (Q_{\text{Network},i} - Q_{\text{Gas},i}) \quad (5.3)$$

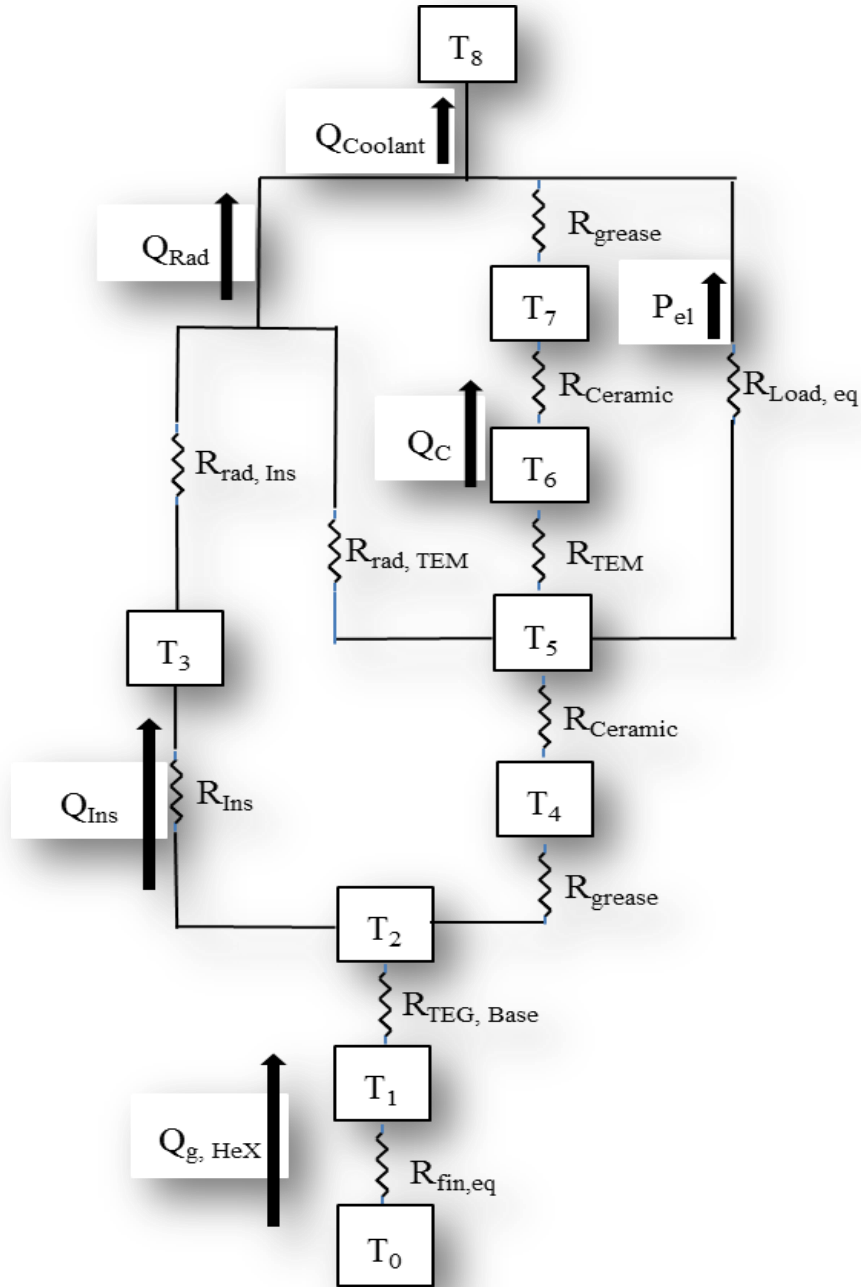


Figure 5.3. Thermal resistance network in a control volume

Now, the bulk mean gas temperature in gas CV is defined by Eq. (5.4). The heat transferred through the heat exchanger ($Q_{gas,i}$) is equal to energy which is being conducted through the 1D thermal resistance network between $T_{gavg,i}$ and $T_{w,i}$ because of symmetry plane in gas CV. The thermal resistance between these two temperature nodes is composed of heat exchanger resistance ($R_{fin,eq}$) and half of liner conduction resistance $\left(\frac{t_w/2}{\kappa_w w \Delta x} \right)$. Here w is the width of TEG parallel to flow direction; and Δx is the discrete step size along flow direction. Using these relationship, the gas temperature at right face of i^{th} gas CV ($T_{g,i+1}$) can be defined as a linear combination of $T_{g,i}$ and $T_{w,i}$ as shown in Eq. (5.5). The coefficients a , b and c are defined in Eq. (5.6). The heat energy transferred through the heat exchanger to the wall liner ($Q_{gas,i}$) is then calculated by Eq. (5.7).

$$T_{gavg,i} = (T_{g,i} + T_{g,i+1}) / 2 \quad (5.4)$$

$$T_{g,i+1} = \frac{1}{c} (aT_{g,i} + bT_{w,i}) \quad (5.5)$$

$$a = \frac{1}{2} \left[\dot{m}C_p - \frac{1}{R_{fin,eq} + \frac{t_w/2}{\kappa_w w \Delta x}} \right]$$

$$b = \frac{1}{R_{fin,eq} + \frac{t_w/2}{\kappa_w w \Delta x}} \quad (5.6)$$

$$c = \frac{1}{2} \left[\dot{m}C_p + \frac{1}{R_{fin,eq} + \frac{t_w/2}{\kappa_w w \Delta x}} \right]$$

$$Q_{gas,i} = \frac{T_{gavg,i} - T_{w,i}}{R_{fin,eq} + \frac{t_w/2}{\kappa_w w \Delta x}} \quad (5.7)$$

Hence, the net energy imbalance in the i^{th} liner CV ($Q_{\text{Err},i}$) can be calculated as :

$$Q_{\text{Err},i} = Q_{\text{Axial},i} + Q_{\text{Gas},i} - Q_{\text{Axial},i+1} - Q_{\text{Network},i} \quad (5.8)$$

Since the temperature terms in the hot gas wall are coupled; temperatures in the resistance network, wall liner temperatures, and gas temperatures in the flow direction have to be solved simultaneously. The leftmost wall face and rightmost wall face of the wall liner were modeled as adiabatic boundaries since these walls are thermally insulated. The hot side wall liner is followed by the thermoelectric module array and coolant supply in transverse direction to exhaust flow as mentioned in the parent TEG resistance model.

5.3 Solution Method

Following methodology was used to solve the axial conduction problem:

- 1) Linearly decreasing profiles for wall liner temperatures (T_w) and gas temperatures (T_g) are the initial guess for all control volumes.
- 2) The resistance network model is solved to calculate $Q_{\text{Network},i}$ on the basis of updated $T_{w,i}$ for all CVs
- 3) $T_{g,i+1}$ (Eq. (5.5)) and $Q_{\text{Gas},i}$ $T_{w,i}$ (Eq. (5.7)) are computed for all CVs which are based on $T_{g,i}$ and $T_{w,i}$
- 4) Equation set (Eq. (5.3)) is solved for wall liner temperatures (T_w) in CVs using Gauss-Seidel successive over-relaxation method (GSSOR)[60] until root mean square (RMS) error in $T_{w,i}$ (Eq. (5.9)) falls below 0.001°C

$$\text{RMS Error} = \sqrt{\frac{\sum_i (T_{w,\text{new}} - T_{w,\text{old}})^2}{N}} \quad (5.9)$$

- 5) Updated T_w values are used to calculate net energy imbalances in hot wall CVs denoted by Eq. (5.8).

- 6) If global heat energy imbalance $\sum Q_{\text{Err},i}$ is greater than 0.001W and sum of RMS errors in T_w and T_g are above 0.001°C, steps (2 – 5) are repeated till they satisfy both convergence criteria.

5.4 Results

5.4.1 Liner Material and Thickness Sensitivity

Axial conduction effects were studied for a hot gas flow rate of $\dot{m} = 36\text{g/s}$ and $T_{\text{in}} = 973\text{K}$. TE generator has baseline dimensions of height, width and flow length as 0.038m, 0.224m and 0.4131 m respectively. The front and rear end of wall liner is modeled as adiabatic wall. Materials properties of exhaust gas and thermoelectric components are functions of temperature. Copper (401 W/m²-K) and stainless steel (20 W/m²-K) are selected as wall liner materials to analyze the impact of high and low thermal conductivities. The temperature dependence of thermal conductivity of liner materials is not considered. Hot gas liner thicknesses (t_w) of 5, 10 and 20 mm were considered. Small step size (Δx) of 0.001m was used to run the simulation to check that the coefficients a, b, and c in Eq. (5.6) are greater than zero for numerical stability. Also, grid size suggested by grid independence study is larger than the selected grid size.

Figure 5.4 represents the axial variation of gas bulk temperature for various liner thicknesses for the two different liner materials. Here, the blue lines represent cases with zero axial conduction, while the red lines include this effect. The axial conduction effects are unnoticeable for the relatively low thermal conductivity stainless steel wall but are highly evident in the case of a copper wall. The variations in gas temperatures due to axial conduction effect in copper liner become increasingly higher as gas flow through

the TEG heat exchanger passage. This is due to presence of zero axial conduction fluxes at the entry region (left liner boundary is adiabatic). The thermal resistance due to liner thickness is more profound in stainless steel liner; and hence, it reduces the relative gas temperature and results in less gas temperature drops.

Figure 5.5 shows the axial distribution of liner temperature for the conditions used in Fig. 5.4 for both liner materials. For the copper liner, the axial conduction effects increase with the wall thickness, and differ considerably from non-axial conduction cases. The results are similar for a stainless steel wall but variations in magnitude are much smaller. Figure 5.6 shows the variation in TEM junction temperature difference (ΔT_{TEM}) along the flow direction for conditions used in Fig. 5.4. For the copper liner, the ΔT_{TEM} at the TEG entry is computed to be 328K for a 20 mm thickness with axial conduction while the value grows to 395K with no axial conduction effects. The axial conduction tends to homogenize liner temperature and therefore lowers the ΔT_{TEM} available to TE modules at the inlet region and increases it at the exit region. However, ZT_{TEM} decreases with average TE junction temperature; and hence this lowers the effective thermoelectric generator performance which has been discussed later in this chapter. The order of this similar variation is lower for stainless steel based wall liners.

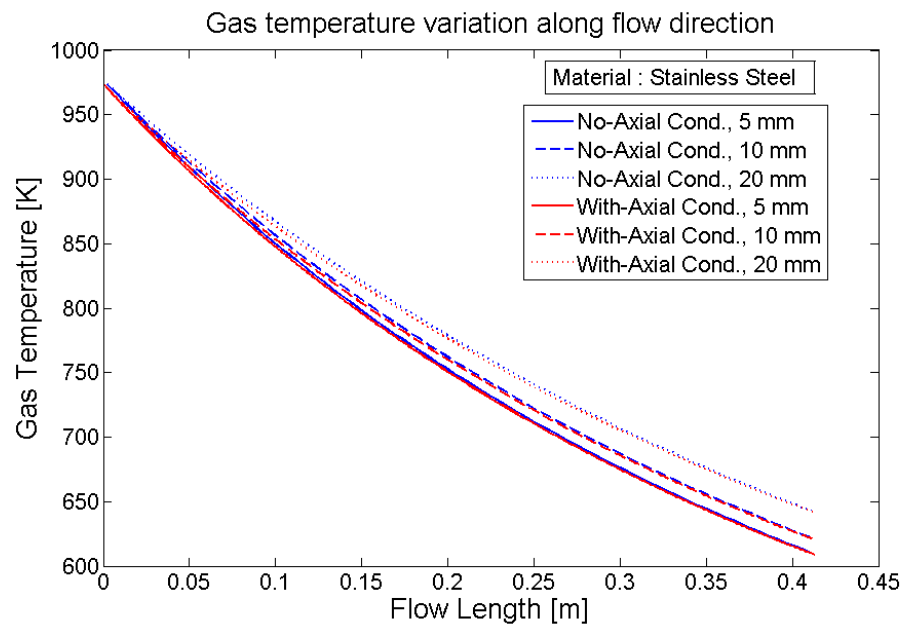
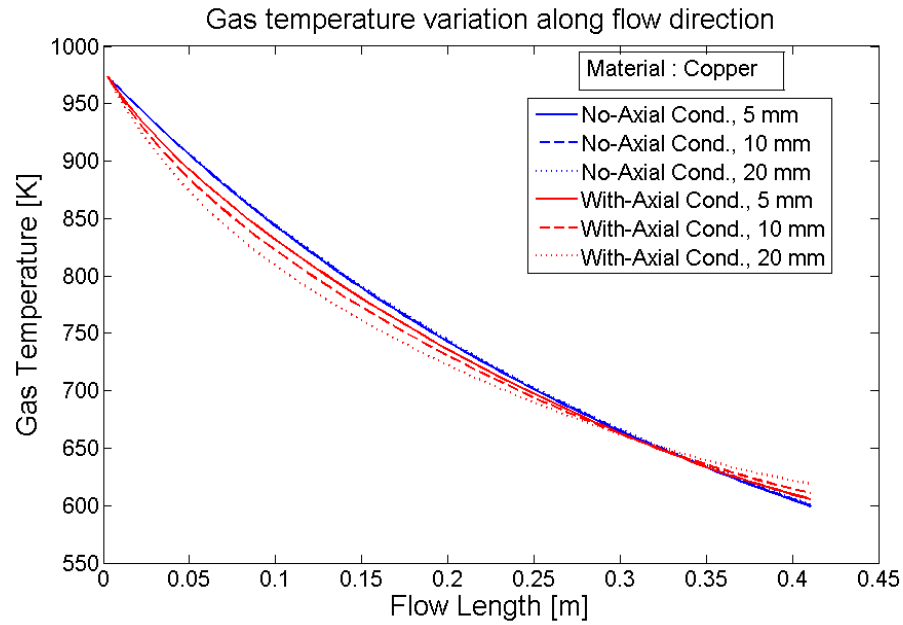


Figure 5.4. Gas temperature variation along the flow direction for (a) Copper and (b) Stainless steel Wall liners at $\dot{m} = 36\text{g/s}$ and $T_{\text{in}} = 973\text{K}$.

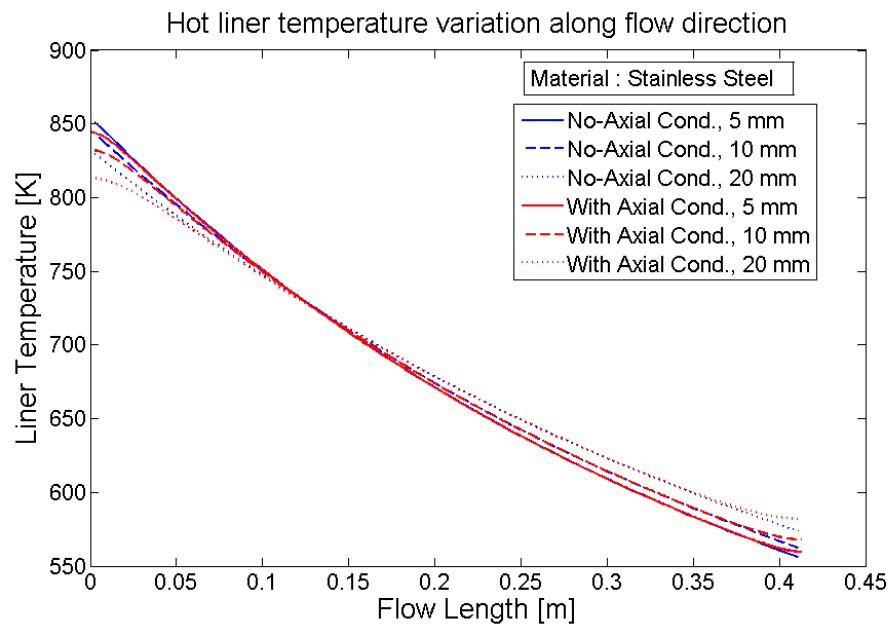
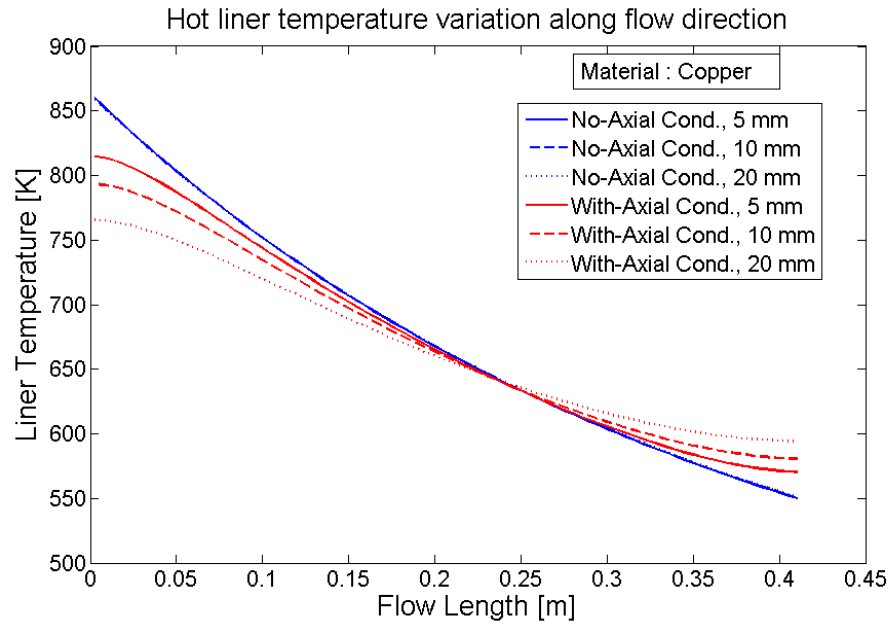


Figure 5.5. Hot wall liner temperature variation along the flow direction for (a) Copper and (b) Stainless steel Wall liners at $\dot{m} = 36\text{g/s}$ and $T_{\text{in}} = 973\text{K}$.

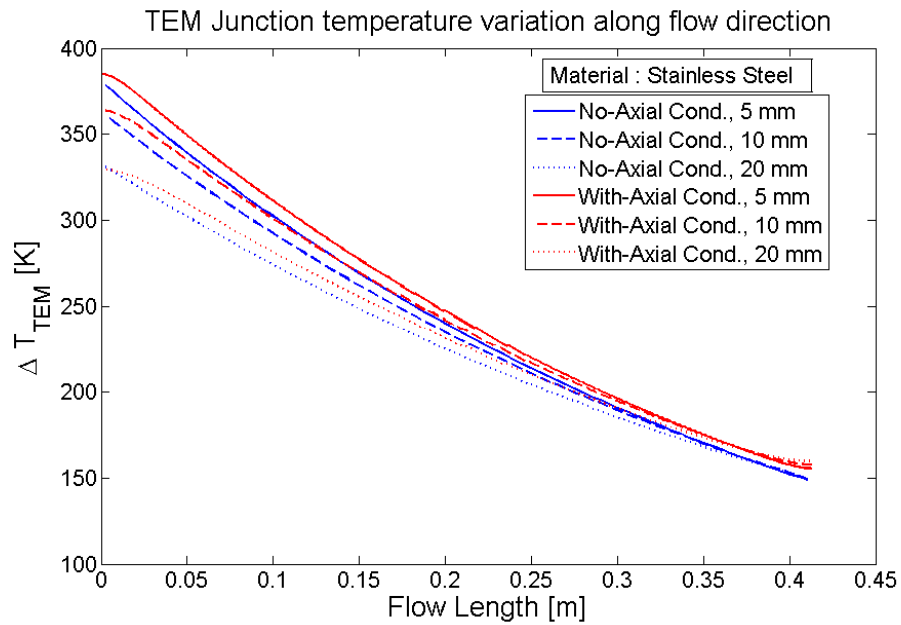
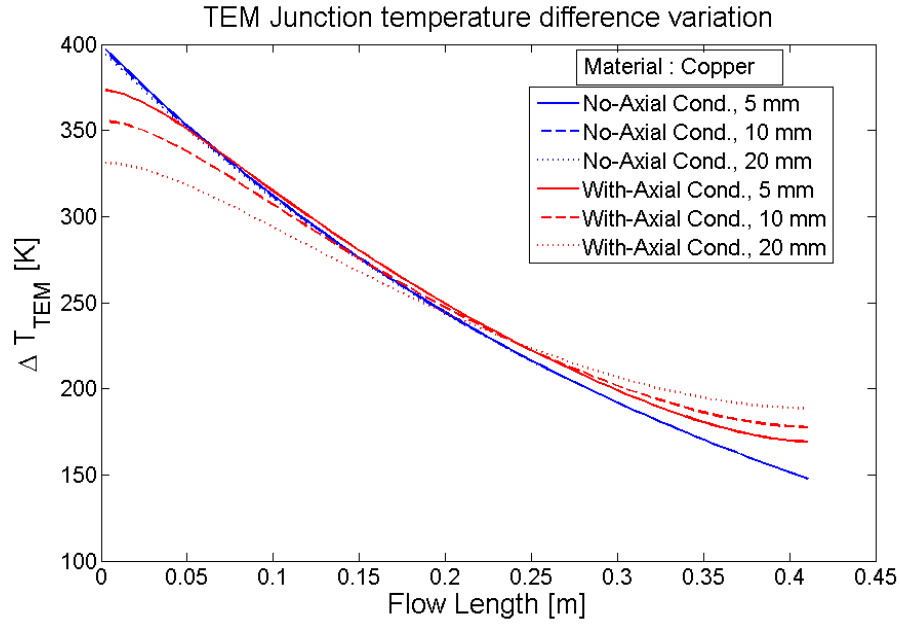


Figure 5.6. TEM junction temperature variation along the flow direction for (a) Copper and (b) Stainless steel Wall liners at $\dot{m} = 36\text{g/s}$ and $T_{in} = 973\text{K}$.

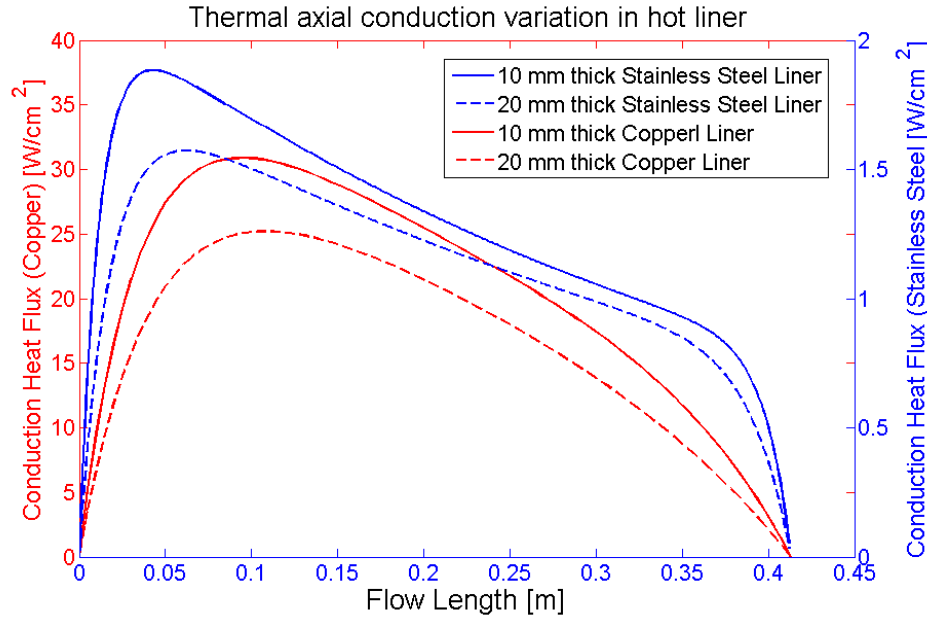


Figure 5.7. Axial conduction flux in wall lining and its variation along the flow direction for Copper and Stainless steel Wall liners at $\dot{m} = 36\text{g/s}$ and $T_{\text{in}} = 973\text{K}$.

The axial conduction fluxes are plotted along the flow direction as shown in Figure 5.7. Since copper is highly thermally conductive material (about 20 times stainless steel), the axial conduction flux has much smoother gradients in the copper liner as compared to that of stainless steel. The magnitude of axial conduction flux decreases with increase in thermal resistance (liner thickness). The flux matches the zero flux boundary condition at both inlet and exit locations. In general, the magnitudes of axial conduction fluxes are found to be higher near the inlet region as compared to exit region due to presence of steeper temperature gradients near inlet region. This in turn lowers the effective ΔT_{TEM} at the entry region and increases ΔT_{TEM} near the TEG exit. Since, TEMs have higher thermoelectric power conversion efficiencies (or ZT_{TEM}) at higher temperatures. This changed ΔT_{TEM} along flow direction deters the TEG power generation characteristics. Table 5.1 summarizes these conduction effects and highlights their impact on the TEG

performance. Inclusion of axial conduction effects in the numerical model predicts lowering of power generation term (P_{Electric}) by 4.5% for the 5 mm copper liner and increases to 13.2% for the 20 mm copper liner. For the stainless steel liner, the power generation lowers by 0.25% for a 5 mm thick wall and increases upto 0.83% for a 20 mm thick wall. The impact of thermal resistance due to liner material and thickness is quite notable for both zero and non-zero conduction effects. TEG with low resistive liner (5 mm, copper) generates 919W of electrical power as compared of 727W for high resistive liner (20 mm, stainless steel). Temperature drop in gas along the flow (ΔT_{Gas}) is 373K for 5 mm copper wall and only 330K for a 20 mm stainless steel wall.

Table 5.1. Parameters representing impact of axial conduction on TEG performance.

	t_w [mm]	Q_{Hex} [W]		P_{Electric} [W]		ΔT_{Gas} [K]	
		Cu	SS	Cu	SS	Cu	SS
No Axial Conduction	5	14830	14398	919	866	373	362
	10	14806	13968	916	816	373	351
	20	14760	13172	910	727	372	330
With Axial Conduction	5	14569	14384	879	864	368	364
	10	14354	13942	848	812	362	353
	20	14039	13130	804	720	354	331

5.4.2 Inlet Condition Sensitivity

The model was also utilized to examine the sensitivity to the inlet flow conditions. The TEG inlet was subjected to low, medium and high levels of flow rates and inlet temperatures. Combinations of gas flow rates such as 5g/s, 25g/s and 50 g/s with inlet temperatures such as 473K, 773K and 1073K were considered. The model was run for a stainless steel liner having 5 mm and 20 mm thicknesses.

Figure 5.8, Figure 5.9 and Figure 5.10 represent the variations in exhaust gas temperature, liner temperature and TE junction temperature difference along the flow direction respectively. The solid lines are for the cases with zero axial conduction effects whereas the dashed lines represent the cases with axial conduction effects included. Cases with medium (25g/s) and high (50g/s) flow rates exhibit less or unnoticeable variations. It is found that axial conduction is most effective with low flow rate cases associated with 5 g/s. The variations in temperature profiles are much higher for a 20 mm liner as compared to a 5 mm liner. Again, these variations increase with increasing inlet temperatures for a fixed flow rate of 5g/s. For the inlet condition (5g/s, 1073K), ΔT_{TEM} at the entry location is predicted to be lowered by 59K and 98K for 5 mm and 20 mm thick wall respectively if axial conduction effects are considered. These results suggest that axial conduction will be most detrimental for cases with low flow rate and high inlet temperatures.

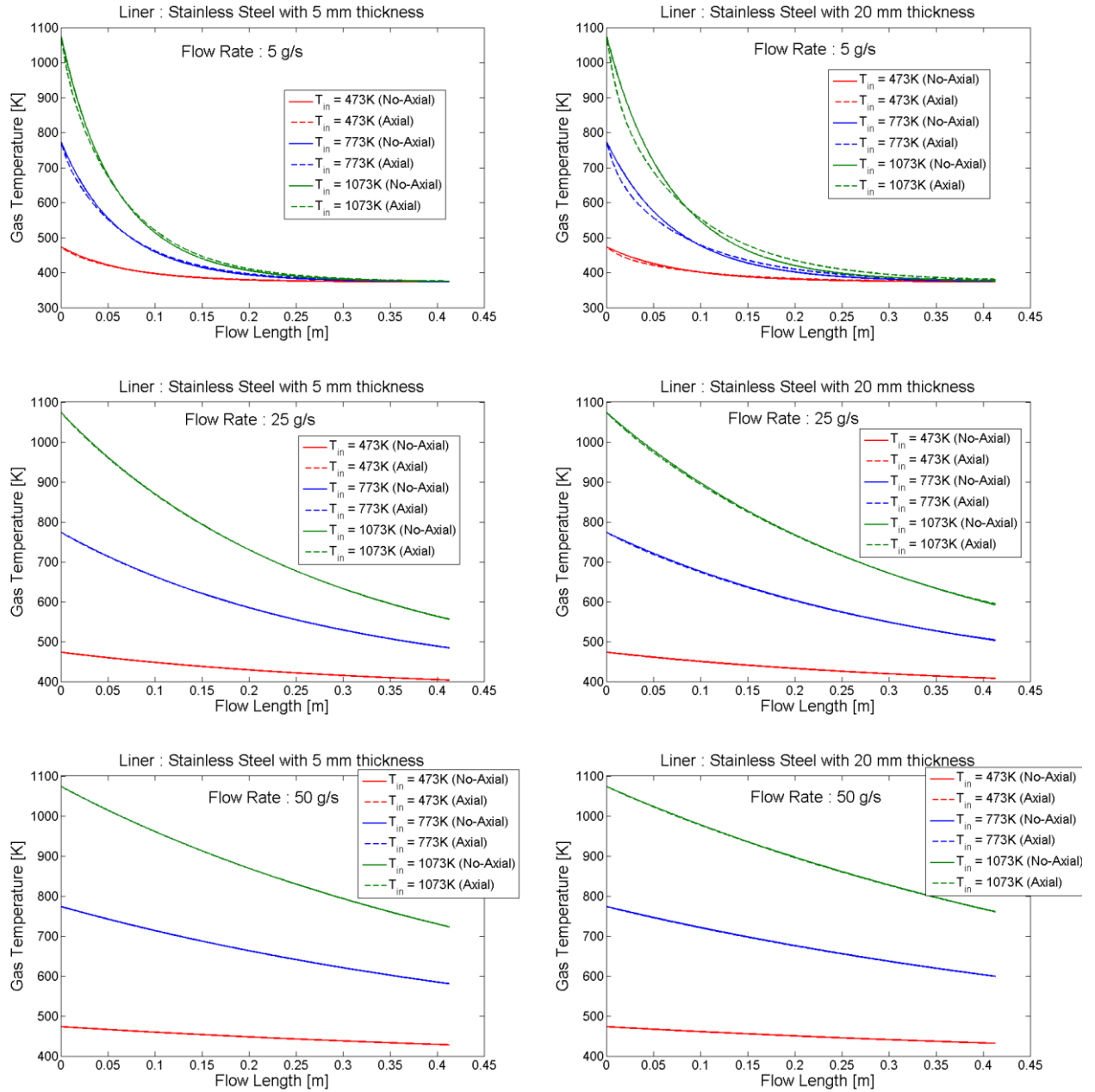


Figure 5.8. Gas temperature variation along the flow direction for 5 mm and 20 mm thick stainless steel liners at inlet temperatures of 473K, 773K and 1073K with flow rates 5g/s, 25g/s and 50g/s.

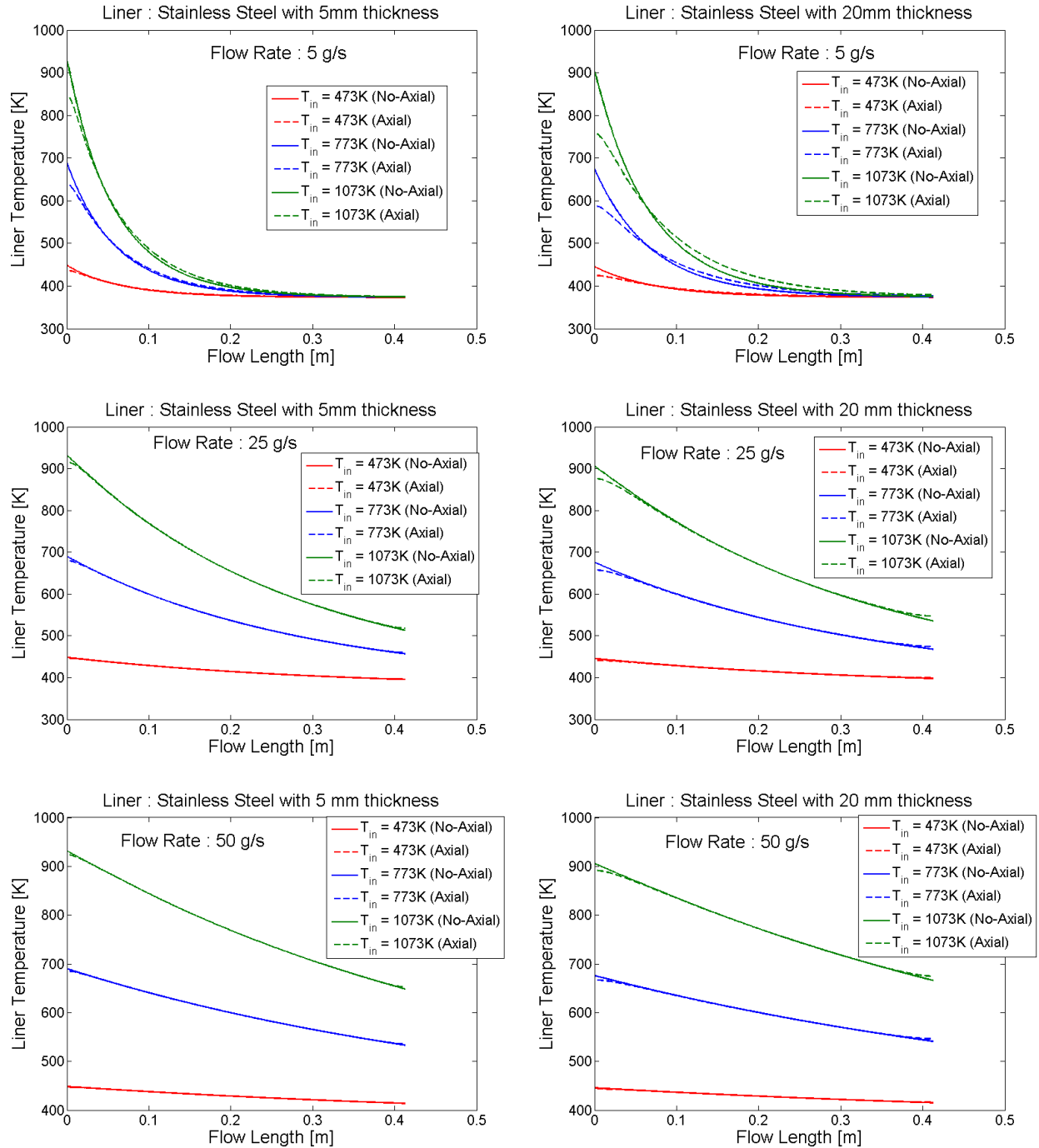


Figure 5.9. Liner temperature variation along the flow direction for 5 mm and 20 mm thick stainless steel liners at inlet temperatures of 473K, 773K and 1073K with flow rates 5g/s, 25g/s and 50g/s.

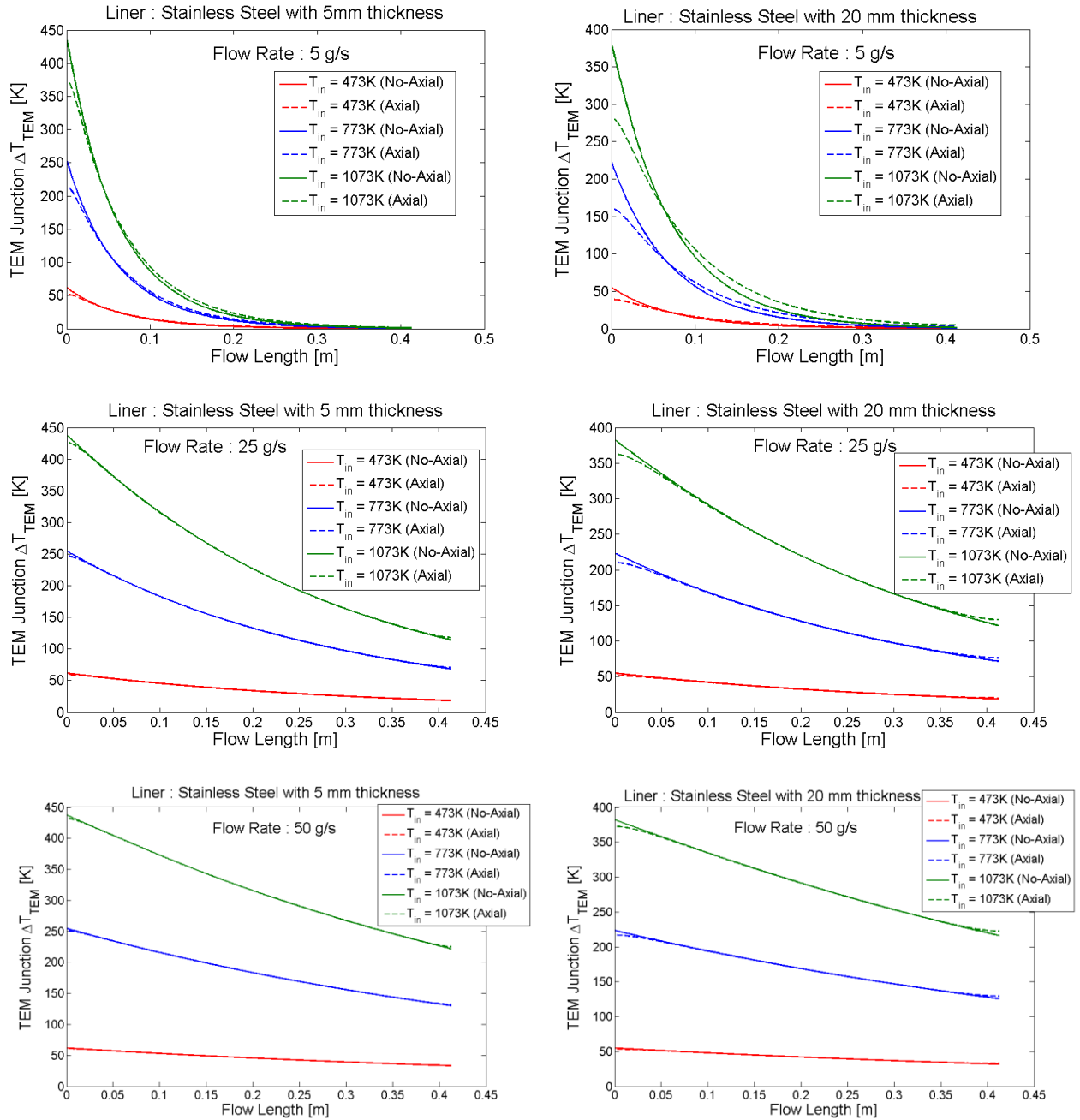


Figure 5.10. TEM junction temperature variation along the flow direction for 5 mm and 20 mm thick stainless steel liners at inlet temperatures of 473K, 773K and 1073K with flow rates 5g/s, 25g/s and 50g/s.

Table 5.2. Parameters representing impact of axial conduction effects on TEG performance at inlet mass flow rate of 5 g/s.

T_{in} [K]	t_w [mm]	Q_{Hex} [W]		$P_{Electric}$ [W]		ΔT_{Gas} [K]	
		With-Axial	Zero-Axial	With-Axial	Zero-Axial	With-Axial	Zero-Axial
473	5	506	507	3.2	3.5	99.6	99.7
	20	503	506	2.5	3.1	98.8	99.5
773	5	2087	2089	56	61	398	399
	20	2072	2084	43.1	54.2	395	398
1073	5	3767	3771	177	191	697	698
	20	3742	3763	137	170	693	697

The inlet sensitivity to TEG performance is presented in Table 5.2. Since, it is observed that the axial conduction is mostly profound for 5g/s flow rate condition, hence, TEG performances based on varying inlet temperatures and liner thicknesses are tabulated. For $T_{in} = 1073K$, electrical power generation lowers to 177 W (differs by 7.9%) and 137 W (differs by 25.4%) for 5 mm and 20 mm thick liner respectively after including axial conduction effects. Even though the change in Q_{Hex} and ΔT_{Gas} is not much appreciable (within 0.2%), the axial conduction shapes the temperature distribution profile at hot side of TE module array; and hence, deters the electric power generation.

5.5 Conclusions

The axial conduction effect was modeled and formulated into the parent TEG numerical model. The new model was run to evaluate TEG performance sensitivity on liner material, liner thickness, and inlet exhaust conditions. The axial conduction affects the temperature distributions in gas stream, hot wall liner and hot side surface of TE modules. Axial conduction homogenizes the temperature in liner leading to decrease in ΔT_{TEMs} near the inlet region (comparatively much hotter than rear end of TEG) and

increase in ΔT_{TEMs} near the exit region. Figure of merit of TEMs (ZT_{TEM}) decreases with decreasing average TE junction temperatures; hence, TEG output performance lowers down. The axial conduction effects are found to have more pronounced impact for a liner made of highly conductive copper than that of stainless steel; and the effects increase with liner thickness. For inlet condition with low flow rate and high temperature condition (5g/s, 1073K), the axial conduction is found to be most detrimental and lowers the electrical power predictions by 25.4% for a 20 mm stainless steel liner when compared to the case with zero axial conduction.

CHAPTER 6. SUMMARY

6.1 Summary and Conclusions

In this work, comprehensive numerical models have been developed to simulate and study the performance of thermoelectric generators (TEGs). The first part of this thesis deals with the formulation of theoretical models to characterize TEGs and is followed by development of numerical framework to perform system level calculations on electrical power generation and pressure drop for a number of critical parameters. The baseline model of General Motors has been studied and critical suggestions for improvement in performance have been presented. Hybrid arrangement of Skutterudite and bismuth telluride with optimized heat exchanger was found to be the most optimal configuration for the baseline TEG in terms for power generation

The second part of this thesis focusses on new TEG topology studies. New design concepts based on longitudinal, transverse, cylindrical and hexagonal circular cross-sections are introduced. These topologies have characteristic shapes with varying degrees of thermoelectric module arrangement with respect to flow, heat exchanger configuration, and bypass system. The variants of developed numerical model are used to study performances statistics for identical inlet conditions and number of thermoelectric modules within allotted pressure budget. The transverse model was found to be the most efficient design for a fixed number of thermoelectric modules at average inlet conditions.

The third part of this thesis has been based on optimization of thermoelectric modules. A numerical approach based on finite difference method is implemented to characterize thermoelectric power conversion efficiencies and their dependence on thermoelectric leg height, cross-sectional areas and TE leg terminal temperatures. The developed model is further employed to optimize thermoelectric modules based on Skutterudites material. Two typical heat exchanger profiles (plate fin heat exchanger and jet impingement) are studied as inputs and optimized geometric configurations for Skutterudite based TEMs are presented. TE modules with leg height of 3.5 mm to 5 mm were found to be most suitable for automotive waste heat recovery systems.

The fourth part of this thesis investigates the axial conduction effects on TEG performance. The numerical model is developed to incorporate axial conduction terms in wall liner and additions are incorporated in parent numerical model. The TEG output sensitivity to liner material, liner thickness, and inlet flow conditions are presented. Axial conduction was found to be more prominent in copper liners as compared to stainless steel ones and increases with liner thickness. Axial conduction in liner was most detrimental to TEG performance for inlet conditions with low flow rates and high temperatures.

6.2 Future Work

6.2.1 Jet Impingement

The analysis of TEG system based on traditional heat exchanger mechanisms approaches has shown that the TEMs should be placed at hottest regions of the TEG system. Also, all the TEMs should be exposed to the same hottest temperatures. TEG design based on jet impingement is one of the probable designs which could harness this

concept. The surface heat transfer surface coefficients for jet impingement range from 200-500 W/m²-K at the expense of desired pressure drop limit of 800 Pa [61].

6.2.2 Modeling Test Bed to Support TEG Development

As a part of thermoelectric design, this project intends to develop a thermoelectric generator's prototype in the facilities of Zucrow Labs, Purdue University. The CFD analysis will be quite helpful in finalization of the final design of prototype. The major findings from the 1D analytical and CFD analysis will be very beneficial in the development of thermoelectric generator.

6.2.3 Transient Analysis

The inlet conditions to the TEG such as the mass flow rate and the exhaust temperature depend on the engine running condition. It has been shown in the present analysis that the variation in the inlet conditions strongly affects the electrical power output, electrical voltage and load current. Hence, a transient analysis of TEG over an engine drive cycle is a critical study. This analysis will help us to assess TEG's performance over a real-time scale. The sensitivity of TEG could be another important study to measure the thermal lag in power generation to inlet variations. However, the transient analysis in 1D may not provide us much understanding about the varying flows and flow reversals inside TEG, 3D analysis could be bit more comprehensive. But 1D transient analysis would be an important first step before initiating a computational study of 3D model as discussed in following section.

6.2.4 Computational Analysis of 3D Model

Since, the current model's analysis was performed in only two dimensions, various physical phenomena associated to this problem like fluid flow reversal, non-uniform

temperature distribution, etc., cannot be analyzed. This is possible if the mass, momentum and energy conservation equations are solved in 3D domain of the thermoelectric generator. Currently available commercial software like ANSYS Fluent has the capability to simulate real life complex physical problems in a 3D computational domain. Comprehensive 3D model simulations will help to understand thermoelectrical and thermodynamical phenomena inside TEGs.

LIST OF REFERENCES

LIST OF REFERENCES

- [1] Yu C., and Chau K. T., 2009, "Thermoelectric automotive waste heat energy recovery using maximum power point tracking," *Energy Convers. Manag.*, **50**(6), pp. 1506–1512.
- [2] Stabler F., 2002, "Automotive applications of high efficiency thermoelectrics," *Proc. DARPA/ONR/DOE High Efficiency Thermoelectric Workshop*, pp. 1–26.
- [3] Rowe D. M., 1995, "CRC handbook of thermoelectrics," *CRC handbook of thermoelectrics*, CRC Press, pp. 441–458.
- [4] Yang J., 2005, "Potential applications of thermoelectric waste heat recovery in the automotive industry," 24th International Conference on Thermoelectrics, 2005. ICT 2005, IEEE, pp. 170–174.
- [5] Rowe D. M., Smith J., Thomas G., and Min G., 2011, "Weight Penalty Incurred in Thermoelectric Recovery of Automobile Exhaust Heat," *J. Electron. Mater.*, **40**(5), pp. 784–788.
- [6] Rowe D. M., 1999, "Thermoelectrics, an environmentally-friendly source of electrical power," *Renew. Energy*, **16**(1-4), pp. 1251–1256.
- [7] Saqr K., and Musa M., 2009, "Critical review of thermoelectrics in modern power generation applications," *Therm. Sci.*, **13**(3), pp. 165–174.
- [8] Tang X., Zhang ., Chen L., Goto T., and Hirai T., 2005, "Synthesis and thermoelectric properties of p-type- and n-type-filled skutterudite $RyMxCo_{4-x}Sb_{12}(R:Ce,Ba,Y;M:Fe,Ni)$," *J. Appl. Phys.*, **97**(9), pp. 093712–093712–10.
- [9] Rogl G., Grytsiv A., Bauer E., Rogl P., and Zehetbauer M., 2010, "Thermoelectric properties of novel skutterudites with didymium: $DDy(Fe_{1-x}Co_x)_4Sb_{12}$ and $DDy(Fe_{1-x}Ni_x)_4Sb_{12}$," *Intermetallics*, **18**(1), pp. 57–64.
- [10] Zhao X. B., Ji X. H., Zhang Y. H., Zhu T. J., Tu J. P., and Zhang X. B., 2005, "Bismuth telluride nanotubes and the effects on the thermoelectric properties of nanotube-containing nanocomposites," *Appl. Phys. Lett.*, **86**(6), pp. 062111–062111–3.
- [11] Suter C., Tomeš P., Weidenkaff A., and Steinfeld A., 2010, "Heat Transfer and Geometrical Analysis of Thermoelectric Converters Driven by Concentrated Solar Radiation," *Materials*, **3**(4), pp. 2735–2752.
- [12] Tomeš P., Trottmann M., Suter C., Aguirre M. H., Steinfeld A., Haueter P., and Weidenkaff A., 2010, "Thermoelectric Oxide Modules (TOMs) for the Direct Conversion of Simulated Solar Radiation into Electrical Energy," *Materials*, **3**(4), pp. 2801–2814.

- [13] Riffat S. B., and Ma X., 2003, "Thermoelectrics: a review of present and potential applications," *Appl. Therm. Eng.*, **23**(8), pp. 913–935.
- [14] Espinosa N., Lazard M., Aixala L., and Scherrer H., 2010, "Modeling a Thermoelectric Generator Applied to Diesel Automotive Heat Recovery," *J. Electron. Mater.*, **39**(9), pp. 1446–1455.
- [15] Chau K. T., Wong Y. S., and Chan C. C., 1999, "An overview of energy sources for electric vehicles," *Energy Convers. Manag.*, **40**(10), pp. 1021–1039.
- [16] Yodovard P., Khedari J., and Hirunlabh J., 2001, "The Potential of Waste Heat Thermoelectric Power Generation From Diesel Cycle and Gas Turbine Cogeneration Plants," *Energy Sources*, **23**(3), pp. 213–224.
- [17] Morelli D. T., 1996, "Potential applications of advanced thermoelectrics in the automobile industry," , Fifteenth International Conference on Thermoelectrics, 1996, IEEE, pp. 383–386.
- [18] Neild A. B., 1963, "Portable Thermoelectric Generators," Society of Automotive Engineers, SAE-645A, New York, USA.
- [19] Birkholz U., Grob E., Stohrer U., Voss K., Gruden D. O., and Wurster W., 1988, "Conversion of Waste Exhaust Heat in Automobile using FeSi₂ Thermoelements," *Proc. 7th International Conference on Thermoelectric Energy Conversion*, Arlington, USA, pp. 124–128.
- [20] Bass J., Campana R. J., and Elsner N. B., 1992, "Thermoelectric Generator Development for Heavy-Duty Truck Applications," *Proc. Annual Automotive Technology Development Contractors Coordination Meeting*, Dearborn, Michigan, USA, pp. 743–748.
- [21] Bass J. C., Elsner N. B., and Leavitt F. A., 1994, "Performance of the 1 kW thermoelectric generator for diesel engines," *AIP Conf. Proc.*, **316**(1), pp. 295–298.
- [22] Ikoma K., Munekiyo M., Furuya K., Kobayashi M., Izumi T., and Shinohara K., 1998, "Thermoelectric module and generator for gasoline engine vehicles," XVII International Conference on Thermoelectrics, 1998. *Proceedings ICT 98*, IEEE, pp. 464–467.
- [23] Thacher E. F., Helenbrook B., and Karri M. A., 2006, "Progress in Thermoelectrical Energy Recovery from a Light Truck Exhaust," *Proc. DEER Conference*, Detroit, Michigan.
- [24] Thacher E. F., Helenbrook B. T., Karri M. A., and Richter C. J., 2007, "Testing of an automobile exhaust thermoelectric generator in a light truck," *Proc. Inst. Mech. Eng. Part J. Automob. Eng.*, **221**(1), pp. 95–107.
- [25] Hsiao Y. Y., 2010, "A mathematic model of thermoelectric module with applications on waste heat recovery from automobile engine," *Energy*, **35**(3), pp. 1447–1454.
- [26] Karri M. A., Thacher E. F., and Helenbrook B. T., 2011, "Exhaust energy conversion by thermoelectric generator: Two case studies," *Energy Convers. Manag.*, **52**(3), pp. 1596–1611.
- [27] Kim S., Park S., Kim S., and Rhi S.-H., 2011, "A Thermoelectric Generator Using Engine Coolant for Light-Duty Internal Combustion Engine-Powered Vehicles," *J. Electron. Mater.*, **40**(5), pp. 812–816.

- [28] Xiao H., Gou X., and Yang C., 2008, "Simulation analysis on thermoelectric generator system performance," Asia Simulation Conference - 7th International Conference on System Simulation and Scientific Computing, 2008. ICSC 2008, IEEE, pp. 1183–1187.
- [29] Yu J., and Zhao H., 2007, "A numerical model for thermoelectric generator with the parallel-plate heat exchanger," J. Power Sources, **172**(1), pp. 428–434.
- [30] Meng F., Chen L., and Sun F., "A numerical model and comparative investigation of a thermoelectric generator with multi-irreversibilities," Energy, **36**(5), pp. 3513–3522.
- [31] Eder A., Liebi J., and J nsch D., 2009, "Thermoelektrik Eine Chance fr die Automobilindustrie," Thermoelektrik Eine Chance fr die Automobilindustrie, expert verlag, Renningen, Germany, pp. 45–56.
- [32] Crane D. T., and LaGrandeur J. W., 2009, "Progress Report on BSST-Led US Department of Energy Automotive Waste Heat Recovery Program," J. Electron. Mater., **39**(9), pp. 2142–2148.
- [33] Fairbanks J. W., 2011, "Vehicular Thermoelectrics: A New Green Technology," Proc. 2011 Directions in Engine-Efficiency and Emissions Research (DEER) Conference, Detroit, Michigan.
- [34] Yang J., 2009, "Engineering and Materials for Automotive Thermoelectric Applications," Proc. 2009 Thermoelectrics Applications Workshop, San Diego, CA.
- [35] Meisner G. P., 2011, "Advanced Thermoelectric Materials and Generator Technology for AutomotiveWaste Heat at GM," Proc. 2011 Thermoelectrics Applications Workshop, San Diego, CA.
- [36] Meisner G. P., 2011, "Thermoelectric Conversion of Exhaust Gas Waste Heat into Usable Electricity," Proc. 2011 Directions in Engine-Efficiency and Emissions Research (DEER) Conference, Detroit, Michigan.
- [37] Xuan X.C., Ng K.C., Yap C., and Chua H.T., 2002, "A general model for studying effects of interface layers on thermoelectric devices performance," Int. J. Heat Mass Transf., **45**(26), pp. 5159–5170.
- [38] Liang G., Zhou J., and Huang X., 2011, "Analytical model of parallel thermoelectric generator," Appl. Energy, **88**(12), pp. 5193–5199.
- [39] Cola B. A., Xu J., and Fisher T. S., 2009, "Contact mechanics and thermal conductance of carbon nanotube array interfaces," Int. J. Heat Mass Transf., **52**(15-16), pp. 3490–3503.
- [40] Cola B. A., Xu J., Cheng C., Xu X., Fisher T. S., and Hu H., 2007, "Photoacoustic characterization of carbon nanotube array thermal interfaces," J. Appl. Phys., **101**(5), pp. 054313–054313–9.
- [41] Cola B. A., Xu X., Fisher T. S., Capano M. A., and Amama P. B., 2008, "Carbon Nanotube Array Thermal Interfaces for High-Temperature Silicon Carbide Devices," Nanoscale Microscale Thermophys. Eng., **12**(3), pp. 228–237.
- [42] Matsubara K., 2001, "The Performance of a Segmented Thermoelectric Convertor Using Yb-Based Filled Skutterudites and Bi₂Te₃-Based Materials," MRS Online Proc. Libr., **691**, p. null.

- [43] Matsubara K., 2002, "Development of a high efficient thermoelectric stack for a waste exhaust heat recovery of vehicles," Twenty-First International Conference on Thermoelectrics, 2002. Proceedings ICT '02, IEEE, pp. 418–423.
- [44] Graff J., Zhu S., Holgate T., Peng J., He J., and Tritt T. M., 2011, "High-Temperature Thermoelectric Properties of Co₄Sb₁₂-Based Skutterudites with Multiple Filler Atoms: Ce_{0.1}In_xYb_yCo₄Sb₁₂," *J. Electron. Mater.*, **40**(5), pp. 696–701.
- [45] Shi X., Yang J., Salvador J. R., Chi M., Cho J. Y., Wang H., Bai S., Yang J., Zhang W., and Chen L., 2011, "Multiple-Filled Skutterudites: High Thermoelectric Figure of Merit through Separately Optimizing Electrical and Thermal Transports," *J Am Chem Soc*, **133**(20), pp. 7837–7846.
- [46] Rowe D. M., 2006, "Review: Thermoelectric Waste Heat Recovery as a Renewable Energy Source," *IJESP*, **1**(1), pp. 13–23.
- [47] Takanose E., and Tamakoshi H., 1994, "The development of Thermoelectric Generator for Passenger Car," *Proc. 12th International Conference on Thermoelectrics*, Tokyo, Japan, pp. 467–470.
- [48] Buist R. J., 1995, "Calculation of Peltier Device Performance," *CRC Handbook of Thermoelectrics*, CRC Press, Boca Raton, FL, pp. 143–156.
- [49] Dresselhaus M. S., Lin Y. M., Koga T., Cronin S. B., Rabin O., Blackand M. R., and Dresselhaus G., 2001, *Semiconductors and Semimetals, recent Trends in Thermoelectric materials Research III*, Academic, San Diego, CA.
- [50] Hendricks T. J., and Lustbader J. A., 2002, "Advanced thermoelectric power system investigations for light-duty and heavy duty applications. I," Twenty-First International Conference on Thermoelectrics, 2002. Proceedings ICT '02, IEEE, pp. 381–386.
- [51] Incropera F. P., and DeWitt D. P., 2007, *Fundamentals of heat and mass transfer*, John Wiley.
- [52] Salvador J. R., 2014, "Email conversation with the author."
- [53] Chanson H., 2004, *Hydraulics of Open Channel Flow: An Introduction*, Butterworth–Heinemann, p. 231.
- [54] Baker C., Vuppuluri P., Shi L., and Hall M., 2012, "Model of Heat Exchangers for Waste Heat Recovery from Diesel Engine Exhaust for Thermoelectric Power Generation," *J. Electron. Mater.*, **41**(6), pp. 1290–1297.
- [55] Kumar S., Heister S. D., Xu X., Salvador J. R., and Meisner G. P., 2013, "Thermoelectric Generators for Automotive Waste Heat Recovery Systems Part I: Numerical Modeling and Baseline Model Analysis," *J. Electron. Mater.*, **42**(4), pp. 665–674.
- [56] Kumar S., Heister S. D., Xu X., Salvador J. R., and Meisner G. P., 2013, "Thermoelectric Generators for Automotive Waste Heat Recovery Systems Part II: Parametric Evaluation and Topological Studies," *J. Electron. Mater.*, **42**(6), pp. 944–955.
- [57] Kumar S., Heister S. D., Xu X., Salvador J. R., and Meisner G. P., 2012, "Thermal Design of Thermoelectric Generators for Automotive Waste Heat Recovery," *ASME 2012 Summer Heat Transfer*, Rio Grande, Puerto Rico.

- [58] Shih T., and Hogan T., 2005, "Modeling and Characterization of Power Generation Modules Based on Bulk Materials," *Thermoelectrics Handbook*, D. Rowe, ed., CRC Press, pp. 12-1-12-23.
- [59] Domenicali C. A., 1953, "Irreversible Thermodynamics of Thermoelectric Effects in Inhomogeneous, Anisotropic Media," *Phys. Rev.*, **92**(4), pp. 877-881.
- [60] Bradie B., 2005, *A Friendly Introduction to Numerical Analysis*, Pearson.
- [61] Martin H., 1977, "Heat and Mass Transfer between Impinging Gas Jets and Solid Surfaces," *Advances in Heat Transfer*, James P. Hartnett and Thomas F. Irvine, ed., Elsevier, pp. 1-60.

APPENDIX

APPENDIX

Comparison of Methods for Electric Power Calculations

The material properties of thermoelectric legs are dependent on the temperatures. The spatial variation in temperature would lead to large differences in calculated parameters if averaging principles were used. The average based calculations are performed by Eq. (A.1) [58].

$$\eta_T = \frac{I(\alpha(T_H - T_C) - IR)}{\alpha T_H I + K(T_H - T_C) - 0.5I^2 R} \quad (\text{A.1})$$

In this section, a list of such methods are represented and compared with the discussed iterative methods. Iterative method has been discussed in detail in previous sections of this paper. The methods of interest are with brief description:

- 1) Simple Average Method: The leg properties are calculated at average junction temperature. i.e. $T_M = (T_H + T_C)/2$. For example: $\alpha_{n,p} = \alpha_{n,p}(T_M)$
- 2) Integral Average Method:
 - a. Integral Average (α): Only Seebeck coefficients are integral averaged over T_H and T_C . Other properties are calculated at average junction temperature.

$$\alpha_{n,p} = \frac{\int_{T_C}^{T_H} \alpha_{n,p} dT}{T_H - T_C} \quad (\text{A.2})$$

- b. Integral Average (all): All the properties are integral averaged over junction temperatures.

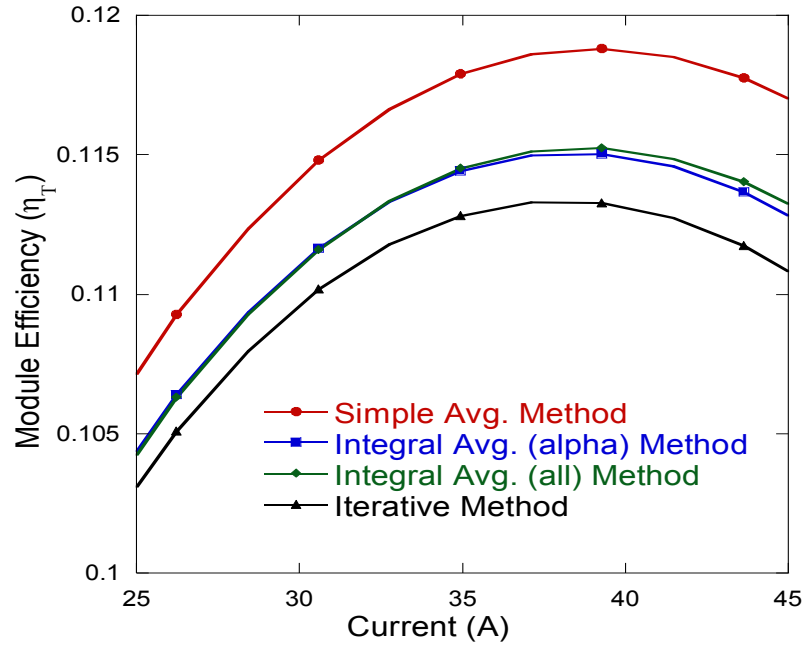


Figure A 1. Method comparison at different current inputs for skutterudites at $Lx = 10$ mm, $A_N/A_P = 0.8$; $\Delta T = 450^\circ\text{C}$, and $A_P = 1\text{cm}^2$.

The simple average method over predict efficiency values and do not match the iterative method. However, integral average methods perform better than simple averaging method; it may not be suitable for near optimal point analysis or for high current values input. The simple averaging methods do not take into account the Thomson effect at higher current values. Iterative method accounts for the material property variations and hence Thomson effect is accounted for various ranges of input current.

VITA

VITA

Sumeet graduated from Indian Institute of Technology Kharagpur (IITKGP) in 2008 with B. Tech. and M. Tech. degrees in Mechanical Engineering. During his undergraduate research, he developed numerical models for melting and solidification processes for multi-component systems under the presence of external electromagnetic fields. He interned in ANSYS Fluent Ltd, Pune, India (2006), and European Organization for Nuclear Research (CERN), Geneva, Switzerland (2007). After graduation, he worked with Schlumberger Oilfields Ltd. (2008-2009), and Tridiagonal Solutions Pvt. Ltd., Pune, India (2009-2010). He started working with Prof. Stephen Heister and Prof. Xianfan Xu at Purdue University towards his Ph.D. since 2010. His research involves theoretical and numerical modeling of thermoelectric generators; and proposing performance improvements and innovative design concepts. Upon completing his Ph.D., Sumeet will be joining the Wafer Inspection Group at KLA-Tencor, Milpitas, CA in September, 2014.

PUBLICATIONS

PUBLICATIONS

Journals

- Kumar S., Heister S. D., Xu X., Salvador J. R., and Meisner G. P., 2013, “Thermoelectric Generators for Automotive Waste Heat Recovery Systems Part I: Numerical Modeling and Baseline Model Analysis,” *Journal of Electronic Materials*, **42**(4), pp. 665–674.
- Kumar S., Heister S. D., Xu X., Salvador J. R., and Meisner G. P., 2013, “Thermoelectric Generators for Automotive Waste Heat Recovery Systems Part II: Parametric Evaluation and Topological Studies,” *Journal of Electronic Materials*, **42**(6), pp. 944–955.
- Kumar S., Heister S. D., Xu X., and Salvador J. R., “Optimization of Skutterudite based Thermoelectric Modules for Automotive Thermoelectric Generators,” *Submitted to Journal of Electronic Materials* (October, 2014).

Conferences

- Kumar S., Heister S. D., Xu X., Salvador J. R., and Meisner G. P., “Thermal Design of Thermoelectric Generators for Automotive Waste Heat Recovery,” *Proc. ASME 2012 Summer Heat Transfer Conference*, Rio Grande, Puerto Rico (July, 2012).
- Kumar S., Heister S. D., Xu X., and Salvador J. R., “Numerical Analysis of Thermoelectric Modules for Automobile Waste Heat Recovery Systems,” *ASME IMECE 2013*, San Diego, California (November, 2013)
- Kumar S., Dubitsky A., Heister S. D., Xu X., “Jet Impingement concept for Thermoelectric Generators,” *International Conference on Thermoelectrics – ICT 2014*, Nashville, Tennessee (July, 2014)